A METHOD OF STRENGTHENING MONITORED DEFICIENT BRIDGES

by

BRANDON RICHARD DECKER

B.S., Kansas State University, 2005

A THESIS

submitted in partial fulfillment of the requirements for the degree

MASTER OF SCIENCE

Department of Civil Engineering
College of Engineering

KANSAS STATE UNIVERSITY
Manhattan, Kansas

2007

Approved by:

Major Professor
Hayder A. Rasheed

Abstract

There is a high need to repair or replace many bridges in the state of Kansas. 23% of the bridges in Kansas are labeled structurally deficient or functionally obsolete. A majority of these bridges serve rural areas and are damaged due to overloading during harvest season. A state-of-the-art method of performing structural health monitoring on these bridges followed by an effective method of strengthening and repair was researched and presented in this thesis.

The first phase of this research involved researching multiple devices to be used for state-of-the-art health monitoring. After deciding on an appropriate system, multiple tests were performed to determine the systems performance compared against conventional systems. The system was tested on a laboratory scale pre-stressed concrete T-beam. The system was tested on its ability to effectively record and transmit acceleration data. If this system were to be implemented on an actual bridge, KDOT could make a decision to repair or strengthen the bridge based on the results. The next phase of the research was to determine an effective strengthening procedure using carbon fiber reinforced polymer (CFRP).

Reinforced concrete beam specimens were cast and tested in the lab. The specimens consisted of rectangular and T-shaped cross-sections to create different failure modes when tested in bending. The primary issue when strengthening with CFRP is the issue of early separation failure when using CFRP in the longitudinal direction only. In an effort to prove this, the specimens were strengthened with five layers of CFRP and tested in four-point bending until failure. In an effort to prevent early separation failure, CFRP "U-wraps" were applied to provide shear resistance and additional anchorage for the flexural CFRP. The beams were then tested in flexure until failure by FRP rupture or concrete crushing followed by FRP rupture. The test results indicate that the U-wraps allowed the FRP to reach full capacity and fail in FRP rupture. The use of CFRP provided a strength increase of about 220% over the control beam specimens while significantly reducing the ultimate deflection.

Table of Contents

List of Figures

List of Tables

Acknowledgements

This project was made possible by funding through the University Transportation Center. CFRP strengthening materials were kindly donated by VSL Strengthening Products, a division of Structural Group. Materials for construction of the reinforced concrete lab specimens were donated by Ambassador Steel and Gateway Building Materials.

I would especially like to than Dr. Hayder Rasheed for the opportunity to participate in this project, and also his guidance and support throughout the research. I would also like to thank Dr. Asad Esmaeily, Dr. Robert Peterman, and Dr. Hani Melhem for acting as committee members and providing their support and knowledge in the research. I would also like to give a special thanks to our Civil Engineering Lab Technician, Dave Suhling, for providing assistance in the lab during construction and testing of the experimental specimens. I would also like to give thanks to Jeff Peterson from Caterpillar for introducing us to and explaining the MicroStrain wireless instrumentation system. I would also like to thank some of my fellow and former students for taking time out of their busy schedules to provide assistance in the experimental portion of the research, especially LJ Dickens, Kyle Larson, Steve Hart, Sarah Grotheer and Long Qiao.

CHAPTER 1 - Introduction

Background

The need to repair, upgrade or replace infrastructure elements on the Kansas and National bridge inventory is increasing due to the aging of structural components and materials as well as the expanding volume and weight of traffic. In the year 2004, almost 23% of the 25,525 bridges in Kansas were labeled either structurally deficient or functionally obsolete. Of the total Kansas bridges, 23,093 were not on the national highway system (NHS) with 5,456 deficient and obsolete bridges. A significant number of these bridges serve rural Kansas, which has very limited funding and low priority for rehabilitation or upgrade. There has been evidence of severe cracking of prestressed concrete girders on Kansas rural bridge inventory due to frequent overloads during harvest season. The Federal Highway Administration estimated that funding of $215 billion is necessary to repair all the bridges and roads in their current conditions. Replacement costs are expected to be larger by many folds. Accordingly, there is a clear need for objective methods to assess and evaluate the condition of the structurally deficient and functionally obsolete bridges to prioritize the need for repair, strengthening, replacement or closing and detouring.

Presently, visual inspection is being routinely conducted according to the National Bridge Inspection Program to estimate the functional state of bridges and establish a continuous condition record that can be used to determine priorities for repair or upgrade actions. In addition, the Federal Highway Administration is developing software (Virtis) that facilitates the visual inspection and rating of bridges by adding multimedia features that allow inspectors to perform condition assessment and comparisons from their offices. However, visual inspection is time consuming and depends on the experience and judgment of the inspector since it lacks sufficient testing tools.

Therefore, the University Transportation Center provided funding to develop a health monitoring system for remote sensing, evaluation and feedback in a model rural highway bridge with existing damage. There is a clear need for such a rational basis to prioritize decisions on repairing or replacing deficient bridges. The health monitoring system will be installed and tested on laboratory-scale beams to verify its proper functionality prior to implementing it in the actual bridge, which will be performed in future projects. Based on the health monitoring system installed, Kansas Department of Transportation (KDOT) may decide to repair and strengthen some of the deteriorated bridge elements to extend the deficient bridge life for another 20 years. Consequently, the health monitoring system will serve as an essential tool to monitor the effectiveness of the new repair and strengthening techniques and to detect any new deterioration that can possibly occur in these upgrades.

Objectives

The primary objective of this study is to develop a state-of-the-art health monitoring system to allow for remote sensing, evaluation and feedback of a model rural bridge with existing damage. Visual inspection is obviously not a very reliable way to assess the internal condition of bridge elements. Accordingly, a bridge member will be used to examine the functionality of a wireless health monitoring system. The health monitoring system will be designed to provide a continuous record of the strain and stiffness conditions of the bridge girders under the action of a moving load. The main sensors that will be used in the process are: (a) wireless transceiver to connect to strain gages to measure the state of strain and stress in the girders, (b) accelerometer to measure the vibration of the girder element and provide an accurate account of the stiffness distribution, (c) Linear Variable Displacement Transducers (LVDT) to measure deflection in girders.

Another main objective is to determine an effective bridge strengthening procedure should KDOT decide to repair and strengthen the deteriorated bridge elements as opposed to total bridge replacement. Effective strengthening method will be investigated to qualify the efficient use of externally bonded carbon fiber reinforced polymer (CFRP) sheets on concrete bridge girders. To achieve this objective, six, 16-ft long reinforced concrete beams are built. Three of them with rectangular cross-sections, and three with T-shaped cross sections to create different failure modes.

Complete design and construction details of the beam specimens will be discussed along with test methods and experimental procedures. Finally, conclusions and recommendations for future research will be discussed.

Scope

This thesis is composed of two separate parts. Part I will discuss in detail the research involving bridge strengthening using CFRP reinforcement. For this area of research, a literature review was first performed to investigate a range of previous studies on the control of CFRP separation failure in concrete bridge element strengthening. Following the literature review is an explanation of the design of the laboratory specimens and the properties of the materials that were used in the construction of the specimens. The step-by-step construction of the specimens is then described including the casting of the concrete beams and the procedure for applying the CFRP reinforcement. Following this is the section describing the experimental testing procedures of the specimens as well as the experimental results. The results from the experimental tests are then analyzed to determine and explain the effectiveness of using CFRP as an efficient method for reinforcing concrete bridge elements by eliminating premature separation failure.

Part II of the thesis is the topic of state-of-the-art health monitoring system. A literature review is also included for this research topic to determine if there is any new development in state-of-the-art monitoring equipment specifically wireless health monitoring systems. The findings of an experimental program will be described on laboratory scale bridge member to assess and monitor its health state in terms stiffness and strain.

PART I: Strengthening Reinforced Concrete Girders with CFRP

CHAPTER 2 - Literature Review

Structural strengthening and repair have become a major issue over the past two decades due to infrastructure in need of upgrades or repair. Externally bonded Fiber Reinforced Polymer (FRP) provides a state-of-the-art technique for strengthening and rehabilitation. Traditional methods of strengthening involve the application of externally bonded steel sheets. But some problems with this include deterioration of the bond between the steel and concrete due to steel corrosion, the difficulty to handle large steel plates and limited delivery lengths. Composites can provide a strengthening technique where conventional systems do not work. Specifically, FRP sheets can be used in place of steel sheets. FRP sheets can be wrapped around a structural element to provide an increase in strength and ductility.

Bakis et al. (2002) investigate the current practice of using externally bonded FRP in Civil Infrastructure. External FRP can be effective in flexural reinforcement when the FRP material is epoxy bonded to the tension surface of the structural element with the fibers oriented in the longitudinal direction. A well established strengthening procedure can be followed as long as attention is given to the linear-elastic response of the FRP material and the bond quality. Multiple modes of failure can be expected with the use of FRP strengthening, these include: (1) yielding of steel followed by FRP rupture; (2) yielding of steel followed by crushing of concrete; (3) crushing of concrete; (4) FRP debonding at the end of the plate due to concrete shear failure; (5) FRP debonding far away from the plate ends due to shear cracks; (6) FRP debonding at plate end due to flexural cracking; and (7) FRP debonding at FRP-concrete interface due to poor bond or imperfections on the concrete surface. Externally bonded FRP material can also provide shear strength of RC beams. The can be accomplished by either partial or full wrapping of FRP around the element with fibers oriented parallel to the principal tensile stresses.

The failure mode is the main factor in the effectiveness of FRP for shear strengthening. The primary failure modes are debonding of the FRP through the concrete or rupture of FRP. The failure mode that is to occur first depends on the quality of the bond, the anchorage length, the type of FRP attachment, the rigidity of the FRP and the concrete strength. Most often, the failure mode is a combination of both cases. The most significant use of externally bonded FRP has been the increase of confinement in structurally deficient RC structures in seismic zones. Increased confinement can increase the ductility and prevent debonding of internal reinforcement. Proper confinement can increase capacity of a bridge due to increased loads. When designing externally bonded FRP reinforcement it is important to consider the fact that strengthening should be minimal in case an unexpected event such as a fire were to occur, unless a proper method of protecting the reinforcement is implemented.

Arduini and Nanni, (1997) investigated the use CFRP sheets to strengthen pre-cracked reinforced concrete beams. Four-point bending tests were conducted on the FRP strengthened beams and compared to control beams and beams that are not pre-cracked. For their experimental program, beams with shallow section geometry and beams with deep section geometry were constructed. Two different surface preparation techniques were also tested on the beam. One technique was surface cleaning with a power sander. The other technique involved sandblasting the concrete surface. To simulate the case of FRP strengthening to a structure without removing the service load, the experimental specimens were loaded to 30% of their ultimate moment capacity and then strengthened while the load was maintained. The CFRP strengthening was applied to the specimens in the longitudinal direction using the manual layup procedure, where a primer or resin is first applied, followed by the fabric, then followed by another layer of resin, which is repeated for multiple plies. For one of the groups of specimens, CFRP was also applied in the transverse direction to try and prevent the longitudinal sheet from debonding. Based on their results, Arduini and Nanni concluded that a pre-cracked specimen is not significantly different from a non-cracked specimen. The pre-cracked specimen did show a slightly lower initial stiffness and ultimate capacity. Surface preparation by sandblasting showed to be more effective than sanding. It was also concluded that application of CFRP in the transverse direction is effective in preventing debonding. The strengthened specimens showed an increase in strength of 38%.

Rahimi and Hutchinson (2001) also looked into the suitability of using externally bonded FRP for reinforcing concrete structures. Primarily they investigated the aspect of adhesive bonding. They also compared pre-cracked to un-cracked specimens, as well as type and thickness of external reinforcement, and plate-end geometry. Three different types of external reinforcement were tested, glass FRP (GFRP), carbon FRP (CFRP), and external mild steel. The CFRP varied in thickness from 0.4 mm to 1.2 mm, while the GFRP was chosen to be 1.8 mm due to its low modulus. The external steel reinforcement consisted of 3 mm thick mild steel plates. All types of reinforcement were bonded to the concrete using a two-part epoxy adhesive. The specimens were tested in four-point bending using a hydraulic jack with load increments of 5 kN. The results showed that none of the specimens failed as a result of adhesion failure. The beams that failed due to FRP debonding failed with the epoxy and concrete still attached to the plate. There were two primary failure modes, failure in the constant moment region and failure in the shear span. The mode of failure was dependant on the type and thickness of the reinforcement. The specimens strengthened with thin laminates failed in a mode of concrete crushing. As the plate thickness was increased, the specimens started to fail toward the end plates. The specimens reinforced with external mild steel failed by steel yielding ultimately followed by plate debonding originating at the plate ends. The specimens strengthened with the composite plates showed much more significant increase in stiffness and strength over those strengthened with mild steel. The specimens strengthened with composite material showed an increase in ultimate load-carrying capacity of 230% over the control specimens.

Larson et al. (2005) researched strengthening of pre-stressed concrete bridge girders with CFRP sheets. Previous research on 30-year-old pre-stressed concrete T girders was conducted by Reed and Peterman (2004). However, these girders failed prematurely to do strand fatigue. In their research, Larson et al. (2005) strengthened 16.5 ft. long pre-stressed T-beams. Prior to strengthening and testing, all beam specimens were pre-cracked by loaded them past their cracking moment to simulate a bridge girder in service. In their experimental procedure, six beams were tested in four-point bending.

Beam 1 was tested with no CFRP strengthening as a control beam. Beams 2-5 were strengthened with CFRP reinforcement. Beams 2 and 3 were designed for the CFRP reinforcement to control the stress in the pre-stressing strand to 18 ksi, while beams 4 and 5 were designed for 36 ksi. Beams 2 and 4 were loaded statically, while beams 3 and 5 were tested cyclically to demonstrate long-term serviceability. For the strengthening procedure the beams were flipped up-side-down for ease of strengthening and safety concerns. The beams were then sandblasted to remove and imperfections and foreign substances. The CFRP was applied using a wet lay-up process with a two-part epoxy system. The beams were also strengthened with external CFRP wraps to try and prevent debonding of CFRP. The test of the control beam showed that failure occurred at a load of 15.1 kips due to rupture of the pre-stressing strand. Beam 2 showed an increase in strength to 25.7 kips with a failure mode of CFRP rupture. The cyclic loading of beam 3 showed some loss in stiffness due to possible opening of flexural cracks during loading. However, strength and ductility were not affected by the cyclic loading. The beam failed at a load of 25.3 kips in a mode of CFRP rupture. Beam 4 showed a larger increase in strength over the control beam as expected. The beam failed in rupture of CFRP at a load of 32.2 kips. The stress in the CFRP at failure was 73 ksi, which is significantly higher than the design stress of 36 ksi. The cyclic loading of beam 5 once again showed some decrease in stiffness. The beam failed prematurely in rupture of CFRP at a load of 26.2 kips. However, this failure is in agreement with ACI 440.2R-02 which states that fatigue strength of CFRP is 60-70% of its initial static strength after one million cycles.

Teng et al. (2003) investigated the issue of intermediate crack (IC) debonding due to flexural cracks or flexural-shear cracks located away from plate ends. A model is developed for IC debonding failure based on a model for bond strength between FRP and concrete. Teng et al. then develop a procedure for strengthening of beams based on the IC debonding model. IC debonding is caused by a large flexural crack developing in the concrete. As this crack grows, tension is relieved in the concrete and transferred to the FRP plate. This causes high stresses in the area between the FRP plate and the concrete. As the load increases, theses stresses become larger until debonding initiates and spreads towards the plate end. The bond strength model determines the stress in the FRP plate that causes debonding. This stress is related to the elastic modulus, thickness and width of the plate, as well as concrete test cylinder compressive strength. To apply this model to IC debonding, the critical location of crack development needs to be determined. Once this location is determined, the bond length is determined to be the distance from this critical section to the nearest plate end. After determining the bond length, the critical stress at which debonding occurs can be found. This model is calibrated based on experimental data collected through an extensive literature survey. The calibration is performed by determining a value of the coefficient α from the experimental data. It is determined that a value of 0.48 be proposed for α. This value is considered to be conservative but satisfactory for design use. Teng et al. believe that the failure mode of shear failure as well as failure modes due to plate end debonding can be prevented. It is recommended that plate ends be located where the moment is as close to zero as possible. Also end anchorage should be provided in order to prevent debonding. End anchorage can be provided by use of U jacketing or U wrapping. By using several U jackets near the plate end, the debonding load can be greatly increased. U jacketing also provides additional shear resistance. If debonding does not occur then the ultimate moment of the section will be reached when failure occurs due to rupture of FRP or crushing of concrete. When designing based on debonding not considered, a three step procedure is developed. The first step is to determine the ultimate plate stress for IC debonding. The next step is to determine the reduced tensile stress of the FRP plate. The final step is to determine the ultimate moment of the critical section.

Spadea et al. (1998) decided that there are still many unknown issues when RC beams are strengthened with CFRP. They suggested the use of external steel plate stirrups to improve the composite action, and perform experiments to develop a better understanding of CFRP strengthening. The specimens used in their experiments consisted of four 5,000mm long beams with rectangular cross section of 140 x 300 mm. Beam 1 was tested with no external reinforcement as a control beam. Beam 2 was strengthened with a single CFRP sheet on the tension face. Beam 3 was strengthened with the same single CFRP sheet on the tension face but with external end anchorage and anchorage along the support. Beam 4 was similar to beam 3 but with different anchorage locations. The external anchorages consisted of steel plates. The beams were loaded in four-point bending while load-deflection and strain results were recorded during the test.

The results indicate that the use of a CFRP plate on the tension surface without considering additional anchorage significantly reduces deflection at the ultimate load. However, the use of a CFRP plate without additional anchorage can significantly degrade the structural behavior resulting in brittle failure. The structural behavior can be restored by the use of external anchorages at the ends and at critical locations along the beam. The beam with sufficient anchorage provided sufficient CFRP bond and maintained composite action up to 98.6% of its ultimate capacity and provided a 70% increase in load over the control beam. The external anchorage also provided a more ductile failure. Teng et al. conclude that the use of external anchorage has a significant influence on the structural ductility of a RC beam but provide no methodology to compute the required anchorage.

Once the transverse FRP U-wraps are successful in suppressing the separation failure mode, RC beams strengthened with composites are anticipated to develop their full flexural capacity. This leaves FRP rupture and concrete crushing as the two predominant flexural failure modes. This would also increase the strength and ductility of the strengthened flexural members.

CHAPTER 3 - Design of Specimens

The experimental program consists of designing and testing six concrete beams. Three beams have a rectangular shaped cross section and three specimens have T-shaped cross section. One of each of the beam types was used as a control specimen with no application of CFRP to serve as a base line to compare to the beams strengthened with CFRP. The second beam, in each of the two series, was strengthened with flexural CFRP on the bottom of the beam only. Then, it was tested to demonstrate the issue of CFRP premature debonding. The third beam, in each of the two series, has the same flexural CFRP reinforcement on the bottom along with U-shaped CFRP wraps to anchor the flexural sheets and prevent debonding.

Beam Geometry

The lab testing equipment that is used has an actuator capacity of 50 kips. So it was important that the beams be designed so that the ultimate capacities of the strengthened beams do not exceed the 50 kip limit of the equipment. Also for the T-beam design, a failure mode of FRP rupture was intended for the strengthened beams as opposed to a failure mode of concrete crushing selected for the rectangular beam design.

The design was performed using a nonlinear analysis program based on the incremental deformation technique. In addition, ACI 440.2R-02 and Teng et al. (2001) procedures were followed to determine the likelihood of premature separation failure when using flexural reinforcement only. The beams that satisfied the actuator capacity limit and indicated that separation is likely to occur prior to ultimate flexural capacity are selected as dimensions to use, Table 3.1. The rectangular beams have a 6in x 12 in cross section (152 mm x 305 mm), Figure 3.1(b). They have a length of 16 ft (4877 mm) with a clear span of 15.5 ft (4724 mm). The main flexural reinforcement consists of 2 No. 5 bars with 2 No. 3 bars used for the compression steel just to provide a caging framework for the shear reinforcement, Figure 3.1(b). The beam has shear reinforcement consisting of No. 3 stirrups at 5 inches on center, Figure 3.1(b). The T beams have a 6in x 12 in web dimensions with the depth extending through the flange thickness, Figure 3.1(a).

The flange dimensions are 16 in width and 4 in thickness. The main flexural reinforcement is identical to that of the rectangular section. The compression steel consists of 4 No. 3 bars to hold the shear reinforcement caging.

Figure 3.1 Beam Specimen Cross-Section (a) T-Beam (b) Rectangular

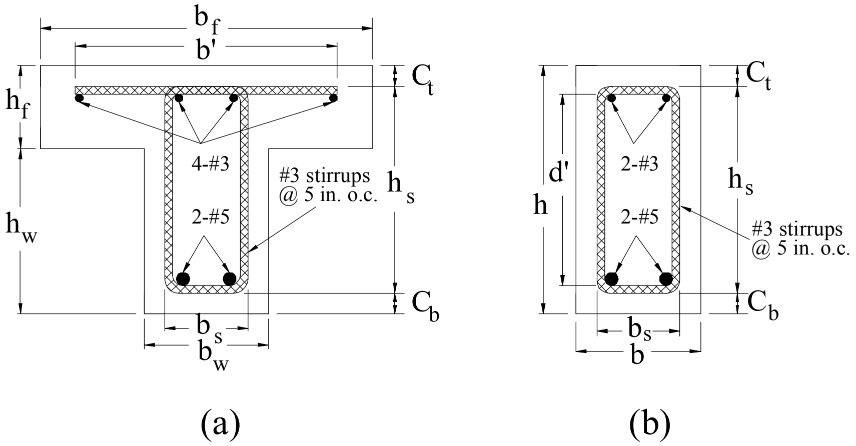

Table 3.1 Dimensions of Beam Specimen Cross-Section

b_f	16 in (406.4 mm)
h_f	4 in (101.6 mm)
b_w	6 in (152.4 mm)
h_w	8 in (203.2 mm)
C_t	1 in (25.4 mm)
C_b	1 in (25.4 mm)
h_s	10 in (254 mm)
b’	13 in (330.2 mm)
b_s	4 in (101.6 mm)

Material Properties

The concrete that was used in casting the six beams is ready mix with a mix design nominal strength of 5000 psi (34.5 MPa). While casting the beams, 30 cylinders were also prepared for the actual material testing on beam test dates. The cylinders were 4in. x 8in. which have a minor correction factor of 4-6% compared with the results of the standard 6in. x 12 in. cylinders (MoDOT 2004). The first set of 3 cylinders was tested on 11/28/06 the same day the control T beam (T1) was tested. The average compressive strength f'c was found to be 5455 psi (37.6 MPa). The second set of 3 cylinders was tested on 2/3/07 the same day the second T beam (T2) was tested. The average compressive strength f'c was found to be 4856 psi (33.5 MPa). The third set of 3 cylinders was tested on 2/23/07 the same day the third T beam (T3) was tested. The average compressive strength f'c was found to be 4730 psi (32.6 MPa). The fourth set of 3 cylinders was tested on 4/11/07 the same day the second rectangular beam (R2) was tested. The average compressive strength f'c was found to be 5203 psi (35.9 MPa). The fifth set of 3 cylinders was tested on 4/25/07 the same day the third rectangular beam (R3) was tested. The average compressive strength f'c was found to be 4804 psi (33.1 MPa). The last set of 3 cylinders was tested on 4/16/07 the same day the control rectangular beam (R1) was tested. The average compressive strength f'c was found to be 6732 psi (46.4 MPa). Table 3.2 summarizes the results of the cylinder testing.

Table 3.2 Summary of Cylinder Tests

Specimen	Cylinder #	Load, lbs (kN)	Stress, psi (MPa)
R1	1	87355 (389)	6951 (47.9)
	2	79121 (352)	6296 (43.4)
	3	87316 (388)	6948 (47.9)
	Average		**6732 (46.4)**
R2	1	62282 (277)	4956 (34.2)
	2	67021 (298)	5333 (36.8)
	3	66851 (297)	5320 (36.7)
	Average		**5203 (35.9)**
R3	1	61298 (273)	4878 (33.6)
	2	62352 (277)	4962 (34.2)
	3	57460 (256)	4573 (31.5)
	Average		**4804 (33.1)**
T1	1	68433 (304)	5446 (37.6)
	2	71717 (319)	5707 (39.4)
	3	65528 (292)	5212 (35.9)
	Average		**5455 (37.6)**
T2	1	61560 (274)	4899 (33.8)
	2	62100 (276)	4942 (34.1)
	3	59398 (264)	4727 (32.6)
	Average		**4856 (33.5)**
T3	1	61813 (275)	4919 (33.9)
	2	58234 (259)	4634 (32.0)
	3	58267 (259)	4637 (32.0)
	Average		**4730 (32.6)**

The material properties of the reinforcing steel were provided by the manufacturer to have a modulus of 29000 ksi (200,000 MPa) and yield strength of 70 ksi (483 MPa). The actual tensile testing of 8-inch long bar specimens was performed by KDOT research lab. The modulus and yield strength of the No. 3 bars were 30900 ksi and 65.31 ksi, respectively. These values represent the average test results of 3 samples. The modulus and yield strength of the No. 5 bars were 29641 ksi and 69.64 ksi, respectively. These values represent the average test results of 3 samples. Table 3.3 summarizes the properties of the reinforcing steel.

Table 3.3 Summary of Reinforcing Steel Properties

Bar Size	Specimen #	Stress, ksi (MPa)	Modulus, ksi (MPa)
#3	1	64.94 (447.8)	30157 (207933)
#3	2	65.96 (454.8)	32684 (225356)
#3	3	65.04 (448.5)	29858 (205871)
	Average	**65.31 (450.3)**	**30900 (213056)**
#5	1	69.55 (479.6)	28945 (199576)
#5	2	69.73 (480.8)	28326 (195308)
#5	3	69.63 (480.1)	31653 (218247)
	Average	**69.64 (480.2)**	**29641 (204375)**

The material properties of the Carbon Fiber Reinforced Polymer (CFRP) were provided by the manufacturer to have a modulus of 33000 ksi (227527 MPa) and strength of 550 ksi (3792 MPa) based on the fiber area. This corresponds to an ultimate strain of 0.017. The actual coupon tensile testing was performed based on ASTM Standard D3039. The modulus and strength averaged 8687 ksi and 111.4 ksi based on the laminate area. These values were the average of 5 specimens as required by the ASTM Standard. This corresponds to an ultimate strain of 0.0129. Table 3.4 summarizes the material properties for CFRP.

Table 3.4 Summary of CFRP Properties

Specimen	Ultimate Strength (ksi)	Modulus (ksi)	Ultimate Strain (με)
1	110.3	9099	12514
2	107.7	7628	14123
3	111.6	8631	12931
4	113.3	9484	11947
5	113.9	8764	12993
Average	**111.4**	**8687**	**12901**

Specimen Flexural Design

Two computer programs were used in the design and analysis of the beam specimens. Both programs are Microsoft Excel based. The first program is a beam analysis program developed by Calvin Reed, a former graduate student of Kansas State University. For this program, the beam section properties are entered as well as the concrete material properties. The program also gives the option to select the type of reinforcement, whether it is prestressed, mild steel, glass bars or FRP sheets. The program uses strain compatibility to determine the flexural response, ultimate flexural capacity and the flexural failure mode of the specimen. From the flexural analysis, the program determines a moment curvature relationship as well a load deflection response.

The second computer program that is used was developed by Kyle Larson, another former graduate student of Kansas State University. The program divides the beam into segments and uses a tri-linear moment-curvature response and strain compatibility to calculate the tension force in the FRP layer at each segment along the beam shear span. This tension force is compared to the tension force calculated for debonding using two separate methods. One of the methods of determining the debonding force is presented in ACI440.2R-02. The other method is presented by Teng et al. (2001). If the tension force determined from the computer program at ultimate flexural capacity is greater than the tension force calculated from the two methods, then CFRP debonding is likely. The tension force calculated for each of the rectangular and T sections is compared to the limiting tension force calculated based on ACI440 and Teng et al. methods and presented in Table 3.5.

Table 3.5 Tension Force in Flexural CFRP

Specimen	Tension Force in FRP, kip (kN)		
	Shear Program	Teng et al.	ACI440
R	44.2 (196.6)	28.0 (124.5)	51.4 (228.6)
T	86.1 (383.0)	43.0 (191.3)	51.4 (228.6)

Accordingly, the nominal load and moment capacity of the rectangular control beam, using the nonlinear beam analysis program, is 12.14 kips (54 kN) and 37 k-ft (50.2 kN.m), respectively. After adding five layers of V-Wrap C100 High Strength Carbon Fiber covering the entire bottom surface of the rectangular beam, the ultimate flexural capacity was computed to be 26.28 kips (116.9 kN) load or 77.72 k-ft (105.4 kN.m) using the nonlinear beam analysis program. This provided a target strengthening ratio of 2.16.

However, it is very likely for the CFRP sheets to debond prior to reaching the ultimate flexural capacity. ACI 440 model computes a higher FRP tension force than that required to achieve the full flexural capacity of the beam. Debonding is not likely according to this model. However, the model by Teng et al. 2001 indicates that the maximum tension force is 28.0 kips (124.5 kN). Accordingly, the beam is estimated to debond at a load of 20.5 kips (91.2 kN). To confirm these findings, rectangular beam 2 was strengthened with flexural CFRP only and was loaded until failure by premature debonding or flexure. On the other hand, rectangular beam 3 was strengthened with the same flexural CFRP along with U-wrap CFRP stirrups to anchor the external flexural reinforcement to accomplish the full flexural capacity of the strengthened beam.

The nominal load and moment capacity of the T beam, using the nonlinear beam analysis program, is 12.3 kips (54.7 kN) and 38.8 k-ft (52.6 kN.m), respectively. After adding five layers of V-Wrap C100 High Strength Carbon Fiber covering the entire bottom surface of the T beam, the ultimate flexural capacity was computed to be 38.7 kips (172.1 kN) load or 114.7 k-ft (155.5 kN.m). This provided a target strengthening ratio of 3.15. However, it is very likely for the CFRP sheets to debond prior to reaching the ultimate flexural capacity. ACI 440 model computes a lower tension force at debonding than that required to achieve the full flexural capacity, Table 3.5. According to the ACI 440 model, CFRP separation is likely to occur at a load of 29.2 kips (129.8 kN). The Teng et al. (2001) model also indicates that debonding is likely to ocurr prior to ultimate flexural capacity, Table 3.5. It yields a lower load of 26.5 kips (117.8 kN) at which separation failure is likely. Accordingly, the latter model is more conservative for both the rectangular and T sections. To confirm these findings for the T beams as well, T beam 2 was strengthened with flexural CFRP only and was loaded until failure by premature debonding. On the other hand, T beam 3 was strengthened with the same flexural CFRP along with U-wrap CFRP stirrups to anchor the external flexural reinforcement to accomplish the full flexural capacity of the strengthened beam.

Specimen Design against CFRP Separation

In an effort to prevent premature separation of flexural CFRP reinforcement, the beam specimens were reinforced with external CFRP U-shaped wraps. The design of these U-wraps was based on the ACI 318-05 model on shear friction. This model computes a maximum tension force in transverse reinforcement during horizontal shear cracking. A spacing of transverse CFRP U-wraps can then be obtained by limiting the level of CFRP tensile strain in the U-wraps. The first step is to obtain a maximum tension force in the flexural CFRP reinforcement by Equation (1)

$$T = E_f A_f \varepsilon_{fu} \tag{1}$$

where E_f is the elastic modulus of the CFRP fibers, A_f is the fiber area and ε_{fu} is the CFRP strain at ultimate flexural failure.

The horizontal shear force per unit length of shear span is then directly determined by Equation (2)

$$V_{hu} = \frac{T}{L_a} \tag{2}$$

where V_{hu} is the horizontal shear force per unit length, and L_a is the shear span.

Next, the shear friction model is used to find the tension force per unit length in the transverse CFRP direction by Equation (3)

$$T_{sf} = \frac{V_{hu}}{\mu} \tag{3}$$

where μ=1.4.

Finally, by using Equation (4), the area of the transverse CFRP flexural stirrups per unit length is determined by limiting the allowable tensile strain in the FRP stirrups. ACI 440.2R-02 limits the tensile strain to 0.00375 which is reduced to 0.003 to be more conservative. This corresponds to a CFRP tensile stress of 100 ksi (690MPa)

$$T_{sf} = \phi A_{vf} \varepsilon_{fe} E_f = 0.85 A_{vf} f_{fe} \tag{4}$$

where A_{vf} is the area of transverse CFRP per unit length of shear span used to prevent premature separation failure, which is calculated using Equation (5)

$$A_{vf} = 2 n t_f w_f \tag{5}$$

where t_f is the thickness of one layer, w_f is the width of each stirrup and n is the number of layers. Rearranging Equation (5) and using a spacing of 12 inches (304.8 mm), the width of each stirrup is determined. From previous calculations the maximum tension force in the flexural CFRP is 44.2 kips (196.6 kN) and 86.1 kips (383.0 kN) for the rectangular beam and the T-beam respectively. Based on the shear friction model, one layer of stirrups was used on the rectangular specimen with a spacing of 12 inches (304.8 mm) and a calculated width of 5.5 inches (139.7 mm). For the T-beam specimen, one layer of stirrups with a spacing of 12 inches (304.8 mm) required a stirrup width of 10 inches (254 mm). To prevent this from appearing as a continuous stirrup, two layers of stirrups were chosen with a width of 5 inches (127 mm). Complete calculations are shown in Appendix C -.

CHAPTER 4 - Specimen Construction

Construction of Formwork and Caging

The fabrication of all wooden formwork and steel rebar caging was done onsite in the Civil Engineering wood and steel shop. Since the plywood that is used for the bed of the formwork is available only in 4’ x 8’ sheets, the forms had to be fabricated in two halves then combined to create a 16 ft long form. Two-form bed halves were recovered from previous research projects and were in good condition to be used again. The additional form beds and form walls had to be fabricated from scratch in the shop. After the individual components are fabricated they are assembled outside behind the lab in the area of concrete casting.

The steel rebar used for the cages was donated by Ambassador Steel Inc. out of Kansas City, MO. The longitudinal steel was cut to length by the manufacturer. Also the steel stirrups for shear reinforcement were bent to the specified dimensions. The longitudinal reinforcement and the stirrups were tied together by hand using rebar ties. Figure 4.1 shows the finished rebar cage used for the rectangular shaped beams. To observe the strain in the re-bar during the testing process, strain gages were placed on the re-bar to be embedded in the concrete. Two strain gages were installed in each beam, at the mid-span of each bottom reinforcement bar as shown in Figure 4.2. 1 inch rebar chairs were tied to the bottom of the cages to lift the cage to the appropriate height in the formwork. Figure 4.3 shows the rebar cage inserted into the formwork and prepared for casting of concrete.

Figure 4.1 Rebar Cage Used for Rectangular Beams

Figure 4.2 Strain Gages Applied to Mid-span of Flexural Steel Reinforcement

Figure 4.3 Rebar Cages Inserted into Formwork

Casting of Specimens

The specimens were cast using 5000 psi ready mix concrete provided by Midwest Concrete Materials, a local concrete provider. A number of individuals helped out with the concrete casting including fellow graduate students, faculty and staff members. Along with casting the beam specimens, thirty concrete cylinders were cast to be tested along with each beam to determine an average compressive strength that should be considered for each of the beams. The beams and cylinders were allowed to cure for 28 days to reach their appropriate strength. Curing was done by lightly spraying the concrete each day and covering them with plastic to keep the moisture from escaping. Figure 4.4 through Figure 4.6 shows the casting of the beam specimens. Figure 4.7 shows the casting of the 4 x 8 inch concrete cylinders.

Figure 4.4 Casting of Rectangular Specimens

Figure 4.5 Casting of T-Specimens

Figure 4.6 Casting of T-Specimens

Figure 4.7 Casting of Concrete Cylinders

FRP Application

In preparation for the application of the FRP sheets, the surface of the beams where the FRP was to be applied had to be adequately cleaned and roughened. To do this, the surface of the beam was sandblasted using a portable sandblasting tank from the Civil Engineering Systems Lab, powered by a 15.5 cfm air compressor. The sandblasting procedure removes any oil and residue that could keep the epoxy from developing its full bond. It also removes any sharp imperfections on the concrete surface that could puncture the FRP and create premature FRP rupture. Figure 4.8 shows the sandblasting process on bottom surface of one of the rectangular specimens. As seen in Figure 4.9, there is a drastic change in the surface condition of the sandblasted section compared the section that is not sandblasted.

Figure 4.8 Sandblasting of Specimen Surface Prior to FRP Application

Figure 4.9 Comparison of Sanblasted (right) v. Non-Sandblasted Surface (left)

The CFRP that is used for strengthening of the specimens is a high strength carbon fiber called V-Wrap C100, which is provided by VSL Strengthening Products. The FRP comes in a roll of 20 inches (508 mm) wide and 164 feet long (50,000 mm). The flexural FRP was cut to the appropriate size of 6 in. (152.4 mm) wide by 15 ft. (4572 mm) long. The length of 15 ft was used to stop the FRP at 3 inches from the end of the clear span to allow adequate room for the bearing plates used during testing.

The epoxy that is used for saturating the carbon fiber and bonding it to the surface is V-Wrap 776 which was also provided by VSL Strengthening Products. V-Wrap 776 is a two-part epoxy composed of a self-priming putty filler (part B) and a saturant resin (part A). The epoxy is mixed by volume as 3 parts B to 1 part A. Before applying the CFRP strengthening system the beam specimen was first flipped up-side-down. This is not how the system would be applied in the field since it is not possible to flip a bridge girder. However, due to safety concerns in the lab we did not want anyone underneath the specimen while the CFRP was being applied. When applying the CFRP system to the beam, a layer of epoxy was first applied to the concrete surface where the FRP was to be placed. The epoxy was applied using a 3 inch ribbed roller with 1/16th inch groves shown in Figure 4.10.

Figure 4.10 Roller Used for Application of CFRP

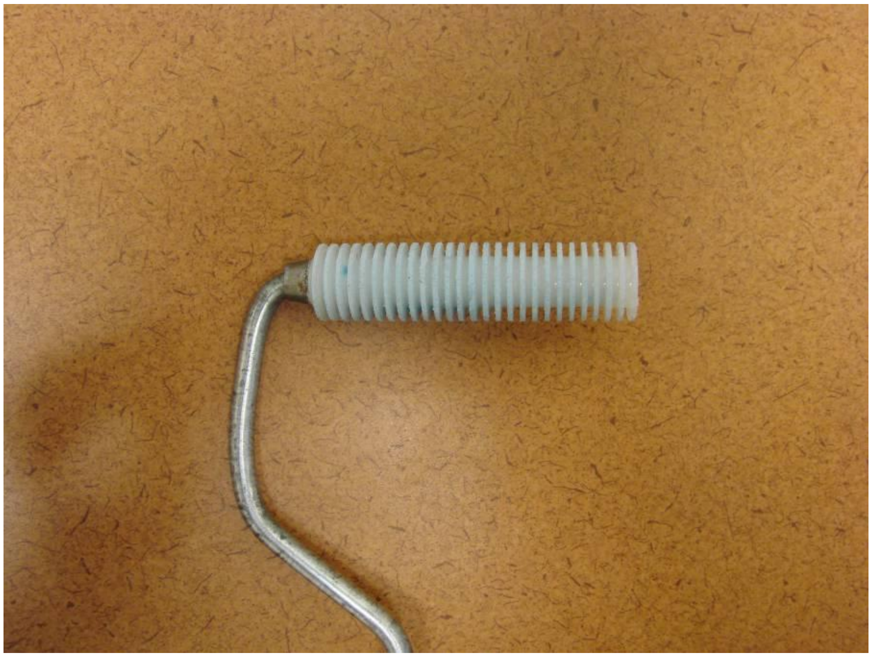

Following the layer of epoxy is the first layer of flexural CFRP. The CFRP is laid on the surface of the beam and the roller was used to draw the epoxy through the CFRP until the CFRP is fully saturated with epoxy. This first layer of CFRP was followed by another layer of epoxy. This process was repeated for all five layers of CFRP. After the final layer of CFRP was applied to the specimen, another layer of epoxy was applied to totally encapsulate the fibers to form a laminate. Figure 4.11 and Figure 4.12 show the application of the flexural CFRP reinforcement.

Figure 4.11 Application of First Layer of Flexural CFRP

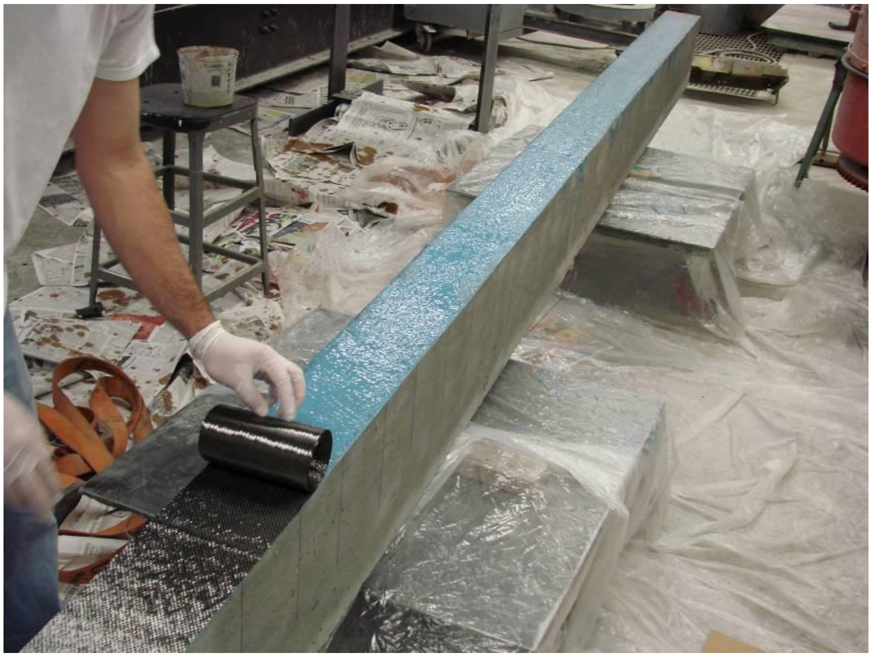

Figure 4.12 Saturating First Layer of Flexural CFRP

For the specimens that require U-wraps for shear reinforcement, the procedure is the same for the first five layers of flexural CFRP. Prior to applying the CFRP U-Wraps, a layer of epoxy is applied to the concrete surface where the CFRP U-wraps were applied. After the epoxy is applied, the fiber used for the U-Wrap is pulled tightly over the layers of flexural CFRP and is then rolled over with the roller to completely saturate the fiber and create a good confining effect. The process is repeated if two layers of U-Wraps are required followed by a final layer of epoxy to encapsulate the fibers and form a laminate. Figure 4.13 shows the application of the CFRP U-Wraps.

Figure 4.13 Application of CFRP U-Wraps

CHAPTER 5 - Experimental Program

Test Setup and Data Acquisition

The flexural tests were performed in the structural testing lab of Kansas State University. The beams were loaded in four-point bending using a 4-ft long steel spreader beam and a 50 kip hydraulic actuator. The actuator is controlled by a servo-hydraulic system called FlexTestGT from MTS system. The MTS system is a very precise data acquisition system which requires MTS certification in order to be properly operated.

The beams are simply supported with plates and rollers at the supports. The supports are placed 3 inches (75 mm) from the edge of the beam, providing a clear span of 15.5 ft (4724.4 mm). Figure 5.1 shows the experimental test setup.

Figure 5.1 Experimental Test Setup of Specimens

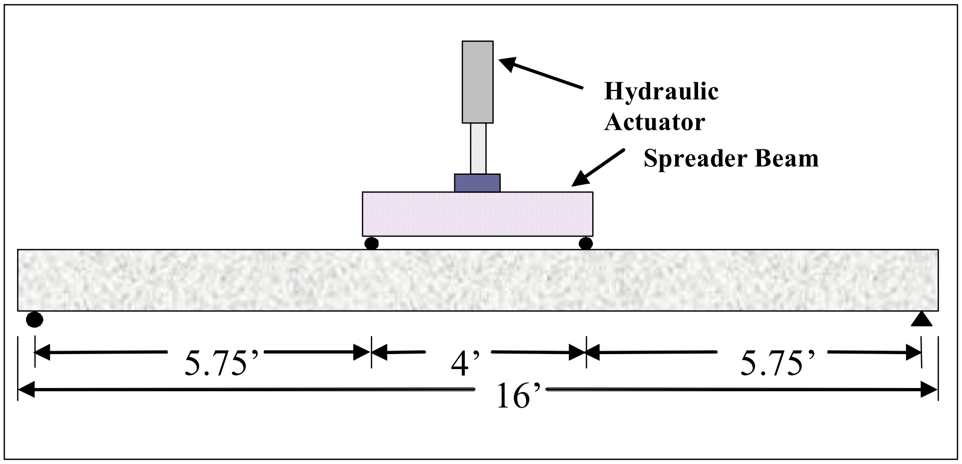

Two-four inch LVDT’s were placed on each side of the beam at mid-span. The LVDT’s were offset so that the second LVDT would engage just before the first one goes out of range if the beam was to deflect more than four inches. Two-350 Ω strain gages were installed on the main flexural bars, one gage on each #5 bar at mid span, prior to casting of the concrete to capture the yielding of steel. 150 Ω strain gages were also used for data collection. Three gages were placed along the side of the beam at mid-span. One was placed directly in the center of the beam and the other two placed at two inches from the top and bottom surfaces of the beam respectively. Two gages were also placed on the top surface of the beam at mid-span as well as two gages on the bottom surface of the beams strengthened with CFRP. All instrumentation was wired to a Megadac 200 channel data acquisition system. The data was recorded every 3 seconds. The beams were loaded at a load rate of 500 pounds per minute with the load recorded by a calibrated load cell. When the load was approximately 2 kips lower than the theoretical failure load, the system was programmed to switch to displacement control at a rate of 0.1 inch per minute. This guarantees capturing a limit load followed by a descending branch and leads to less catastrophic beam failure. The displacement was controlled by a 13-inch LVDT. After completing each test, the data was transferred from the data acquisition system into Microsoft Excel.

Test Results

Rectangular Control Beam (Beam R1)

The first beam tested in the series of rectangular beams is the rectangular control beam. It was determined from the flexural analysis program that the beam would fail at a load of 12.14 kips. The beam was loaded in load control at a rate of 500 pounds per minute. Cracking began taking place at a load of approximately 1500 pounds. At a load of 10 kips the control system switched to displacement control to capture the correct peak load. The rate of displacement was 0.1 inches per minute. The test results show that the beam failed at a load of 12.3 kips, which is very close to the theoretical value. The beam failed in a typical mode of steel yielding followed by crushing of concrete. Figure 5.2 shows beam R1 set up before the test was begun. Figure 5.3 shows beam R1 after failure indicating that the beam failed in a mode of concrete crushing.

Figure 5.2 Control Beam R1 Before Test

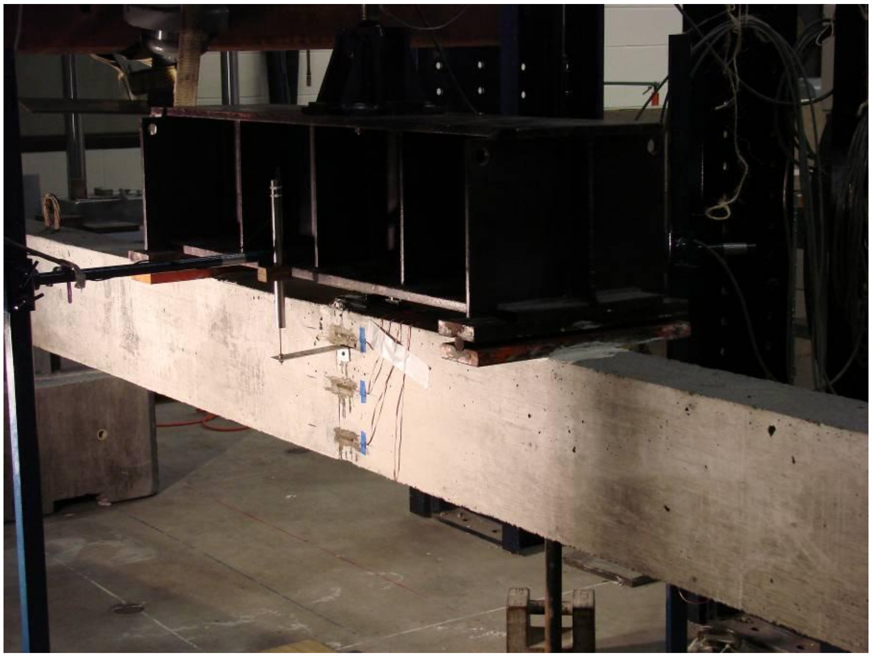

Figure 5.3 Control Beam R1 After Test

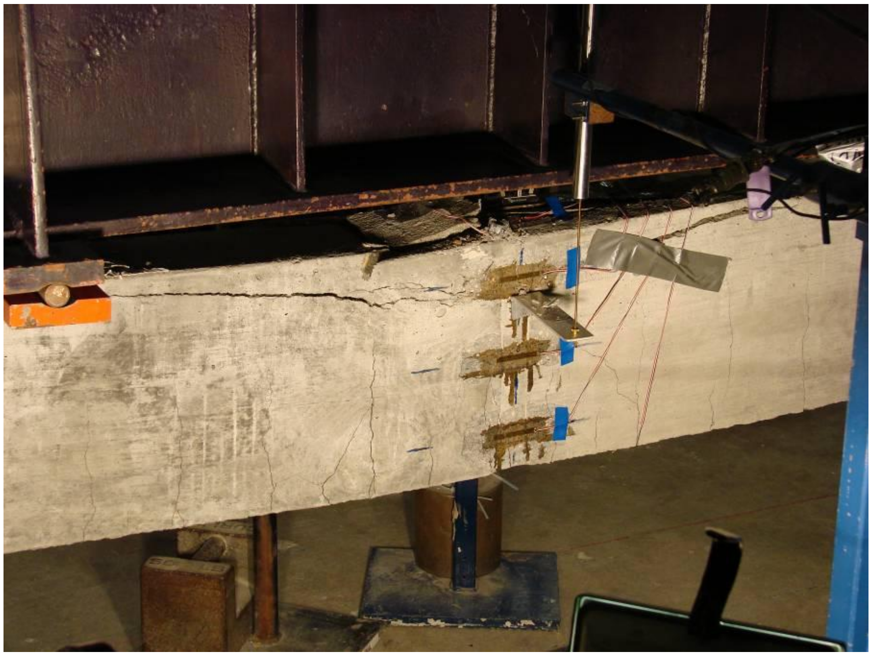

As a backup for the primary data acquisition unit, load and both mid-span LVDT's are recorded by MTS at a rate of one scan for every change in load of 50 pounds. For each test, the Megadac data acquisition system is run through multiple test procedures to ensure that it is recording the data. The deflection at the ultimate load was approximately 3.1 inches. After failure, the load dropped drastically to approximately 9.1 kips. This was caused by concrete crushing of the top cover followed by lowering the neutral axis within the confined core, Figure 5.4.

Figure 5.4 Lowering of Neutral Axis after Concrete Crushing

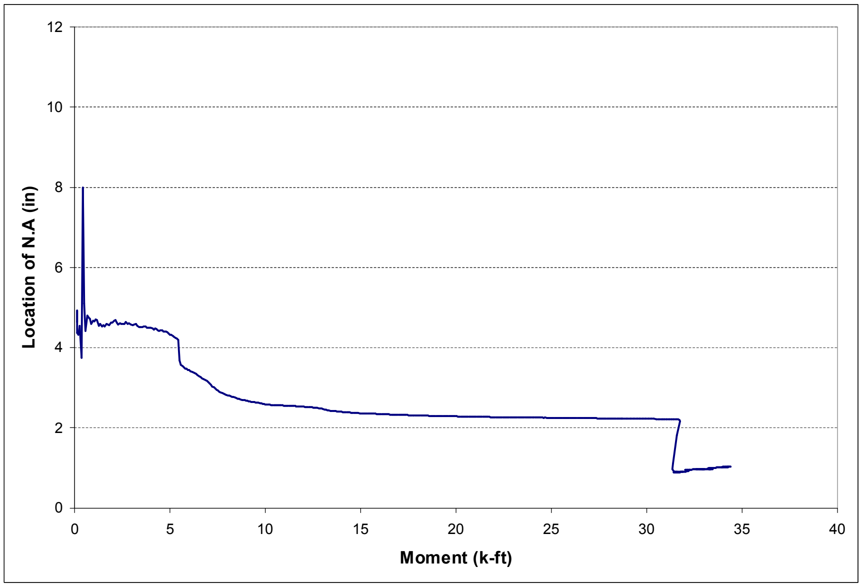

Figure 5.4 was generated from the load-strain curves at different heights of mid span section. The figure should show a drop in moment but the strain gages quit reading prior to the drop in moment. After this sudden load drop, the beam slowly began to gain additional strength by engaging the confined concrete. The beam continued to be loaded until the LVDT's went out of range at a final deflection of approximately 5.8 inches. Figure 5.5 shows the load-deflection results obtained from the Megadac data acquisition system and the MTS system.

Figure 5.5 Megadac and MTS Load-Deflection Comparison for Rectangular Control 3

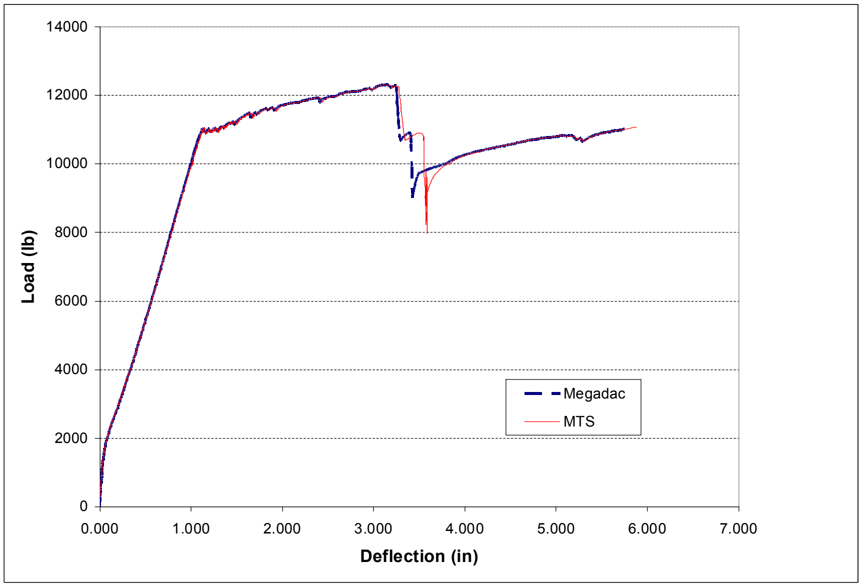

The data obtained from the two systems greatly agree with each other. Upon completion of the beam test, concrete cylinders were tested to determine if the compressive strength of the concrete was close to that of the rest of the beams. The three cylinders that were tested produced an average compressive strength of 6732 psi. This strength is higher than the strength of 5000 psi that was ordered for construction of the other beams.

Rectangular Beam with CFRP Only (R2)

The next step was to strengthen the second rectangular beam with flexural CFRP sheets at the bottom face. This beam was tested with five layers of CFRP sheets on the bottom in the longitudinal direction for flexural strengthening only. No U-wraps were applied to the beam since we wanted delamination to occur. For the test to be successful, delamination had to occur at a load higher than that of the control beam, which had an ultimate load of 12.3 kips. The CFRP was predicted to debond at a load of 20.5 kips using the Teng debonding equation. On the other hand, the ACI 440 model predicted that debonding wouldn't take place prior to flexural failure by concrete crushing. The beam was loaded in load control at a rate of 500 pounds per minute. At 12 kips the system was programmed to switch to displacement control at a rate of 0.1 inches per minute. 12 kips was chosen as the switch point because this is close to where the control beam failed and it was unknown how much of an increase in capacity would be achieved with the addition of the flexural CFRP. The load went well past that of the control beam. At a load of approximately 20 kips a lot of popping sounds started coming from the FRP which indicated the occurrence of local delamination. At a load of 24.6 kips (109.4 kN), the CFRP reinforcement delaminated with tremendous energy release. This load was a little higher than that predicted by Teng et al model (20.5 k or 91.2 kN), which shows that this approach is conservative. Figure 5.6 and Figure 5.7 show beam R2 before and after testing respectively. The failure mode was mostly debonding failure between FRP and the concrete substrate as indicated by Figure 5.7. However, there were two small locations where failure occurred due to separation of the entire 1 inch concrete cover as shown in Figure 5.8. Figure 5.9 shows the load-deflection results from this beam test.

Figure 5.6 Beam R2 Prior to Testing

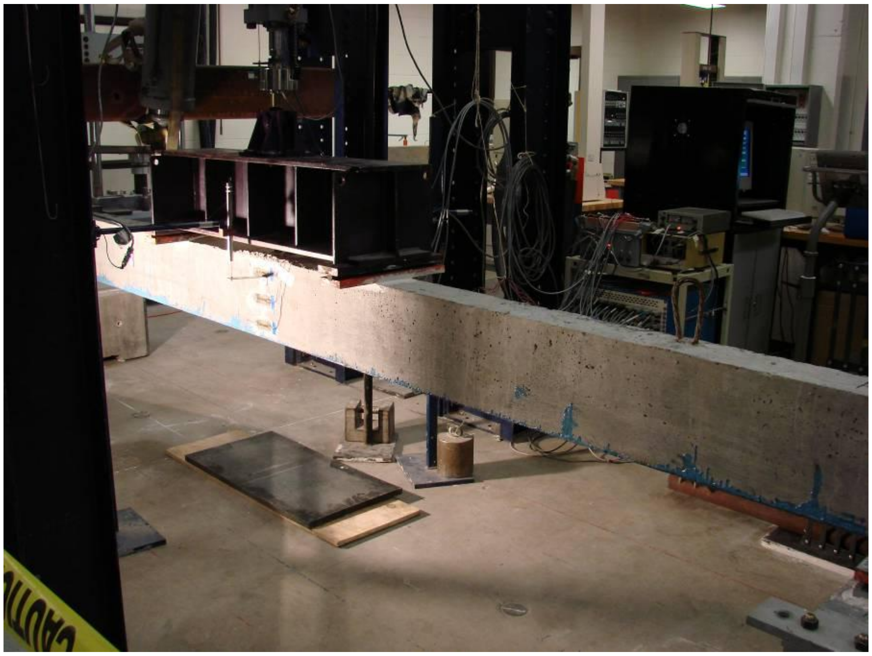

Figure 5.7 Beam R2 After Testing Showing Separation Failure of CFRP

Figure 5.8 Failure of Beam R2 by Separation of Concrete Cover

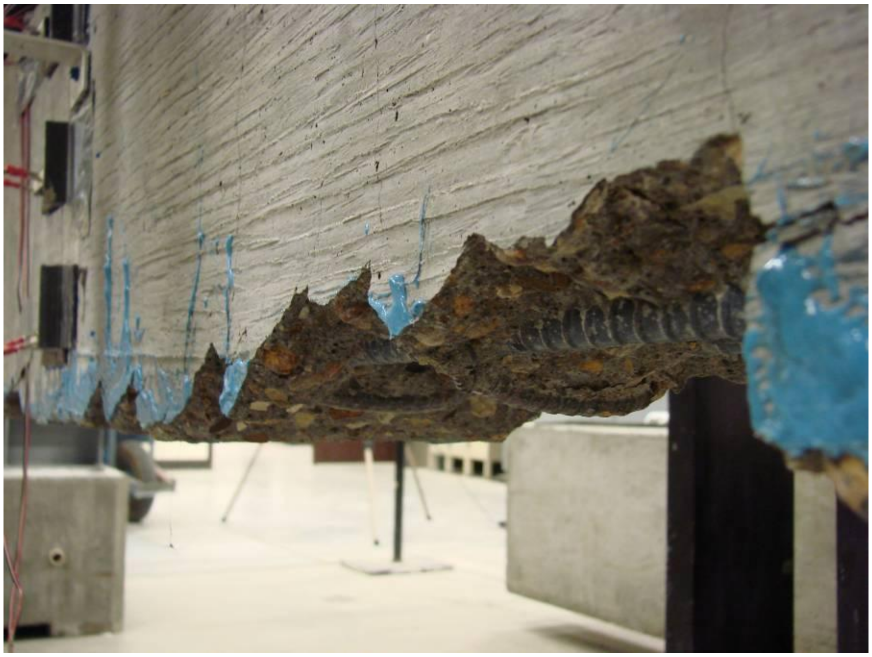

Figure 5.9 Load-Deflection for Rectangular Beam with flexural CFRP only

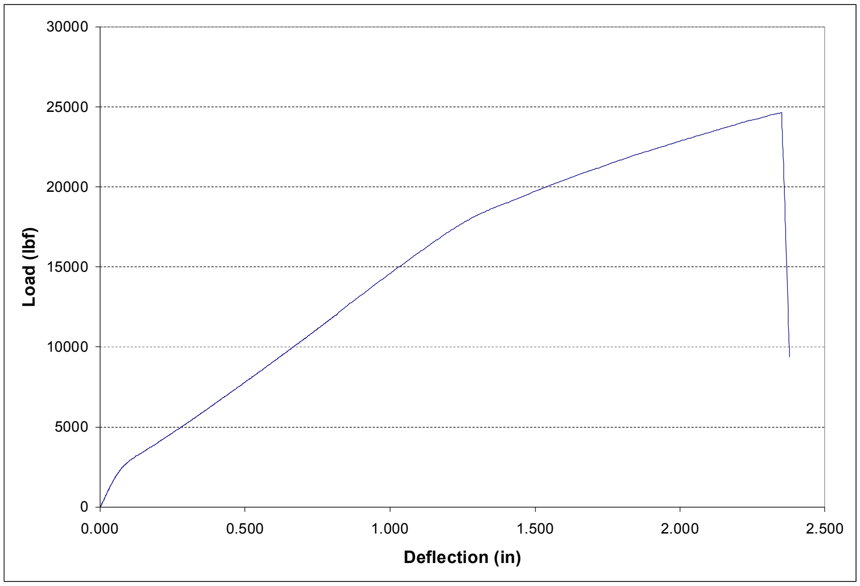

Rectangular Beam with CFRP and U-Wraps (R3)

The final beam to test in the series of rectangular beams is the beam with the full CFRP strengthening system applied. This beam was strengthened with the same five layers of CFRP on the bottom of the web as the beam (R2) for flexural strength increase, but it also had one layer of 5.5 inch wide U-shaped wraps around the web spaced at 12 in. on center, which is indicated in Figure 5.10 prior to testing.

Figure 5.10 Beam R3 Prior to Testing

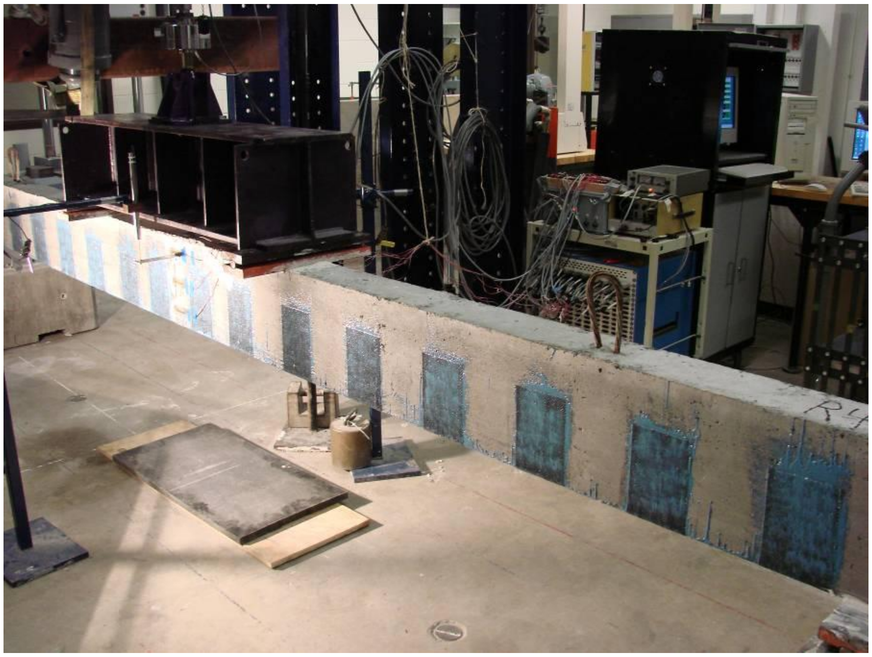

The purpose of these wraps was to provide shear resistance and hold the bottom layer of CFRP in place as it tried to debond. The beam was loaded in load control at the same rate of 500 pounds per minute. Once the test procedure was started, small cracking sounds were noticed around 6 kips, which seemed to be a sign of premature delamination. The noises continued throughout the test, but early separation never occurred. At a load of 20 kips the system was switched to displacement control at a rate of 0.1 inches per minute. The load passed the magnitude of 24.6 kips which is the ultimate separation load from the last test without the U-wraps (R2). This was an excellent indication that the U-wraps performed as they were supposed through inducing resistance by shear friction once the resistance by cohesion is lost. The failure mode was initiated by the crushing of concrete cover. The beam reached an ultimate load of 27.1 kips (120.5 kN) when the CFRP ruptured, as shown in Figure 5.11. A closer view of the flexural CFRP rupture is shown in Figure 5.12. This load was slightly higher than the analysis value of 26.28 kips (116.9 kN) that was predicted to be associated with the concrete extreme compression fiber reaching a strain of 0.003. Figure 5.13 shows the load-deflection relationship that was obtained from this test.

Figure 5.11 Beam R3 After Testing

Figure 5.12 Rupture of Flexural CFRP on Beam R3

Figure 5.13 Load-Deflection Response for Rectangular Beam R3

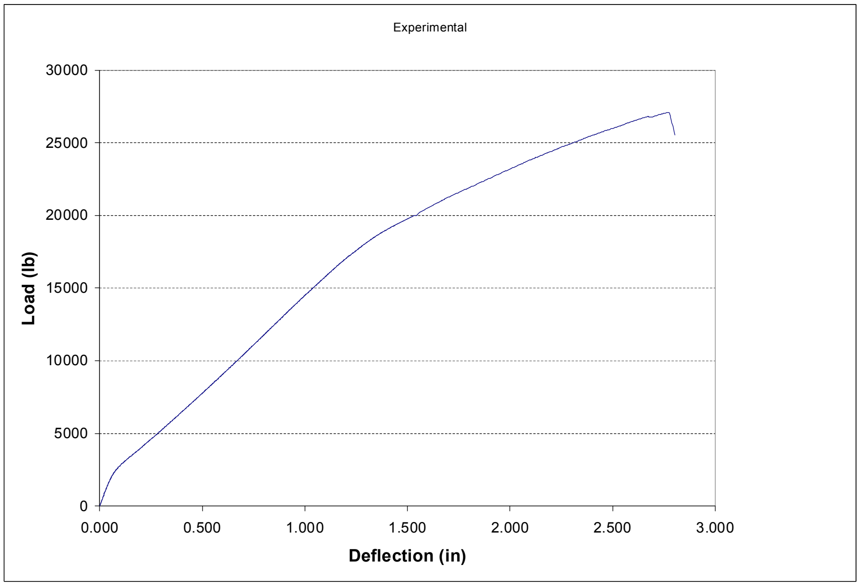

Infrared Thermography

By tapping the flexural CFRP with a hard object, it was observed that the FRP had debonded between the locations of U-wraps. In an effort to verify that the flexural CFRP has lost cohesion and only being held in place by the U-wraps, a more sophisticated method other than visual inspection was used. Infrared thermography was performed on a section of the rectangular beam R3. Infrared cameras can detect changes temperature changes in a specimen by recording different levels of thermal energy. The theory is that by heating the beam specimen, areas of delamination will emit different levels of thermal energy. The infrared camera that is used is called ThermaCam PM675 from FLIR Systems. The camera was loaned out from KDOT for this research.

To perform the infrared thermography, the beam section was allowed to sit in a temperature controlled environment for a long enough period for all elements of the section to reach the same temperature. The beam was set on its side with the bottom CFRP facing the camera. The camera was set up at a distance of 8 ft. from the beam. Two-500 watt halogen lamps were placed at a distance of 3 ft. from the beam to be used at the heat source. Figure 5.14 shows the setup of the experiment. An infrared thermograph was taken at the start of the test at the instant the heat source was applied as shown in Figure 5.15. This shows the constant levels of thermal energy throughout the specimen. The beam was allowed to heat up for 2 minutes at which time another infrared thermograph was taken, Figure 5.16. The heat source was then removed as the beam was allowed to cool for 5 minutes with infrared thermographs taken every 30 seconds. Figure 5.17 shows the beam right after the heat source was removed and the beam was allowed to cool. Figure 5.18 shows the beam half way through the cool down process. This figure shows that the areas of FRP between the U-wraps are cooling down slower than the areas of U-wraps, indicating that delamination has occurred in this area. Another thermograph was taken at the end of the test showing that all areas of the beam specimen have reached an equilibrium temperature as shown in Figure 5.19. This experiment indicates that by use of infrared thermography, areas of delamination can be detected where visual inspection can not be conclusive.

Figure 5.14 Infrared Thermography Setup

Figure 5.15 Infrared Thermograph Taken at Start of Test.

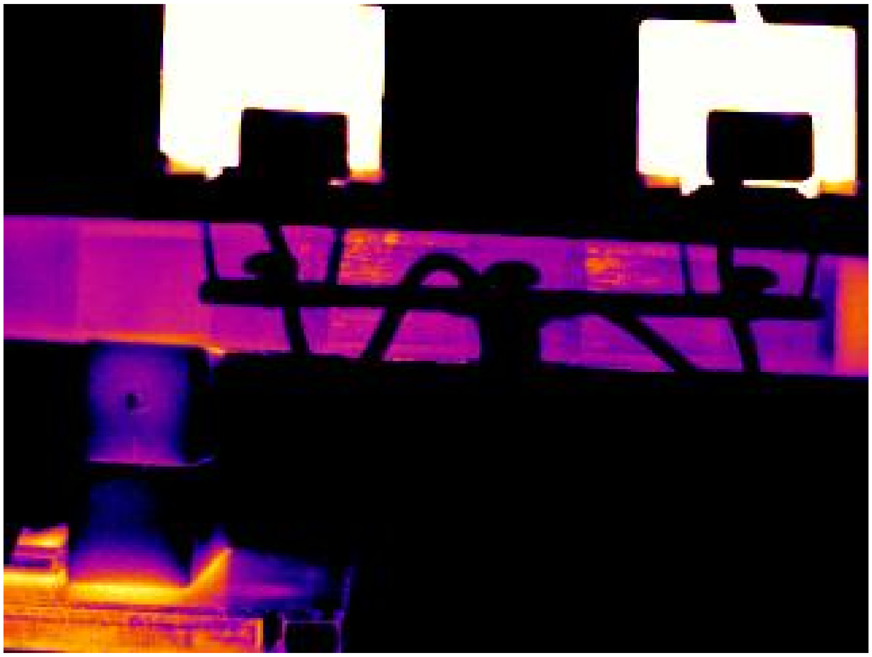

Figure 5.16 Infrared Thermograph at end of Warm-up Period

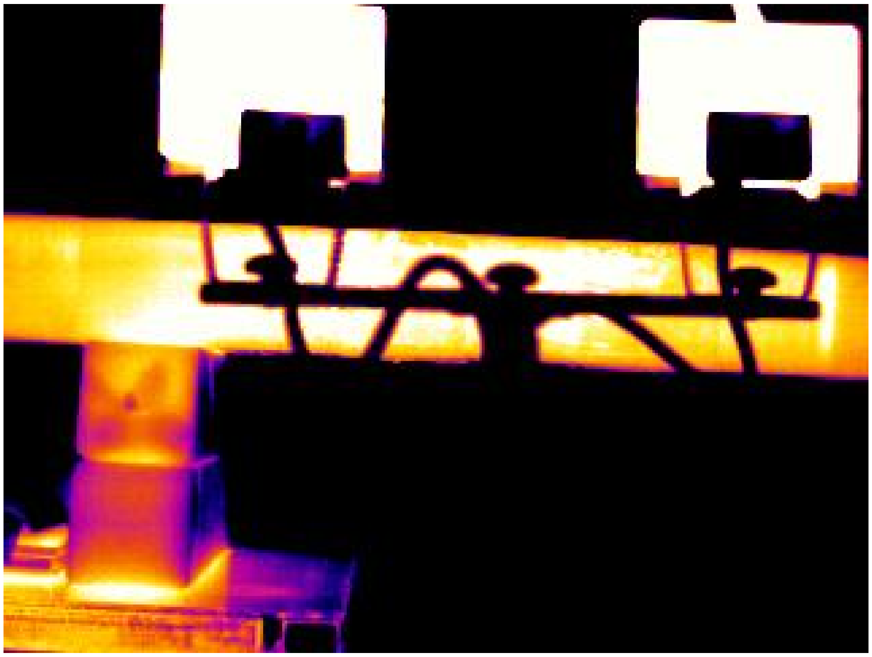

Figure 5.17 Infrared Thermograph at Beginning of Cool Down

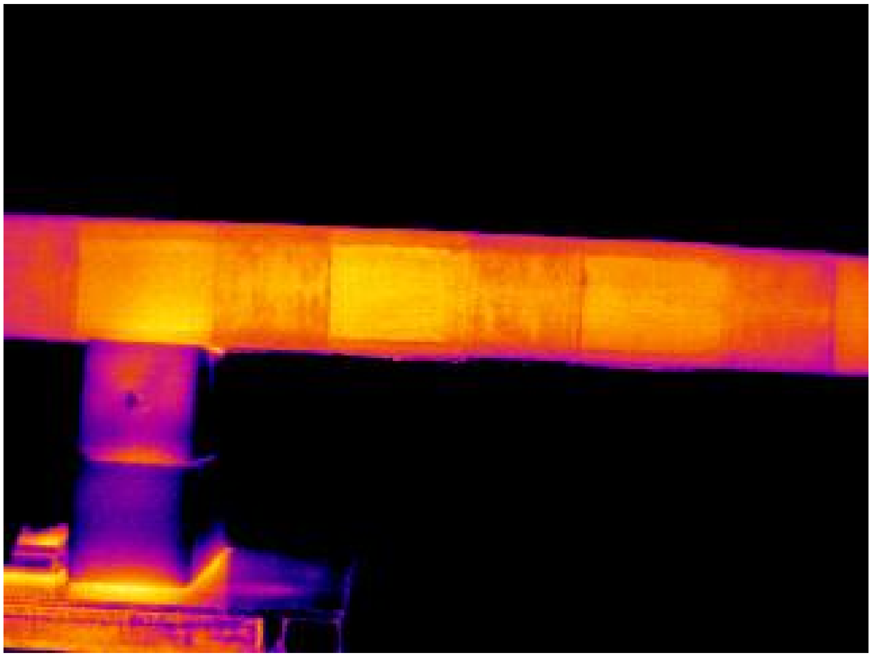

Figure 5.18 Infrared Thermograph Halfway Through Cool Down

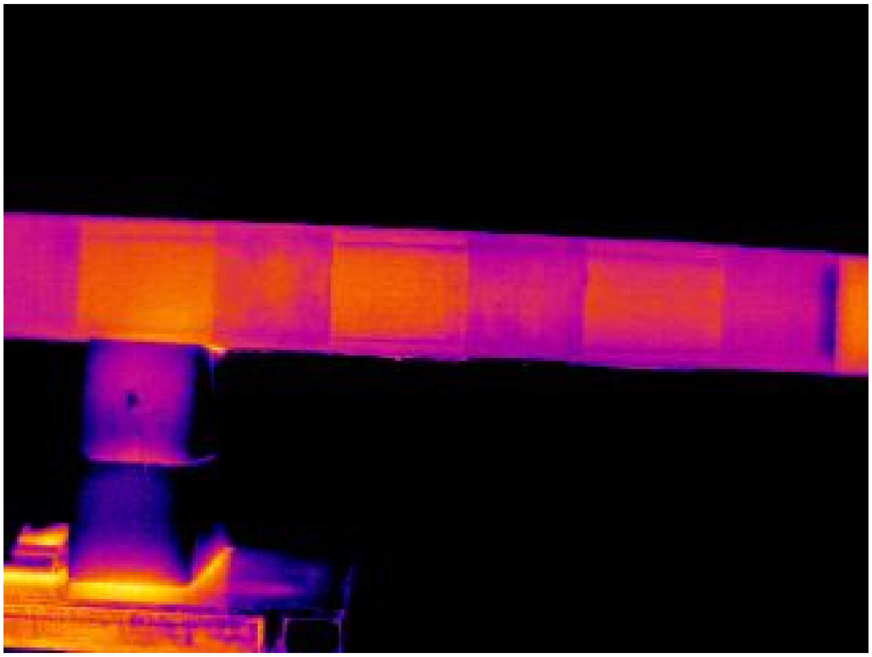

Figure 5.19 Infrared Thermograph at End of Cool Down

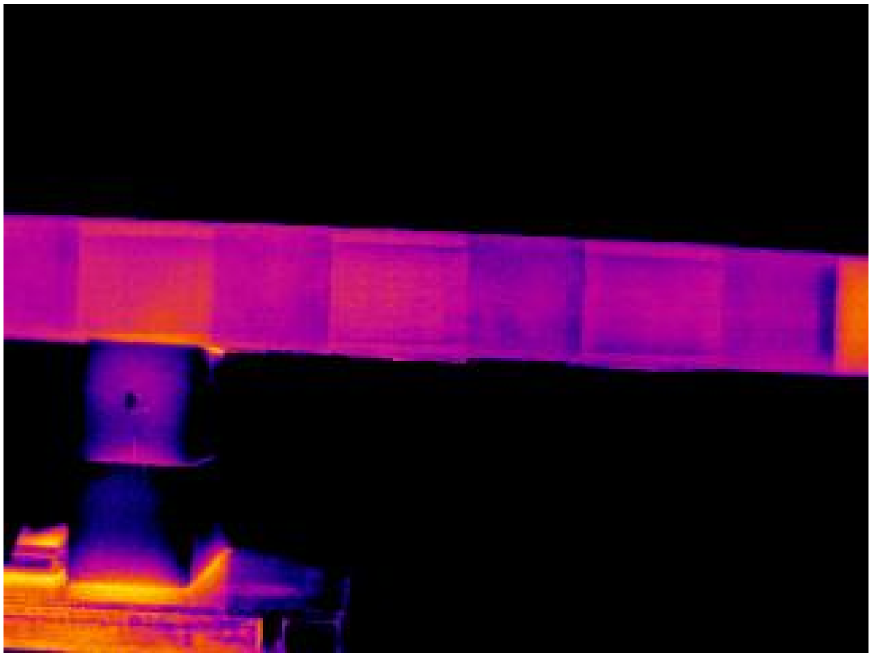

Comparison of Rectangular Specimen Behavior

The experimental results from the series of rectangular beams are demonstrated above. The ultimate loads are very close to those predicted and the CFRP U-wraps were shown to perform as intended. The CFRP reinforcement provided significant additional flexural capacity ($\frac{27.1k}{12.3k} = 2.2$) while reducing the deflection. Figure 5.20 shows the load-deflection comparison of the control beam, the beam with flexural FRP only and the beam with flexural FRP and U-wraps. There is much similarity in the load-deflection response of the beam with and without U-wraps except for the ultimate load. Table 5.1 summarizes the experimental results for the rectangular beams.

Figure 5.20 Comparison of Experimental Load-Deflection Curves for Rectangular Beams

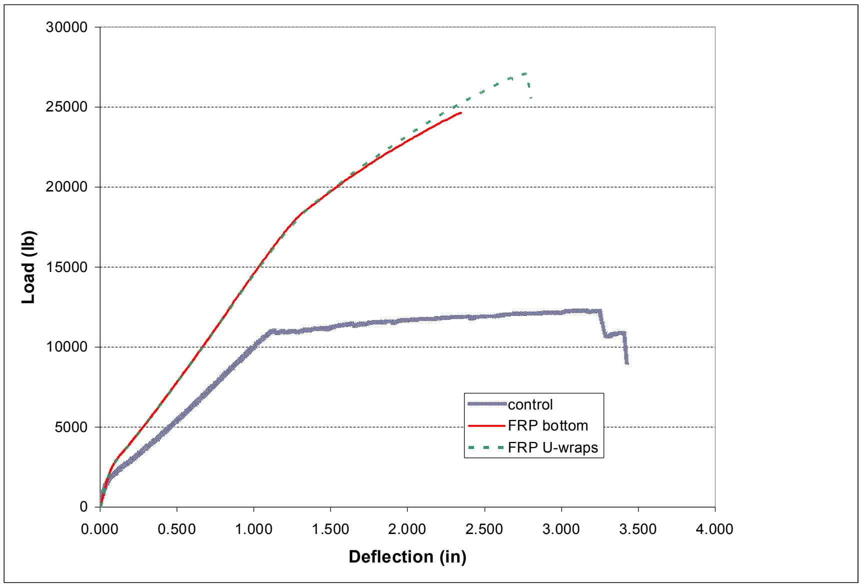

Table 5.1 Summary of Experimental Results for Rectangular Beams

Specimen	External Reinforcement	Ultimate Load (kips)	Deflection (inches)	Load Increase (%)	Failure Mode
R1 (Control)	None	12.3	3.25	N.A.	Concrete Crushing
R2	Flexural FRP	24.6	2.35	200	FRP Separation
R3	Flexural FRP with U-wraps	27.1	2.78	220	FRP Rupture

Control T-Beam (T1)

The first specimen tested in the series of T-shaped beams is the control beam (T1). The beam was loaded in load control at a rate of 500 pounds per minute. At a load of 11 kips, the system was switched to displacement control at a rate of 0.1 inches per minute. The beam was predicted to fail at a load of approximately 12.33 kips (54.8 kN). Flexural cracks began showing up at a load of approximately 4.3 kips (19.1 kN). The beam failed at a load of 15.5 kips. Figure 5.21 shows beam T1 set up prior to testing. Figure 5.22 shows the beam at maximum deflection just before failure of concrete crushing which is shown in Figure 5.23.

Figure 5.21 Control Beam T1 Before Testing

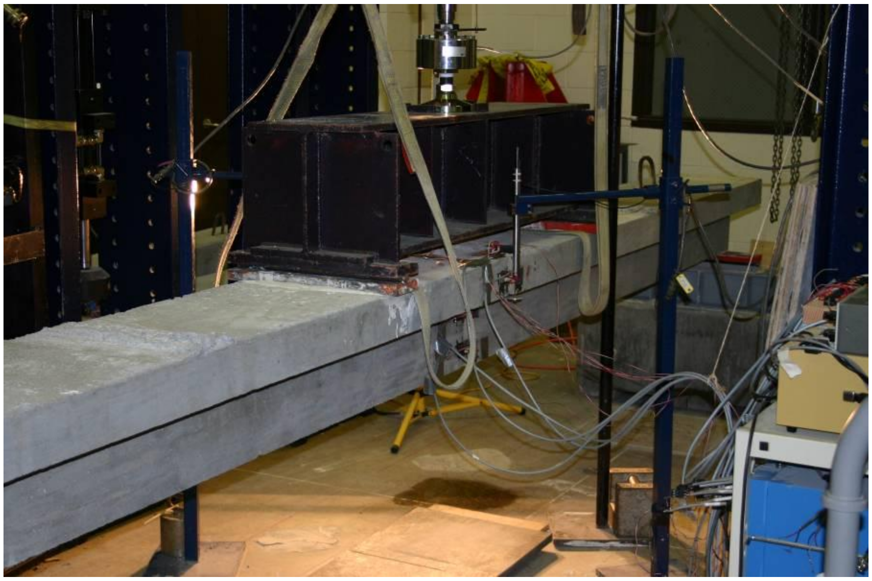

Figure 5.22 Beam T1 Just Prior to Failure

Figure 5.23 Beam T1 After Concrete Crushing Failure

This load is noticeably higher than the load of 12.33 kips that was predicted. To explain the difference between the experiment and the prediction, another analysis was performed accounting for concrete confinement effect and steel post yielding stiffness. The high deformation in the steel engaged strain hardening that was not included in the first analysis. The latter analysis yielded a failure load of 15. 33 kips (68.2 kN) which is much closer to the experimental ultimate load. At the failure load, the deflection at mid-span was 7.0 inches and the failure mode was concrete crushing. Figure 5.24 shows the load-deflection relationship that was obtained from the test of the control beam specimen.

Figure 5.24 Load-Deflection for Control Beam Specimen T1

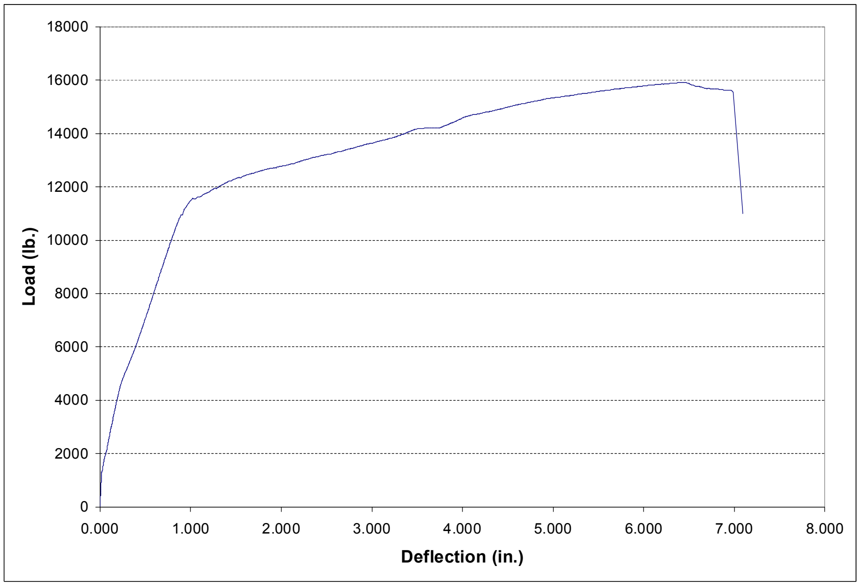

T-Beam with Flexural CFRP only (T2)

The next beam tested is the T-beam specimen with five layers of flexural CFRP reinforcement on the bottom surface of the beam in the longitudinal direction. For the test to be considered a success, the beam had to fail at a load higher than that of the control beam. Using the Teng et al model of predicting FRP debonding, it was estimated that the beam would fail at a load of approximately 26.5 kips (117.9 kN). Using the ACI 440 model, it was estimated that the beam would fail by FRP debonding at approximately 29.2 kips (129.8 kN). Figure 5.26 shows beam T2 set up before testing began. The beam was loaded in load control at the same load rate of 500 pounds per minute. At a load of 15 kips, the control system was switched to displacement control at a rate of 0.1 inches per minute. After the beginning of the test, a load of 6 kips was reached when a strange event occurred. For some reason that is still unknown, a vibration was introduced into the system causing the beam to vibrate at a very high frequency. This vibration was extremely fast and shock the entire testing lab. The hydraulic system was immediately shut down to prevent any damage from occurring. After close investigation of the beam, the beam supports, and all of the gages and equipment, it was determined that no damage was caused. Since the Megadac data acquisition system records data at a specific time interval it was unable to capture the vibration, but the MTS data acquisition system is set up to record data every time there is a change of 500 pounds. This captured the vibration which is shown in Figure 5.25 in the load-deflection plot. By looking at the plot, the vibration reached a peak amplitude of approximately 20 kips, which is getting very close to failure, but since this occurred at such a high frequency there was no damage caused.

Figure 5.25 Vibration experienced by Specimen

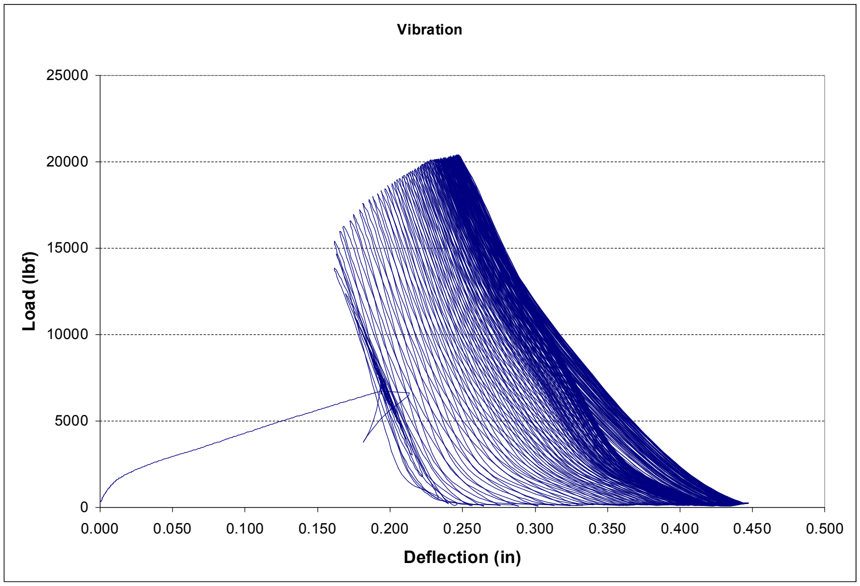

After the test was restarted, everything performed perfectly. At a load of approximately 18 kips some popping sounds were heard indicating areas of local debonding. The beam reached a load of 25.5 kips (113.4 kN) when the CFRP debonded with tremendous energy release. This failure load was very close to that predicted by Teng et al model of 26.5 kips (117.9 kN). At the failure load, the deflection at mid-span was approximately 2 inches which is much smaller than the 7 inch deflection of the control beam. The CFRP detached in the same way it separated on the Rectangular beam R2 with mostly debonding failure at the interface with small areas of concrete cover delamination shown in Figure 5.27 and Figure 5.28. The load-deflection relationship for this beam specimen is shown in Figure 5.29. The CFRP reinforcement performed well by increasing the capacity of the beam by approximately 165 % ($\frac{25.5}{15.5} = 1.65$) and decreasing the deflection by 350%.

Figure 5.26 Beam T2 Set Up Before Testing

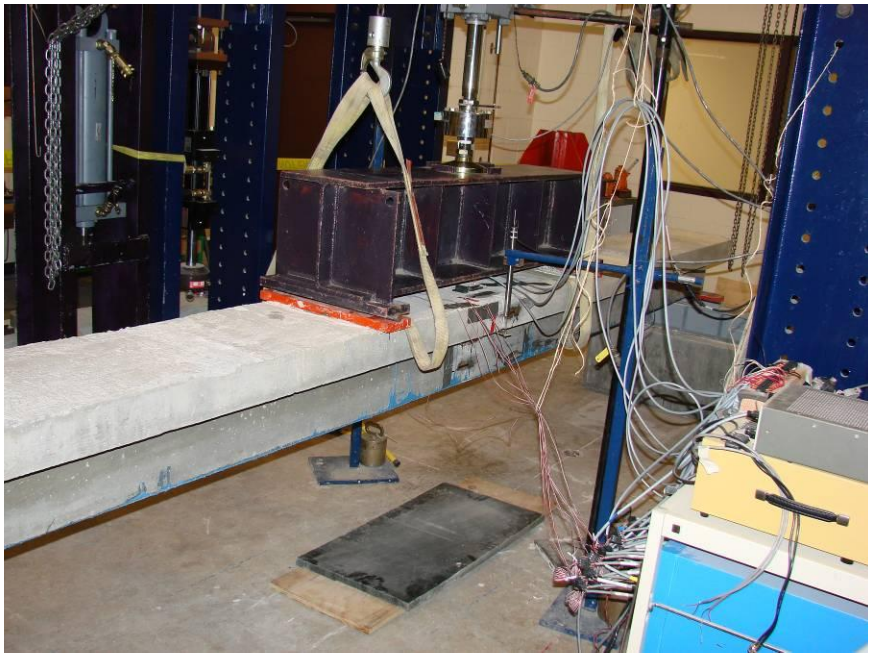

Figure 5.27 Failure of Beam T2 by Separation of Flexural CFRP

Figure 5.28 Failure of Flexural CFRP by Separation of Concrete Cover

Figure 5.29 Load-Deflection Response for T-Beam with Flexural CFRP only (T2).

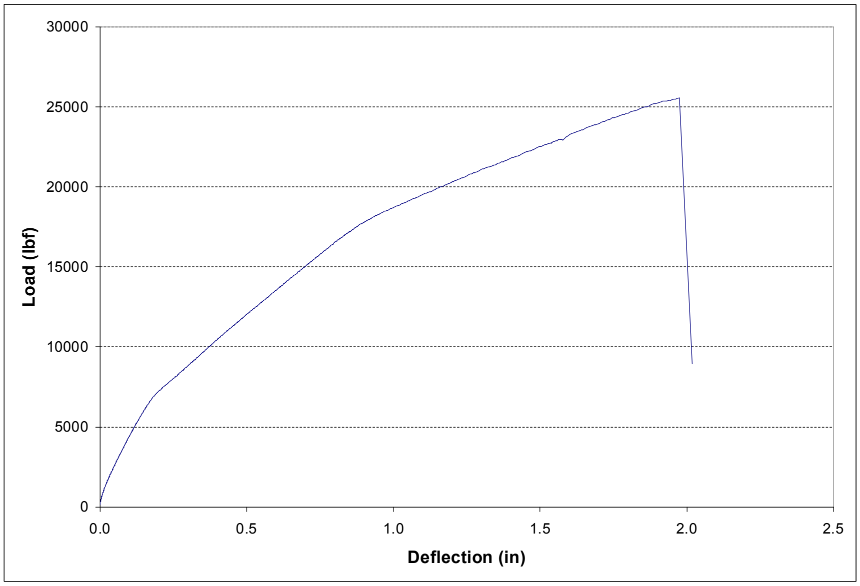

T-Beam with Flexural CFRP only and U-Wraps (T3)

The last beam tested in the series of T-beam specimens is that with the full CFRP strengthening system applied. This beam was strengthened with the same five layers of CFRP on the bottom surface of the web for flexural strength increase and it also had two layers of 5 inch wide U-shaped wraps around the web spaced at 12 in. on center. The purpose of these wraps was to provide shear resistance and anchor the bottom layers of CFRP in place as they tend to debond. This beam was loaded at the same rate as the previous specimens (i.e. 500 pounds per minute). The MTS system was programmed to switch to displacement control at a load of 36 kips. Figure 5.30 shows beam T3 set up prior to testing.

Figure 5.30 Beam T3 Before Testing Began

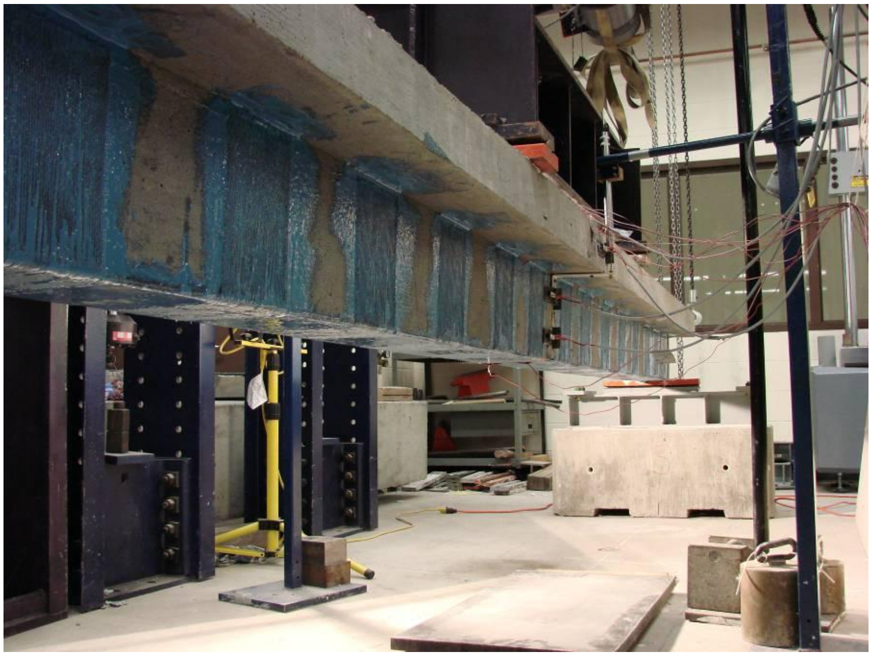

Once the test was started, small popping sounds were heard at around 5 kips which seemed to be a sign of premature debonding. The noises continued throughout the test, but early separation never occurred. At a load of 26 kips (116 kN), about the load at which separation occurred on beam T2, debonding of the flexural CFRP from the beam was seen in between the U-wraps shown in Figure 5.31. This was an excellent indication that the U-wraps were performing as they were supposed to by providing resistance to separation by shear friction. The beam reached an ultimate load of 33.5 kips (149 kN) when the CFRP ruptured, shown in Figure 5.32. The failure of this beam was more drastic than the previous beams since failure occurred prior to the system switching to displacement control. Figure 5.33 shows a close up of the ruptured flexural CFRP at mid-span of beam T3.

Figure 5.31 Debonding of Flexural CFRP between the U-Wraps

Figure 5.32 Failure of Beam T3 by Rupture of Flexural CFRP

Figure 5.33 Rupture of Flexural CFRP at Mid-Span

This test provided a strength increase ratio of 2.16 ($\frac{33.5}{15.5} = 2.16$) over the control beam. This load was lower than the predicted value of 38.7 kips with a failure mode of CFRP rupture. The difference is attributed to the fact that CFRP had no composite action in between the U-wraps causing it to reach rupture sooner. At any rate, the U-wraps that were placed on the beam performed as intended and didn't allow for separation to occur. Figure 5.32 and Figure 5.33 show the failure mode of FRP rupture. At the failure load, the deflection was approximately 3.1 inches. The load-deflection relationship for this beam is shown in Figure 5.34.

Considering ACI 440.2R-02 case of no debonding with ($k_m = 0.9$) and an FRP reduction factor ($\psi_f = 0.85$), the predicted value of load is 33.7 kips which matches very well the experimental value of 33.5 kips. This clearly indicates that the ACI 440.2R-02 offers an appropriate design method.

Figure 5.34 Load-Deflection Response for T-Beam with Flexural CFRP and U-Wraps

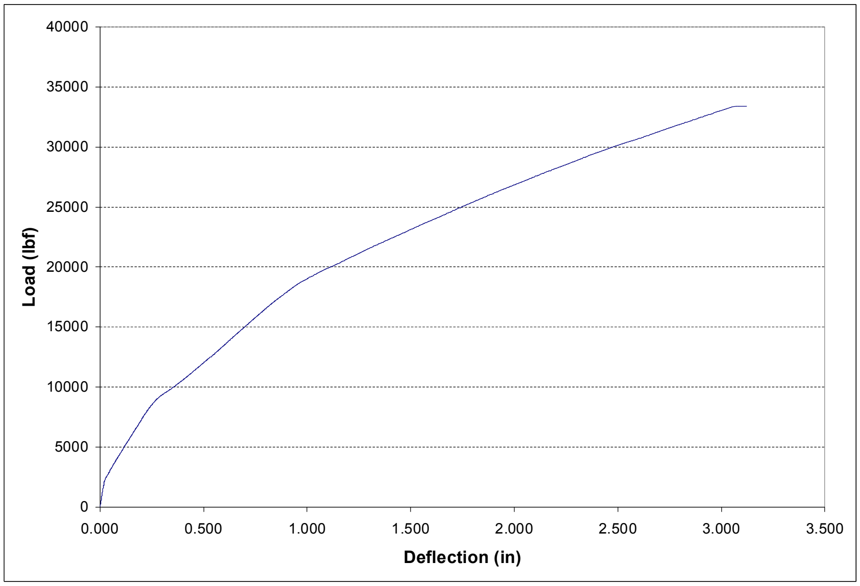

Comparison of T-Beam Specimen Behavior

The experimental results from the series of T-Beam specimens were just as expected. The CFRP reinforcement provided noticeable additional flexural capacity while reducing the deflection. Figure 5.35 shows the load-deflection comparison of the control beam, the beam with flexural FRP only (T2) and the beam with flexural FRP and U-wraps (T3). The response of T2 and T3 is identical except for the ultimate loads. Table 5.2 summarizes the experimental results for the T-beam specimens.

Figure 5.35 Summary of Experimental Results for T-Beam

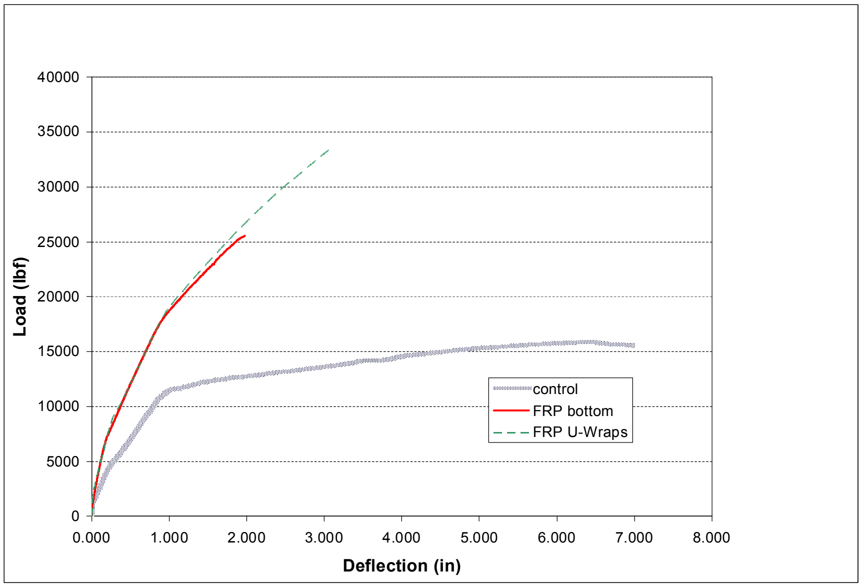

Table 5.2 Summary of Experimental Results for T-Beams

Specimen	External Reinforcement	Ultimate Load (kips)	Deflection (inches)	Load Increase (%)	Failure Mode
T1 (Control)	None	15.5	7.0	N.A.	Concrete Crushing
T2	Flexural FRP	25.5	2.0	165	FRP Separation
T3	Flexural FRP with U-wraps	33.5	3.1	216	FRP Rupture

CHAPTER 6 - Analysis

Overview of Analysis Programs

Two computer programs were used in the design and analysis of the lab specimens. The first program is a nonlinear beam analysis software developed under a previous research program by Calvin Reed, a former graduate student of Kansas State University. This program gives the user the option of selecting the cross-section type, either rectangular or T-shaped, and the appropriate dimensions are entered. The program then allows the user to select the loading type by choosing three-point bending, four-point bending or a uniform load. Material properties are then input such as concrete strength and reinforcement. For the reinforcement properties, the user selects the type of reinforcement be it mild steel, prestressed steel, glass bars, or FRP sheets. For the types of reinforcement used, the size and location is input. The model predicts the flexural response of the specimen by using strain compatibility and incremental deformation techniques based on the specimen geometry and material properties. From the experimental results, it was observed that the ultimate load of the control T beam (T1) was higher than the load predicted using this analysis program. Accordingly, a modified version of the analysis program was used to include the effect of concrete confinement and post yield hardening of the steel bars. Using this modification, the user is allowed to input material properties of transverse steel which produces the confinement effect on the stress-strain curve. The model uses an iterative method to determine the moment curvature relationship. A bending moment is computed once equilibrium is satisfied for a section. A corresponding curvature is determined for this moment from the strain profile at that section. A load deflection relationship is then determined from the moment curvature relationship. An incremental analysis is performed by dividing the specimen into many small segments. A moment is calculated for each segment corresponding to the applied load. The corresponding curvature is then determined using the moment curvature relationship. The deflection is then calculated using the moment area method.

The second computer program that is used in the analysis was developed by Kyle Larson, a former graduate student of Kansas State University. The program divides the beam into sections and calculates the tension force in the FRP layer at each section. This tension force is compared to the tension force calculated for debonding using two separate methods. One of the methods of determining the debonding force is presented by the American Concrete Institute (ACI440.2R-02). In this method, the FRP debonding is predicted by limiting the maximum strain in the FRP. This maximum allowable strain in the FRP layer is computed as a fraction of the ultimate rupture strain of the FRP ($\kappa_m \varepsilon_{fu}$) as shown in Equation (6)

$$\varepsilon_{fe} = \kappa_m \varepsilon_{fu} \tag{6}$$

where κ is the bond-dependent coefficient given by Equation (7)

$$\kappa_m = \begin{cases} \dfrac{1}{60\varepsilon_{fu}}\left(1 - \dfrac{nE_f t_f}{360,000}\right) \le 0.90 \; for \; nE_f t_f \le 180,000 \\ \dfrac{1}{60\varepsilon_{fu}}\left(\dfrac{90,000}{nE_f t_f}\right) \le 0.90 \; for \; nE_f t_f > 180,000 \end{cases} \tag{7}$$

and ε_{fu} is the ultimate strain in CFRP given by Equation (8)

$$\varepsilon_{fu} = \frac{f_f}{E_f} \tag{8}$$

By determining the stress in FRP, the maximum allowable tension force in the FRP is found by taking the CFRP area times elastic modulus of the CFRP times the ultimate CFRP strain shown in Equation (9)

$$T = E_f \varepsilon_{fe} A \tag{9}$$

The value of *T* computed for the rectangular beam is 51.39 kips (228.6 kN) compared to T = 44.22 kips (196.7 kN) determined by attaining full flexural capacity. The value of T computed for the T beam is 51.39 kips (228.6 kN) compared to T = 86.07 kips (382.86 kN) calculated at the full flexural strength.

The other method is presented by Teng et al. (2001). The Teng et al. 2001 model predicts the FRP debonding by limiting the stress in the FRP by Equation (10)

$$\sigma_{f\max} = \alpha k_b k_L \sqrt{\frac{E_f \sqrt{f_c'}}{t_f}} \text{ (MPa)} \tag{10}$$

where $\alpha = 1.1$ is found to be appropriate when determined from flexural beam tests, k_b accounts for the effect of the FRP plate width in Equation (11), k_L accounts for the effect of FRP anchorage length in Equation (12), E_f is the longitudinal modulus of FRP, t_f is the thickness of FRP, and f'_c is the concrete strength.

$$k_b = \sqrt{2 - \frac{b_f}{b} \Big/ 1 + \frac{b_f}{b}} \tag{11}$$

where b_f is the FRP plate width and b is the beam width.

$$k_L = \begin{Bmatrix} 1 & L_b \geq L_{b\max} \\ \sin\left(\pi L_b / 2L_{b\max}\right) & L_b < L_{b\max} \end{Bmatrix} \tag{12}$$

where L_b is the FRP anchorage length and L_{bmax} is the effective length in Equation (13).

$$L_{b\max} = \sqrt{\frac{E_f t_f}{\sqrt{f_c'}}} \text{ (mm)} \tag{13}$$

By determining the stress in FRP, the maximum allowable tension force in the FRP is determined by Equation (14).

$$T = \sigma_{f\max} A \tag{14}$$

The value of T computed for the rectangular beam is 28.0 kips (124.52 kN) compared to T = 44.22 kips (196.7 kN) determined by attaining full flexural capacity. The value of T computed for the T beam is 43.07 kips (191.43 kN) compared to T = 86.07 kips (382.86 kN) calculated at the full flexural strength. Complete calculations for determining the tension force in the FRP are shown in Appendix B -. If the tension force determined from the computer program is greater than the tension force calculated from the two methods, then CFRP debonding is likely. Based on the results we obtained, a premature separation of the CFRP layer is anticipated, see Table 3.5.

Analysis Results

Specimen R1

For the analysis of specimen R1, the rectangular control beam, the only program used was the flexural analysis program since the other program along with the Teng and ACI approaches are only applicable to FRP strengthened beams. Using the flexural analysis program, an ultimate moment capacity of 37.2 kip-ft is predicted. This capacity is reached by an ultimate load of 12.2 kips (54.3 kN) with a maximum deflection of 3.0 inches. The flexural analysis program also determines the cracking moment of the specimen. Cracking is expected to occur at 7.5 kip-ft which will be at a load of approximately 2.0 kips. The program predicted the specimen to fail in a mode of concrete crushing after flexural steel yielding. From the experimental results, it was noticed that the ultimate load was 12.3 kips (54.7 kN) with an ultimate deflection of 3.1 inches. The failure mode was concrete crushing as predicted. The flexural analysis program predicted the behavior of this specimen very accurately. Figure 6.1 shows the load deflection comparisons between the analysis program and the experimental results.

Figure 6.1 Comparison of Analytical and Experimental Load vs. Deflection for Specimen R1

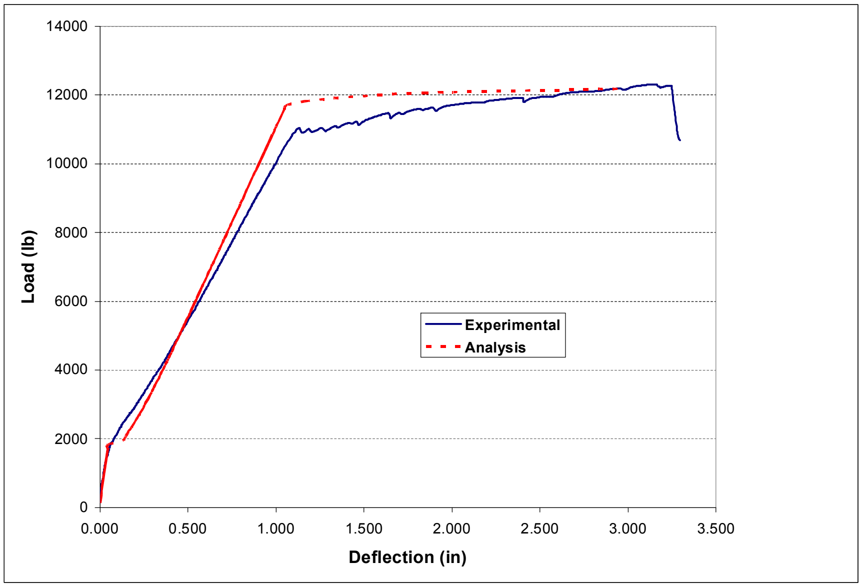

From Figure 6.1 it is observed that cracking of the experimental specimen occurred very close to the load of 2.0 kips (8.9 kN) predicted from the analysis. The steel yielding occurred at a slightly lower load than that predicted from the analysis. Figure 6.2 shows the experimental strain values for each #5 rebar used for tension. From this graph it is observed that the steel yielded at a strain of approximately 0.003 in/in.

Figure 6.2 Comparison of Analytical and Experimental Rebar Strain

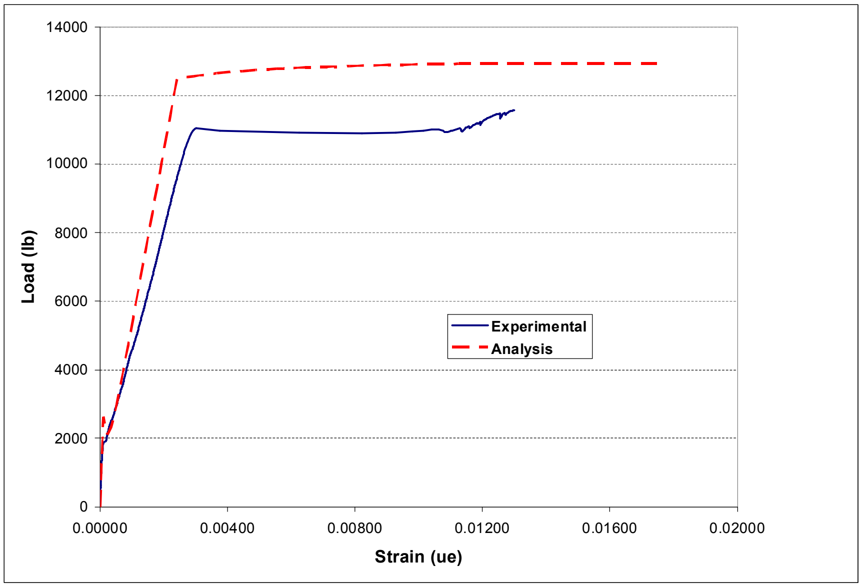

Specimen R2

For the rectangular specimen R2 with CFRP on the bottom for flexural reinforcement only, it was not possible to use the flexural analysis program to determine the premature ultimate capacity. The flexural analysis program assumes that the CFRP will remain bonded to the specimen until concrete crushing failure mode. This is not the case since the FRP is expected to debond upon exhausting the cohesion resistence of the interface. Therefore, the Teng et al. and ACI models are used to predict the load at which the FRP is expected to debond. Using the ACI model, a critical tension force in the FRP was determined to be 51.4 kips (228.6 kN). The Teng model determines the critical force in the FRP to be 28.0 kips (124.52 kN). This corresponds to a load of 20.5 kips (91.15 kN) applied to the beam. There is a lot of discrepancy between the two models. Using the shear program developed by Larson, a maximum tension force in the FRP layers is calculated to be 44.2 kips (196.7 kN) based on the ultimate flexural capacity of the beam. According to the Teng model, we should get separation to occur between the FRP and the specimen. However, the ACI model indicates that delamination will not occur. The experimental results show that the specimen reached an ultimate load of 24.6 kips (109.4 kN) when the FRP delaminated as shown in Figure 6.3. By inputting this load into the shear program a tension force in the FRP can be calculated. By doing this it is calculated that a maximum tension force of 41.6 kips (185.0 kN) was developed in the FRP. This shows that the Teng model is a very conservative approach in determining FRP delamination. We can also see that the tension force in the FRP is very close to the flexural ultimate load in the FRP at failure that was calculated to be 44.2 kips (196.6 kN). This indicates that we might not be able to get much more strength out of the FRP by using the shear wraps. Figure 6.4 shows the experimental strain values in the FRP for the specimen. This figure indicates that the strain in the FRP is slightly higher than the analytical values at the same level of load. This is attributed to the proximity of the strain gage to a flexural crack. A comparison of the strain that is experienced at the top concrete surface for the experimental and analytical results is shown in Figure 6.5. It is clear from this figure that the strains were similar. Figure 6.6 shows the strain that was experienced in the rebar for the experimental and analytical results. It is observed that the experimental strain up to the rebar yielding point is slightly higher than the predicted response. Also, the experimental response is diverted after yielding again because of the proximity to a flexural crack.

Figure 6.3 Comparison of Analytical and Experimental Load vs. Deflection for Beam R2

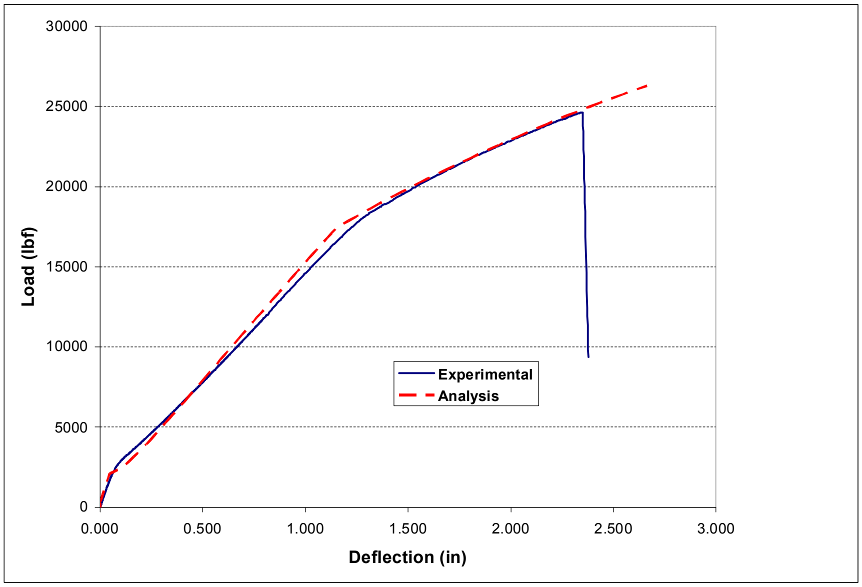

Figure 6.4 Comparison of Analytical and Experimental Strain in FRP of Beam R2

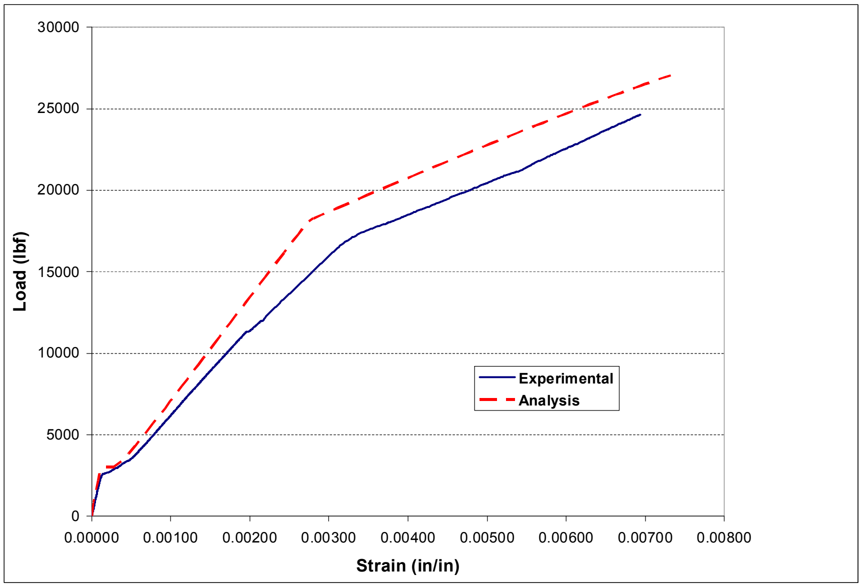

Figure 6.5 Comparison of Analytical and Experimental Load vs. Top Strain in Beam R2

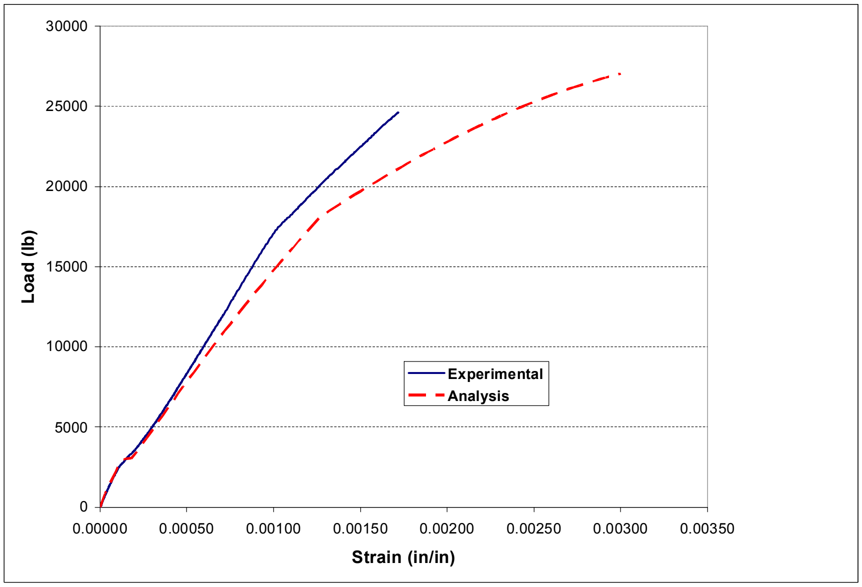

Figure 6.6 Comparison of Analytical and Experimental Strain in Rebar of Beam R2

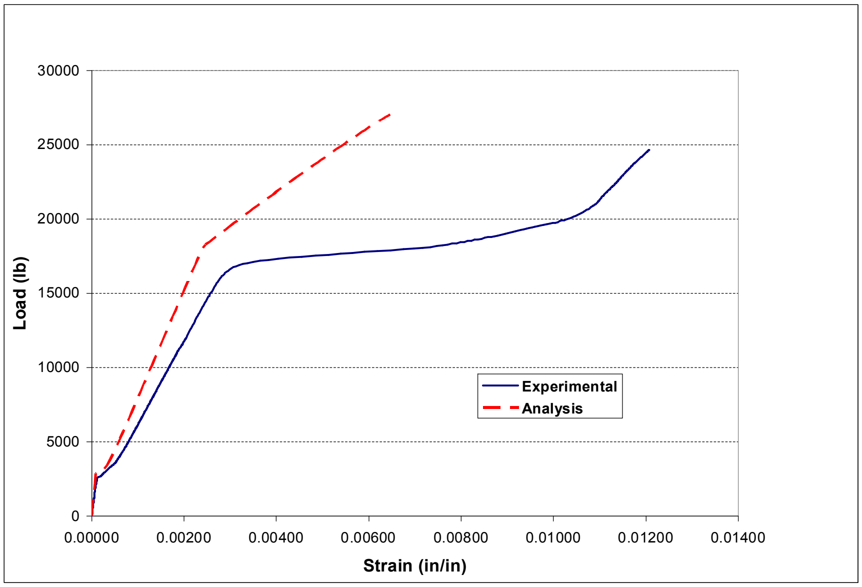

Specimen R3

The rectangular specimen R3 had both flexural and transverse FRP reinforcement applied. The same five longitudinal layers of FRP were applied as well as the U-wraps to provide anchorage reinforcement to prevent FRP separation failure mode. The amount of the U-wrap reinforcement was determined using an adapted version of the ACI 318-05 shear friction model. Detailed calculations of the transverse reinforcement by shear friction are presented in Appendix C -. The flexural analysis program was used to predict the ultimate load of the specimen. An ultimate flexural capacity of 77.7 kip-ft was predicted. This capacity was predicted to be reached by an ultimate load of 26.3 kips (117.0 kN) with a maximum deflection of 2.7 inches. Cracking is expected to occur at a moment of 7.8 kip-ft, which takes place at a load of approximately 2.1 kips (9.3 kN). The flexural analysis program predicted the specimen to fail in a mode of concrete crushing. From the experimental results, it is observed that the specimen reached concrete crushing of the top cover first then reached an ultimate load of 27.1 kips (120.5 kN) with a deflection of 2.8 inches when the FRP ruptured. The results show that cracking occurred at a load of approximately 2.4 kips. These results are very close to the behavior predicted by the analysis program. Figure 6.7 shows the comparison of the load-deflection relationship between the analysis program and the experimental results. It is evident that the rectangular specimen R3 reached the full flexural capacity by the effect of transverse reinforcement in providing resistance to separation failure by friction once cohesion is exhausted.

Figure 6.7 Comparison of Analytical and Experimental Load vs. Deflection of Beam R3

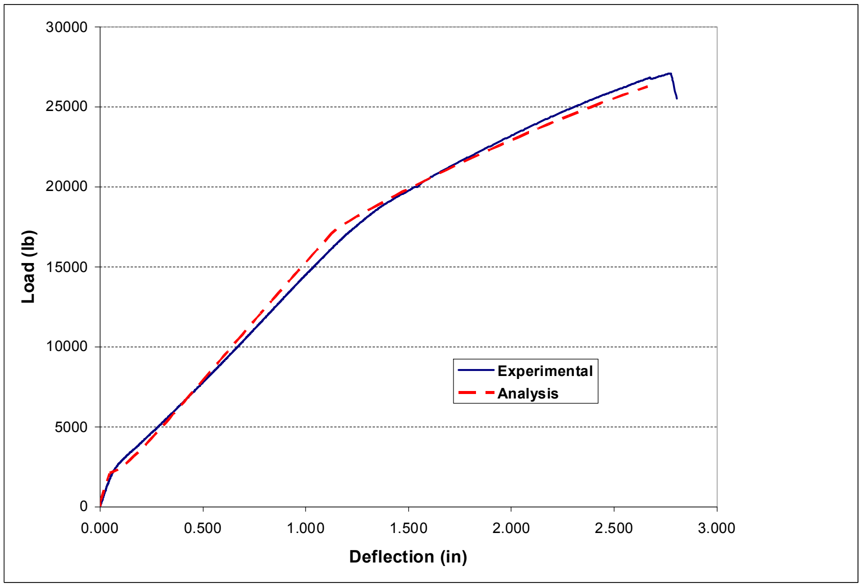

From Figure 6.7 it can be observed that cracking occurred at the same load that was predicted from the analysis program and the specimen failed very close to the analytical value. From the FRP coupon tests conducted earlier, it was observed that the specimens were reaching an average ultimate longitudinal strain of 0.0129 in/in. before rupturing. Figure 6.8 shows the experimental and analytical strain values that were experienced by the FRP layers on the R3 specimen. It is observed that the experimental strain values are higher than the analytical values at the same load level. This is attributed to the proximity of the strain gage to a flexural crack. It appears that the FRP ruptured at a strain of 0.01 in/in. indicating that the FRP ruptured prematurely. Figure 6.9 shows a comparison of the analytical and experimental strain values that were experienced at the top concrete surface at mid span. It is observed that there is an excellent agreement between the experimental and analytical results. The strain that was experienced in the rebar is also shown in Figure 6.10 for the experimental and analytical results. It is evident that the steel showed a yield plateau right at first yielding showing significantly higher strains than the predicted ones at the same load level due to slippage. Comparing the ultimate strain in flexural FRP vs. ultimate strain in steel rebar, it is evident that the latter is larger than the former. This indicates that the flexural FRP lost cohesion in between the U-wraps and slipped causing lower apparent strain.

Figure 6.8 Comparison of Analytical and Experimental Strain in FRP in Beam R3

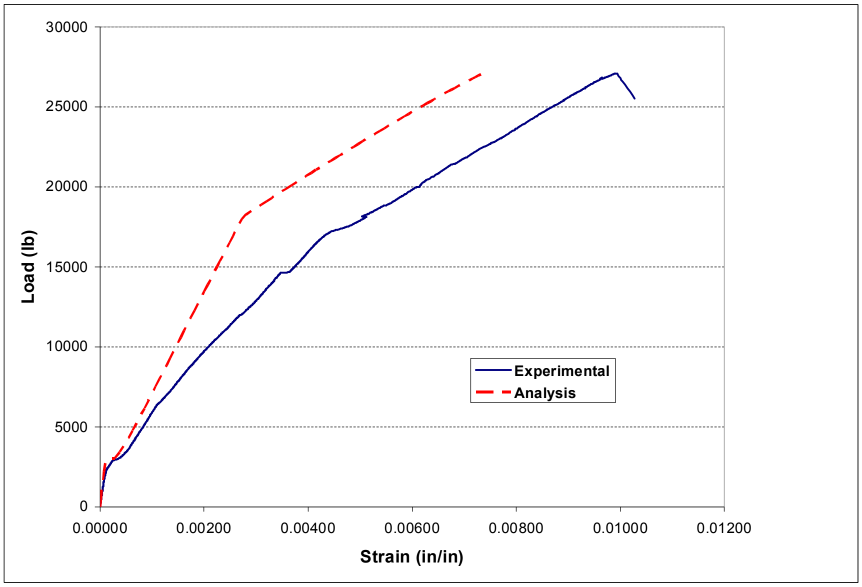

Figure 6.9 Comparison of Analytical and Experimental Strain in Top Concrete Surface at mid span of Beam R3

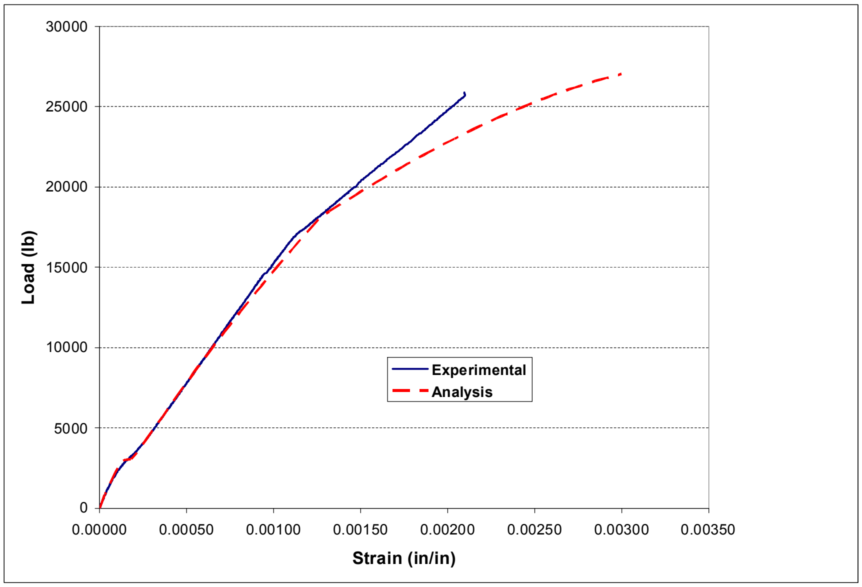

Figure 6.10 Comparison of Analytical and Experimental Rebar Strain at mid span of Beam R3

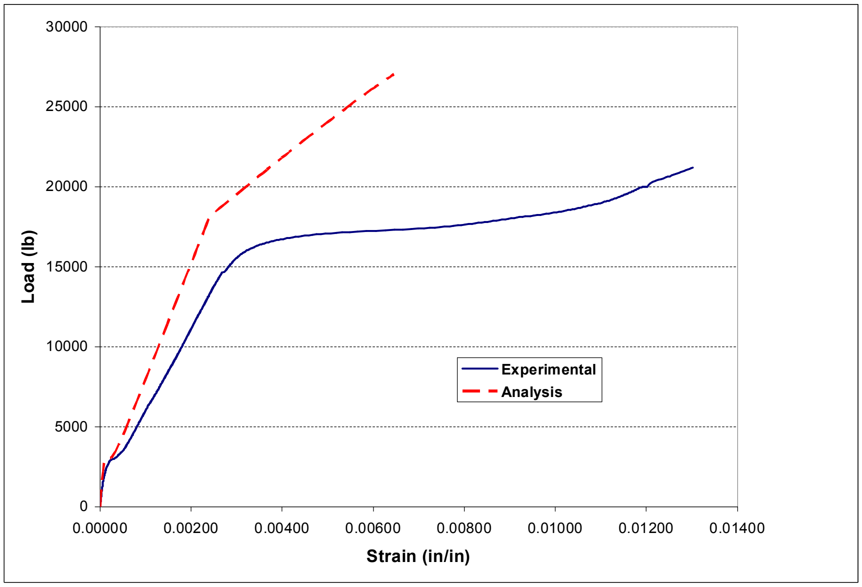

Specimen T1

The analysis of specimen T1, which is the T-shaped control beam, was performed using the flexural analysis program. From this analysis, the ultimate moment capacity of 44.1 kip-ft is predicted. This capacity is reached by an ultimate load of 15.2 kips (67.6 kN) with a maximum deflection of 9.6 inches. The flexural analysis program also determined that the cracking moment would be reached at 9.2 kip-ft or at a load of 3.2 kips (14.2 kN). The program predicted the beam to fail in a mode of flexural steel yielding followed by concrete crushing. From the experimental results, it was observed that the ultimate load was 15.9 kips (70.7 kN) with a maximum deflection of 7.0 inches. The failure mode was concrete crushing. Figure 6.11 shows the load deflection comparisons between the analysis program and the experimental results. From Figure 6.11, it appears that cracking of the experimental specimen occurred at a load of 4.5 kips (20.0 kN), slightly higher than the load of 3.2 kips (14.2 kN) predicted from the analysis. The steel yielding occurred very close to the load predicted from the analysis at around 12 kips (53.4 kN). Figure 6.12 shows the experimental versus analysis strain values for each of the two #5 rebar used as tension reinforcement. From this graph it is observed that the steel yielded at a strain of approximately 0.0024 in/in.

Figure 6.11 Comparison of Analytical and Experimental Load vs. Deflection for Specimen T1

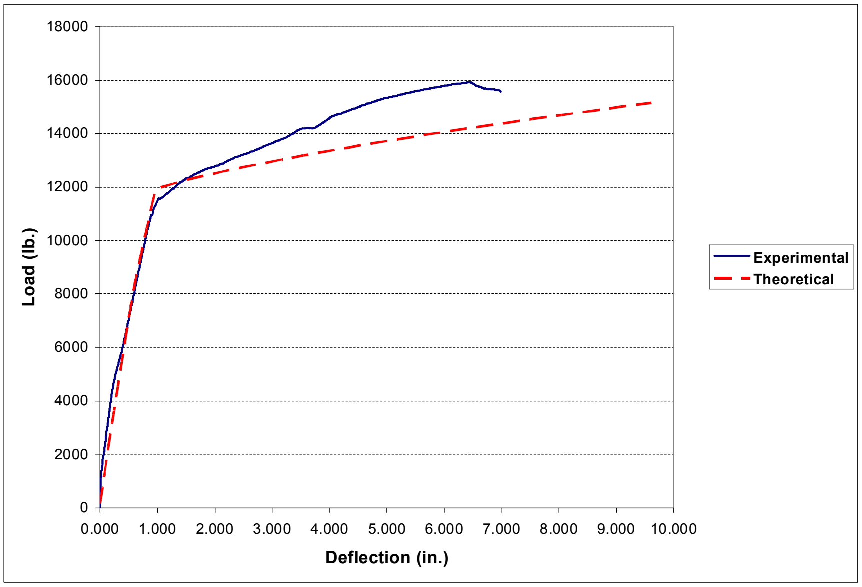

Figure 6.12 Comparison of Analytical and Experimental Rebar Strain

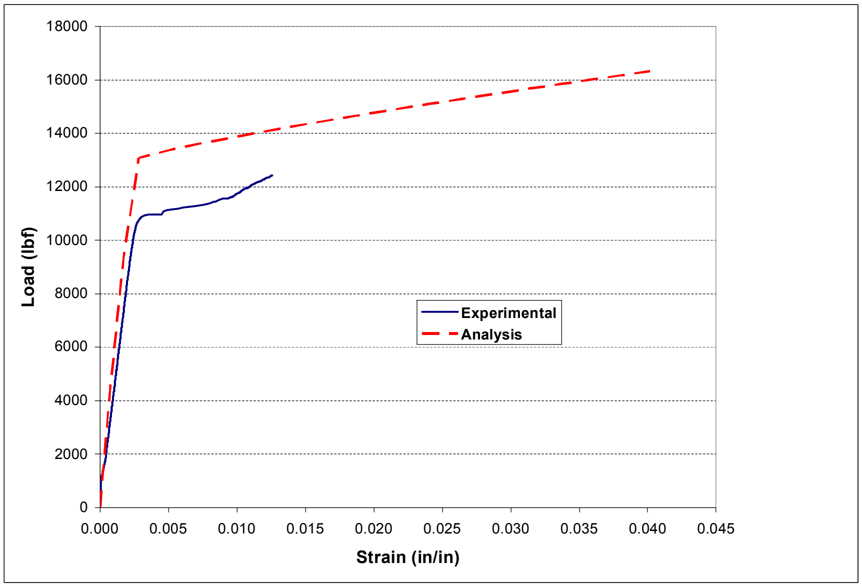

Specimen T2

For the T-beam specimen T2, strengthening with CFRP was limited to flexural reinforcement at the bottom face of the member. Similar to the analysis of specimen R2, the Teng et al. and ACI models are used to predict the load at which the FRP is expected to debond. These calculations are presented below in Equations (15) and (16) for the ACI and Teng model respectively.

$$T_{\max} = E_f \varepsilon_{fe} A \ \text{(ACI)} \tag{15}$$

$$T_{\max} = \sigma_f A \ \text{(Teng)} \tag{16}$$

Using the ACI model, a critical tension force in the FRP was determined to be 51.4 kips (228.6 kN). This corresponds to a load of 29.2 kips (129.9 kN) applied to the beam. The Teng model determines the critical force in the FRP to be 43.0 kips (191.3 kN). This corresponds to a load of 26.5 kips (117.9 kN) applied to the beam. The latter prediction is very similar to the actual experimental separation load of 25.5 kips 113.4 kN). A maximum tension force in the FRP layers is calculated to be 86.1 kips (383 kN) based on the ultimate flexural capacity of the beam. This corresponds to a load of 40.4 kips (179.6 kN) applied to the beam. According to both Teng et al. and ACI models, separation is likely to occur between the FRP and the specimen prior to ultimate flexural capacity. However, the result of the ACI 440 model was not conservative. Figure 6.13 shows the load deflection comparisons between the flexural analysis program and the experimental results. From Figure 6.13 it appears that cracking of the experimental specimen occurred at a load of 7.0 kips (31.1 kN) which is higher than the load of 3.2 kips (14.2 kN) predicted from the analysis. The experimental results show that the specimen reached an ultimate load of 25.5 kips (113.4 kN) when the FRP delaminated. By entering this load into the analysis program, a maximum tension force in the FRP was calculated to be 40.0 kips (177.9 kN). This shows that the Teng model was more accurate in predicting FRP delamination. It is also evident that the tension force in the FRP is far from that causing ultimate flexural load in the FRP that was calculated to be 38 kips (169 kN). This indicates that one should be able to gain much more strength out of the FRP system by properly anchoring the flexural FRP against premature separation. Figure 6.14 shows the experimental strain versus the analytical strain values in the FRP for the specimen. This figure indicates that the strain in the FRP is slightly higher than the analytical values at the same level of load. This is attributed to the proximity of the strain gage to a flexural crack. A comparison of the strain that is experienced at the top concrete surface for the experimental and analytical results is shown in Figure 6.15. It is clear from this figure that the strains were similar. Figure 6.16 shows the strain that was experienced in the rebar for the experimental and analytical results. It is observed that the experimental response up to the rebar yielding point is very close to the predicted response. However, the experimental response is slightly diverted after yielding again because of the proximity to a flexural crack.

Figure 6.13 Comparison of Analytical and Experimental Load vs. Deflection for Beam T2

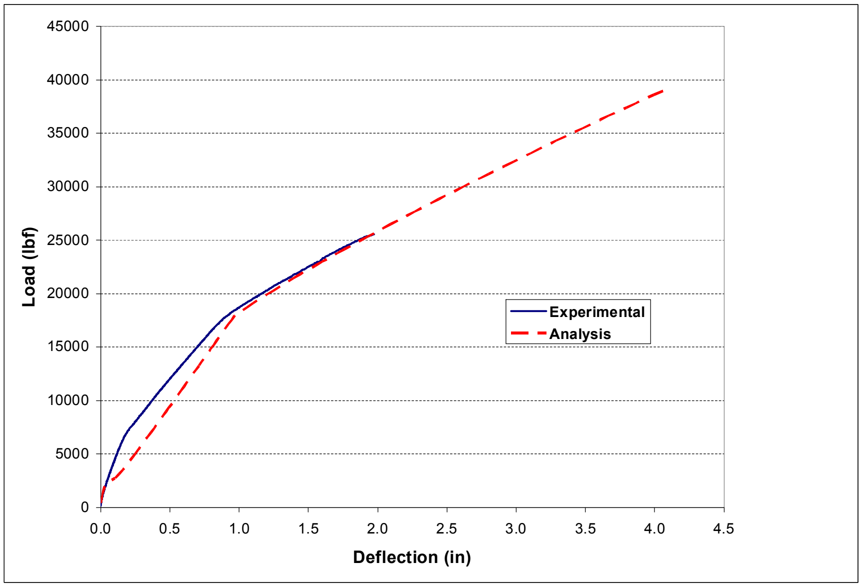

Figure 6.14 Comparison of Analytical and Experimental Strain in FRP of Beam T2

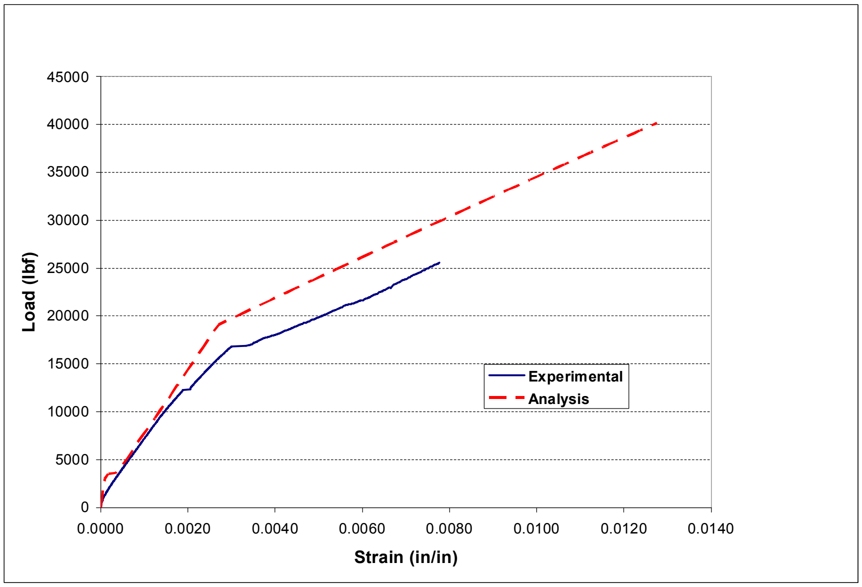

Figure 6.15 Comparison of Analytical and Experimental Load vs. Top Strain in Beam T2

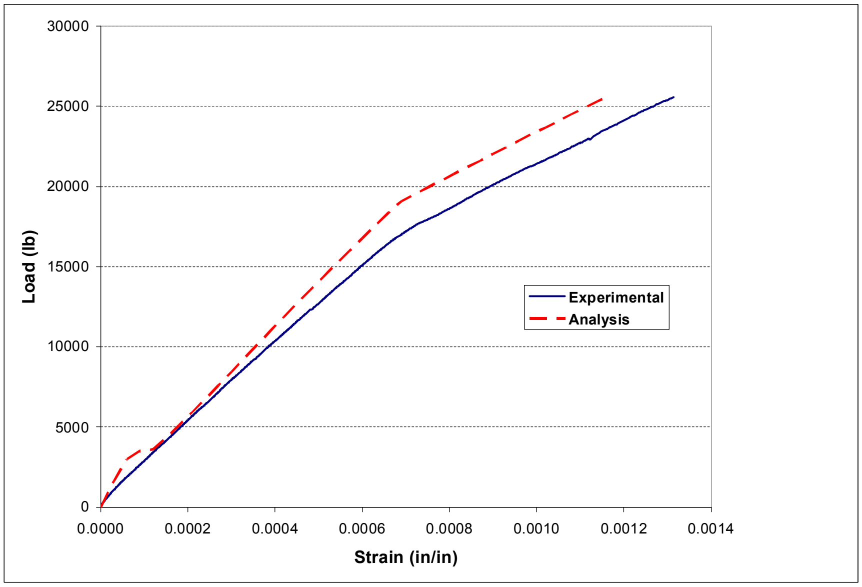

Figure 6.16 Comparison of Analytical and Experimental Strain in Rebar of Beam T2

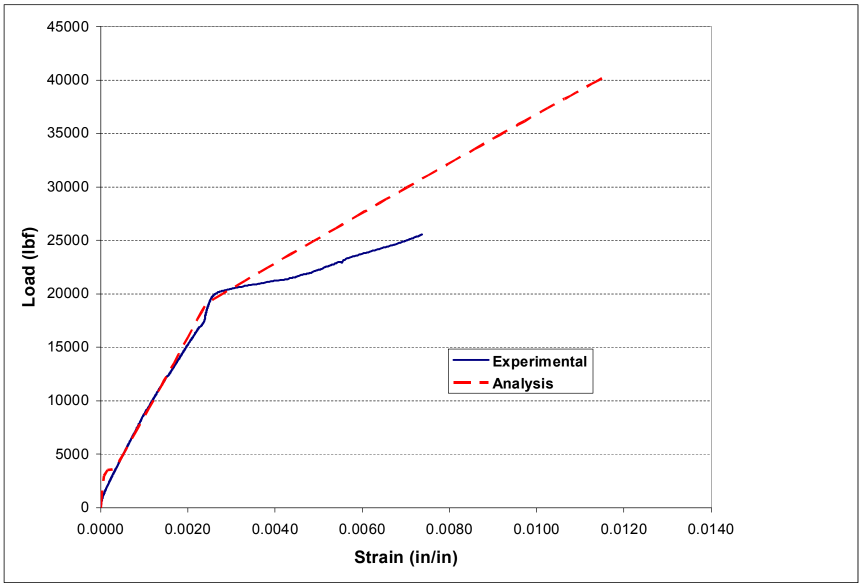

Specimen T3

The T-beam specimen T3 had a combined flexural and transverse FRP reinforcement applied. The same five longitudinal layers of FRP were applied to the bottom face of the beam as well as two layers of the U-wraps to provide anchorage reinforcement to prevent FRP separation failure mode. The amount of the U-wrap reinforcement was specified to be two layers of 5 inches width at 12 inches on center. This was determined using an adapted version of the ACI 318-05 shear friction model. Detailed calculations of the transverse reinforcement by shear friction are presented in Appendix C -. The flexural analysis program was used to predict the ultimate load of the specimen. An ultimate flexural capacity of 115.4 kip-ft was predicted. This capacity is reached at an ultimate load of 40.1 kips (178.4 kN) with a maximum deflection of 4.1 inches. Cracking was predicted to occur at a moment of 9.3 kip-ft which takes place at a load of approximately 3.2 kips (14.2 kN). The flexural analysis program predicted the specimen to fail in a mode of FRP rupture. During the experiment, the CFRP was seen to separate from the beam in between the U-wraps at a load of approximately 25 kips (111.2 kN). However, it was evident that the U-wraps held up the flexural CFRP tight in their position. From the experimental results, it is observed that the specimen reached an ultimate load of 33.5 kips (149 kN) with a deflection of 3.1 inches when the FRP ruptured at mid span. The difference between the analysis and experiment in the ultimate FRP rupture load is attributed to the fact that CFRP had no composite action in between the U-wraps causing it to reach rupture sooner. The results show that cracking occurred at a load of approximately 2.5 kips (11.1 kN). These results are very close to the behavior predicted by the analysis program. Figure 6.17 shows the comparison of the load-deflection relationship between the analysis program and the experimental results. It is observed that the T-beam specimen T3 was just short of reaching the full flexural capacity by the effect of transverse reinforcement in providing resistance to separation failure by friction once cohesion was exhausted. However, this test still provided a strength increase ratio of 2.15 over the control beam compared to 1.63 ratio achieved by Beam T2. Considering ACI 440.2R-02 case of no debonding with ($k_m = 0.9$) and an FRP reduction factor ($\psi_f = 0.85$), the predicted value of load is 33.7 kips which matches very well the experimental value of 33.5 kips (149 kN). This clearly indicates that the ACI 440.2R-02 offers an appropriate design method.

Figure 6.17 Comparison of Analytical and Experimental Load vs. Deflection of Beam T3

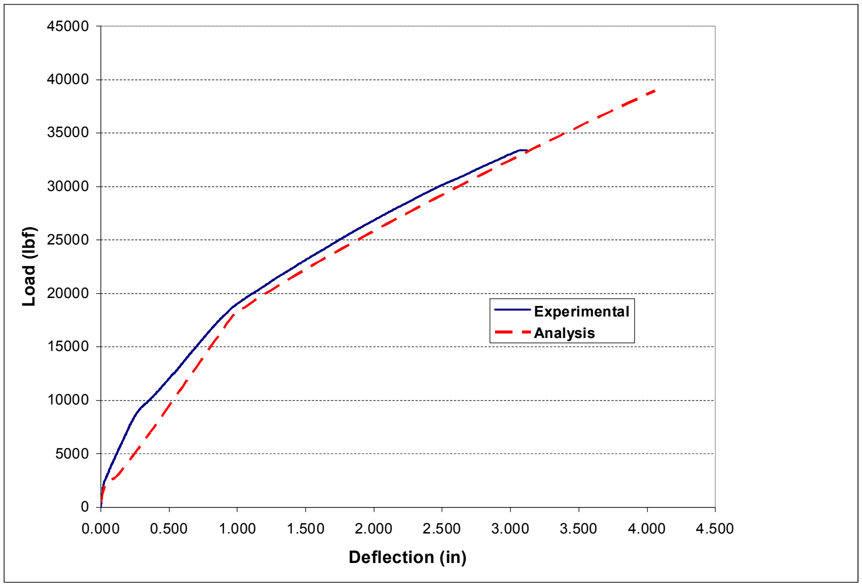

From Figure 6.17 it can be observed that cracking occurred at the same load that was predicted from the analysis program and the specimen failed very close to the analytical value. From the FRP coupon tests conducted earlier, it was observed that the specimens were reaching an average ultimate longitudinal strain of 0.0129 in/in. before rupturing. Figure 6.18 shows the experimental and analytical strain values that were experienced by the FRP layers on T3 specimen. It is observed that the experimental strain values are higher than the analytical values at the same load level. This is attributed to the proximity of the strain gage to a flexural crack. It appears that the FRP ruptured at a strain of 0.0111 in/in. which is the average of the two strain gages. This indicates that the FRP ruptured prematurely, which was the same case for the rectangular specimen. Figure 6.19 shows a comparison of the analytical and experimental strain values that were experienced at the top concrete surface at mid span. It is observed that there is an excellent agreement between the experimental and analytical results. The strain that was experienced in the rebar is also shown in Figure 6.20 for the experimental and analytical results. It is evident that the steel showed a yield plateau right at first yielding showing significantly higher strains than the predicted ones at the same load level. Comparing the ultimate strain in flexural FRP vs. ultimate strain in steel rebar, it is evident that the latter is larger than the former. This indicates that the flexural FRP lost cohesion in between the U-wraps and slipped causing lower apparent strain.

Figure 6.18 Comparison of Analytical and Experimental Strain in FRP in Beam T3

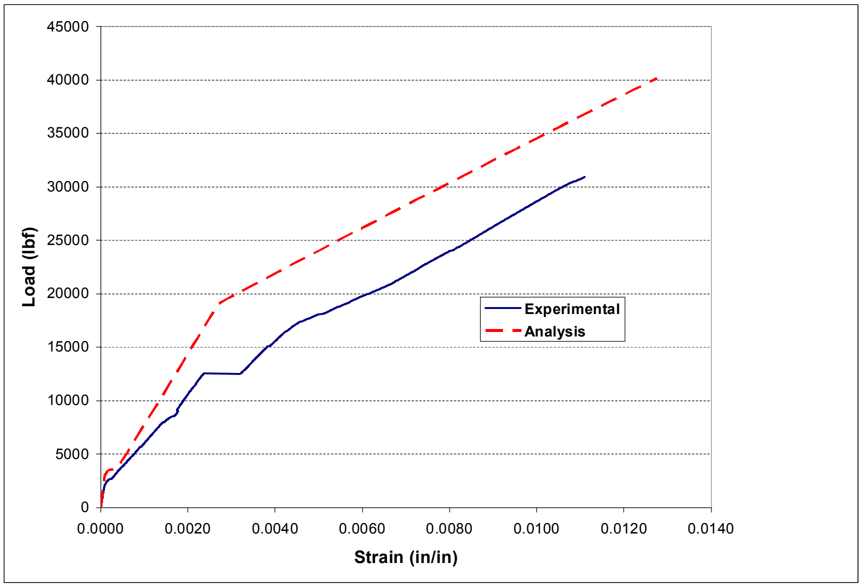

Figure 6.19 Comparison of Analytical and Experimental Strain in Top Concrete Surface at mid span of Beam T3

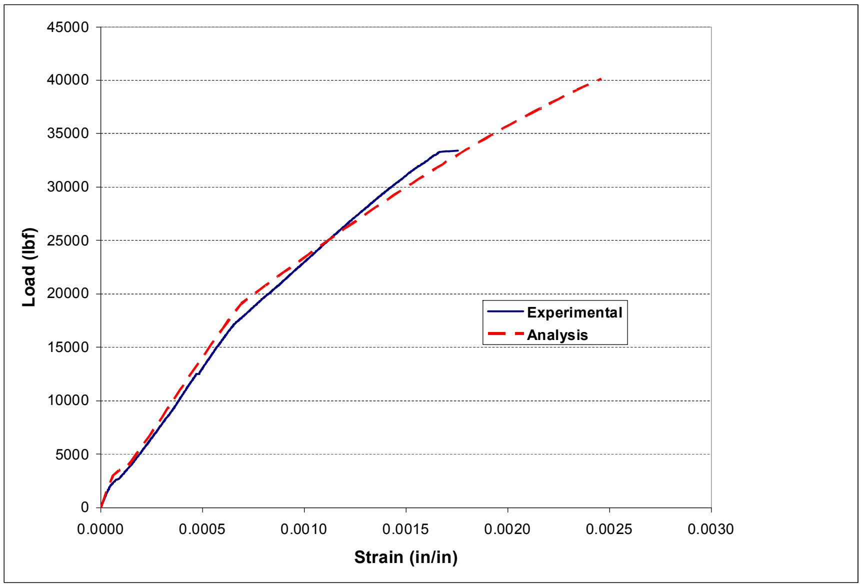

Figure 6.20 Comparison of Analytical and Experimental Rebar Strain at mid span of Beam T3

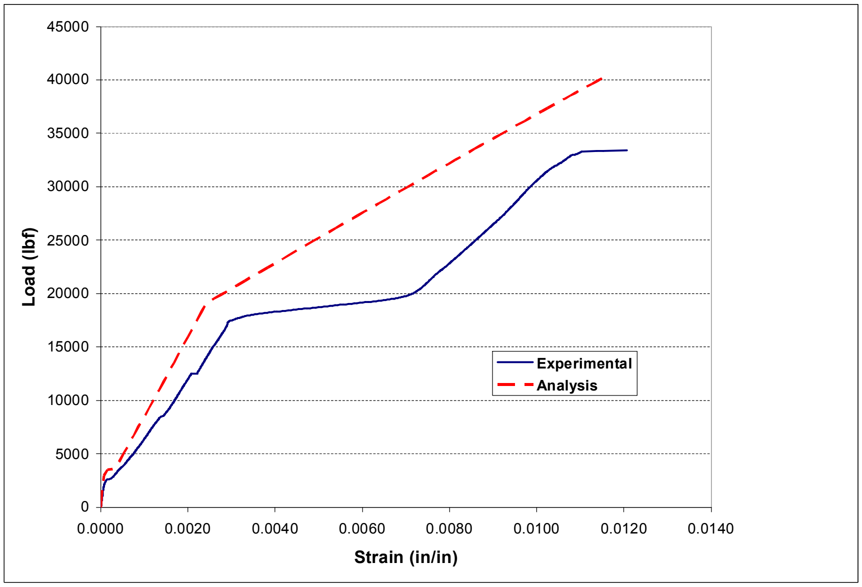

CHAPTER 7 - Conclusions and Recommendations

Throughout this research and experimental results, many conclusions were determined. The design programs were effective in designing two types of beam with two failure modes. The rectangular cross sections were designed to fail in concrete crushing, while the T-beams were designed to fail in FRP rupture. Ultimately both types of beams failed in FRP rupture but the rectangular beam failed first in concrete crushing followed by FRP rupture. A four-point bending test was conducted on each beam specimen to determine its strength as a control beam and with FRP reinforcement applied.

Using the beam analysis program the rectangular control beam was predicted to fail at a load of 12.14 kips. The experimental results indicate that the beam failed at 12.3 kips which is very close to the analytical value. For the T-beams, the analysis program predicted that the control beam would fail at a load of 12.33 kips. The experimental results indicate that the beam failed at 15.5 kips. This is quite higher than the analytical value. Another analysis was performed taking into account the effect of concrete confinement and steel post yielding stiffness. This second analysis predicted a much closer failure load of 15.33 kips.

The remaining beams were to be strengthened with CFRP reinforcement. Prior to application of the FRP, the beam surfaces had to be rotated up-side-down and cleaned by sandblasting. The application process for CFRP reinforcement is quite tedious and requires much skill and preparation. The V-Wrap 776 epoxy used for application and strengthening of FRP fabric has a very fast set time, so a very fast and effective application procedure needs to be implemented. The epoxy and FRP was effectively applied using a 3" wide roller with 1/16th inch groves. These groves remove air pockets and allow the epoxy to fully saturate the FRP fabric. When strengthening reinforced concrete beams with CFRP, the primary factor seems to be the issue of early separation failure. Teng et al. and ACI440 both provide accurate methods in determine the load at which separation is likely to occur. The Teng et al. model seemed to be conservative when predicting debonding for the rectangular beam, but it was very accurate when predicting debonding for the T-beam. For the rectangular beam with flexural FRP on the bottom only, the Teng et al. model predicted the FRP to debond at a load of 20.5 kips. The experimental results indicate that the FRP delaminated at a load of 24.6 kips. For the T-beam, the Teng et al. model predicted the FRP to delaminate at a load of 26.5 kips. The experimental results show that the FRP delaminated at a load of 25.5 kips, which is very close to the prediction by Teng et al. The ACI model on the other hand predicted that debonding would not occur for the rectangular beam, but was proved wrong as debonding occurred at a load of 24.6 kips, just short of FRP rupture. For the T-beam the ACI model predicted the FRP to debond at a load of 29.2 kips, which was slightly higher then the experimental load of 25.5 kips at which debonding occurred.

Reinforcement with flexural CFRP only seemed to provide some additional strength but failed due to separation prior to reaching full capacity. In an effort to prevent premature separation of FRP, U-wraps were designed according to the ACI 318-05 model based on shear friction. Using this model it was determined that one layer of 5.5 in. wide U-wraps were required for the rectangular beam and two layers of 5 in. wide U-wraps were required for the T-beam. The addition of CFRP U-wraps proved to be successful for both beam cross-sections. The U-wraps provided external shear reinforcement and held the flexural CFRP in place long enough to reach full capacity and fail in a mode of FRP rupture. From the experimental results, the rectangular beam failed due to FRP rupture at a load of 27.1 kips, which is very close to the predicted value of 26.28 kips determined from the analysis program. The T-beam failed in FRP rupture at a load of 33.5 kips, which was slightly lower then the predicted value of 38.7 kips from the analysis program. Infrared photography conducted on the rectangular beam verified that the U-wraps were performing as expected by indicating debonding in areas between U-wraps. By using the flexural CFRP with the U-wraps a strength increase of 220% and 216% was reached for the rectangular beam and the T-beam respectively.

This research also posed many recommendations for future work. The strengthening procedure with CFRP work well in the lab, but on-site application may be different. The lab specimens were flipped up-side-down for ease of CFRP application and safety issues. If this was applied in the field the CFRP would have to be applied while under the beam. This epoxy should still have enough adhesion to not require any type of shoring to be used. Changing environmental condition should also be researched when using CFRP reinforcing. Bridge elements are constantly going though environmental changes. Moisture and temperature changes could create drastic changes in how the CFRP behaves or how the bond is affected. Also, all laboratory experiments were conducted on specimens that were not yet cracked. The primary use of FRP in the field would be to rehabilitate bridge girders that have already been cracked. Laboratory tests could be conducted on specimens that have been cracked and then strengthened with FRP to observe if there is any difference in the behavior.

PART II: State-of-the-art Health Monitoring

CHAPTER 8 - Literature Review

The federal government currently requires that all bridges be inspected every two years for the National Bridge Inventory (NBI). The most common method of investigation is by using visual inspection. If a problem is encountered an additional investigation is usually recommended (Bernhardt 2002). A more complex method of investigation using a measurement-based evaluation process of structural conditions, maintenance and rehabilitation needs is known as structural health monitoring (Aktan, 2004). The current state of practice of structural health monitoring incorporates many sensors covering the critical nodes of the structure. All of the data from these sensors is sent through an extensive array of cables to a central data processor where the data is downloaded and managed. This process is effective and highly accurate but there are many drawbacks. Many hours are spent installing all of the sensors and running a cable from each individual sensor to the data logger. The labor involved in this extensive cabling often consumes approximately 75% of the total time involved in the test and 25% of the total cost of the test (Sridhar et al, 2005). Quite often an experienced engineer is required to be onsite to transfer the data from the acquisition unit to a computer for analysis.

One way to overcome the issues of traditional structural health monitoring (SHM) is to use remote health monitoring (RHM). RHM is a process that can be used to monitor a structure for a continuous period without having anyone onsite. The data can be monitored from an office or any remote location without having to download the data from the acquisition unit. Another advantage of RHM is the incorporation of advanced warning signals. If the sensors detect some abnormal activity in the structure, the system can be set up to send the user a warning signal or to trigger some other onsite feature such as a camera to take a picture of the cause of the unusual activity. A remote monitoring test was performed on the Star City Bridge in Morgantown, WV to demonstrate the ability of the system to transmit uninterrupted data to any place on earth (Samir et al., 2006).

The Star City Bridge is a 1004 ft long 5 lane bridge composed of a 6.5 in reinforced concrete deck supported by steel girders. The goal of the test was to identify actual stresses and locations of maximum stress that occur in the bridge elements due to natural climate and load changes, provide a continuous history of data that can be monitored at any time from any location, provide a better method of bridge management than a basic visual inspection and to be able to provide maintenance before any severe damage occurs. The structure is equipped with a variety of sensors including: embedded strain gages, embedded crack meters, displacement transducers, thermistors, external strain gages and vibrating wire strain gages all manufactured by Geokon Inc. Peizo-electric sensors were installed at the bridge entrance to provide a time history of axel loads for the weigh in motion (WIM) system. Six data loggers are used for the long-term monitoring. The data is remotely monitored from any point on earth via a telephone line by equipping the data acquisition system with a modem. All of the equipment is powered with 12V DC marine batteries that are continuously charged with solar panels (Samir et al. 2006). This experiment proved the effectiveness of a smart structure that is capable of providing real time information about its condition and load response remotely to any location in the world.

Fiber optics technology has improved drastically over the past years. Fiber optics provide a method of evaluating infrastructure in ways that have never been achievable before. The use of fiber optics has not been applied greatly to transportation infrastructure such as bridges. Fiber optics can be used to replace the conventional resistive strain gages commonly used in bridge evaluation by providing an alternative strain measuring system with light weight, small size, low transmission loss, corrosion resistance, high resolution and electromagnetic resistance. Along with these advantages, the fibers can withstand around 8000 microstrain, much higher then conventional gages (Bernhardt 2002). One of the most notable advantages of optical fibers is their ability to be embedded within a structure. They are also capable of being distorted and conformed to meet a certain geometry of the structure, which is extremely useful in detecting crack development. One of the main challenges when embedding optical fibers is protecting them against the damage that can occur when placing concrete. This raises the issue of coming up with an effective protective device that does not interfere with the sensing capability of the fiber (Ansari 2005). The sensor consists of a 3 mm diameter stainless steel rod that has a 1.5 mm deep groove cut along its length. The optical fiber rests in this groove and is sealed with epoxy to keep moisture out. The fiber is threaded through the shear keys at the ends of the rod and extended through the brass tube to protect the fiber during construction of the bridge deck.

A couple of tests have been done by researchers to determine the effectiveness of using fiber optics for bridge evaluation. The first test was conducted by the U.S. Naval Research Laboratory on a steel girder bridge on I-10 in Las Cruces, New Mexico. They developed a 64 channel fiber optic system that could be able to record traffic loading data automatically for 8 months. The system was set up to record 15 seconds of data before and after a specific traffic load was detected. Instantaneous girder deflection could be observed and individual girder deflections could be combined into a single bridge deflection model. The greatest achievement of this test was creating a remotely linked fiber optic network that could be accessed wirelessly through a modem (Bernhardt 2002).

One of the more advanced methods of state-of-the-art health monitoring is the use of wireless structural monitoring systems. Of all the state-of-the-art methods, this is the most recent and has the most room for advancements. The most obvious advantage of wireless monitoring systems is the elimination of costly and time consuming cabling to each sensor. In 1998 Straser and Kiremidjian developed the first wireless monitoring device consisting of wireless sensing units to eradicate the need of cabling. Their system was called a Wireless Modular Monitoring System (WiMMS). Wireless monitoring systems are composed of three main sub-components. These components include a multi-channel sensor interface, a computational core and the wireless communication system. The first sub-component, the sensor interface, is composed of all the different sensing devices used for the structure such as strain gages, accelerometers and displacement transducers. Most of these conventional sensors use analog outputs, so an Analog/Digital (A/D) converter is used to convert the output to a 16-bit digital signal. The next sub-component is the computational core. This is where all the data from the sensors is received and stored. Depending on the capability of the processor some small data interrogation tasks can be performed. However, this is where most of the power is consumed. Some wireless monitoring systems have a dual core design consisting of a smaller low power processor to carry out simple unit operation and data storage while a larger processor is kept turned off to conserve power unless a sophisticated engineering computation is required by the system. The final sub-component is the wireless communication system. After the data is stored and interrogated, a method needs to be proposed to transmit the data to the lab or office where is can be analyzed. Large civil engineering structures often require sensor to sensor communication in ranges up to 150 meters. To resolve this, spread-spectrum frequency hopping wireless radios are typically used which provide resistance to channel interference, multi-path reflection and path losses (Lynch et al. 2003).

Since the introduction of wireless sensing units in 1998 by Straser and Kiremidjian, Lynch et al has extended the design of these units. The primary difference in the system, developed by Lynch et al., is the incorporation of microcontrollers to perform data interrogation tasks. For the sensor interface that was used on the prototype, Lynch used an ADS7821 16-bit A/D converter from Texas Instruments which is capable of reaching sample rates of 100 kHz. Two additional sensor channels were added to acquire output from digital sensors such as accelerometers. A dual processor computational core was designed to perform demanding data interrogation tasks while still conserving power. For the basic unit operation a low power 8-bit Atmel AT90S8515 AVR microcontroller was selected because of its low cost and its design capability. For the more demanding computational tasks a powerful 32-bit Motorola MPC555 PowerPC microcontroller was selected. This powerful microcontroller is kept off during basic operations to conserve power and is only turned on by the 8-bit microcontroller when it is needed. The system provides 448 Kbytes of flash ROM and 26 Kbytes of RAM for sufficient data storage (pretty low memory, please check numbers). For the wireless communication of the system, a Proxim RangeLAN2 radio modem was chosen. The modem operates on the 2.4 GHz unregulated FCC industrial, scientific and medical band. Communication rates of 1.6 Mbps can be achieved in ranges up to 1000 feet. When the complete wireless system is fully assembled, it only takes up 15 cubic inches of volume.

The power provided for this device comes from a high density lithium battery producing 9V DC for over 15 continuous hours (Lynch, 2004).

To demonstrate the performance and feasibility of the prototype wireless sensing unit, the system was installed on a full scale civil structure. A commercial structural monitoring system was installed in parallel with the wireless system to provide a baseline to compare the system results with. For this test, the Alamosa Canyon Bridge located in Truth or Consequences, New Mexico was selected. The bridge consists of seven individual 50 ft. long spans. Each span consists of six W30x116 steel girders supporting a 7 in. concrete deck. The commercial monitoring system that was installed is the Dactron SpectraBook dynamic signal analyzer. The system consists of 8 input channels with sample rates up to 21 kHz along with a 24-bit A/D converter providing a range of 120 dB. Multiple wireless sensing unit prototypes were installed within the structure and interfaced with accelerometers. Each data acquisition system was fitted with a different type of accelerometer. For use on the cable based system the Piezotronics PCB336C accelerometer was selected. The PCB336C is capable of operating in the dynamic range of 1 to 1000 Hz with an amplitude range of ± 4 g with a sensitivity of 1 V/g. The noise level of this accelerometer is 60 μg giving a combined dynamic range of 97 dB. For use on the wireless system, the CXL01LF1 MEMS accelerometer from Crossbow Technologies was selected. The CXL01LF1 senses accelerations in the range of ± 1 g with a sensitivity of 2 V/g. The noise associated with this accelerometer is 0.5 mg producing a combined dynamic range of 67 dB.

To obtain a considerable vibration response of the bridge two different test procedures were performed. The first method of excitation was done using a modal hammer. The modal hammer is similar to a sledge hammer. The tip of the hammer is equipped with a load cell to determine the exact force that is being delivered to the bridge surface. The modal hammer is effective in producing an almost perfect impulse with a flat frequency response function. The center of the bridge deck was selected to be the impact point for the modal hammer test. The test was repeated 7 times resulting in 14 total time history recordings. The Dactron system used a sampling rate of 320 Hz to measure the response while the wireless unit measured the response at 976 Hz. At the initial peak of the frequency response, the two systems had some minor disagreement.

The Dactron system measured a peak of 0.17 g and the wireless system measured a peak of 0.13 g. After this initial peak discrepancy the two systems were in total agreement with each other. This indicates that the wireless system is reliable and accurate for obtaining time history results.

The second test method that was performed involved driving a large flatbed truck across a wood plank placed in the center of the span. The truck was driven at approximately 40 mph to produce a force greater than that of the modal hammer which will in turn produce a larger acceleration response. As with the modal hammer test, the Dactron and the wireless systems recorded the acceleration response. In this test the wireless system was configured to store the data locally and then transmit the data wirelessly after the test was complete. After the completion of the test it was concluded that both systems agreed and produced the same time histories.

A great amount of research has been done to develop a new generation of wireless sensor systems. The most recent developments are “Motes”. Motes are wireless sensor network devices that integrate sensors, processor/radio hardware and wireless networking capabilities. The most recent Mote created by Crossbow Technology Inc. is the MICA2DOT Mote which is about the size of a quarter. These motes are designed to be able to be embedded, non-obtrusive, unattended and reprogrammable.

In the present study, a different wireless system is used to generate both acceleration and strain gage records. For the strain gage sensors, a V link transceiver unit is connected to the strain gages. This unit is capable of collecting the analog data from the strain gage sensors and communicate them wirelessly to the USB base unit that receives the record and pass it to the Agile software for real time processing and plotting of the results. This system is produced by MicroStrain Inc.

Current practices of Structural Health Monitoring (SHM) can be very time consuming and labor intensive. New methods of health monitoring systems such as fiber optics and wireless sensing systems offer new approaches to the field of remote health monitoring (RHM). Fiber optics provides the primary advantage of being embedded in a structural component while being monitored from a remote location. However, fiber optics can be difficult to protect in harsh construction environments. Wireless sensing units are the most recent developments in RHM. They are extremely small in size and have been proven to produce similar results to conventional cable based systems as shown in laboratory and field tests. There is still room for further improvements in wireless sensing systems. Improved A/D converters could be developed to provide a more accurate frequency response. The limited power supply also needs to be addressed to conduct tests over longer periods of time.

CHAPTER 9 - Wireless Health Monitoring System

The final phase of the research was to explore state-of-the-art health monitoring by using a wireless data acquisition system. This research investigated only small scale lab testing. Further research will be conducted on full scale bridge girders provided that successful results are obtained from the lab specimens.

Bridge Girder Simulation

In an effort to simulate a bridge girder, a pre-stressed beam from a previous project was used. The beam has dimensions as follows: flange width of 18 inches (457.2 mm), flange height of 4 inches (101.6 mm), web width of 4 inches (101.6 mm), and a web height of 10 inches (254 mm). The beam is reinforced with 2-3/8 inch diameter prestressing strands with a jacking stress of 202 ksi (1393 MPa). The beam is 16.5 feet (5029 mm) in length. The beam cross-section is shown in Figure 9.1.

Figure 9.1 Cross-Section of Pre-Stressed Beam Used for Girder Simulation

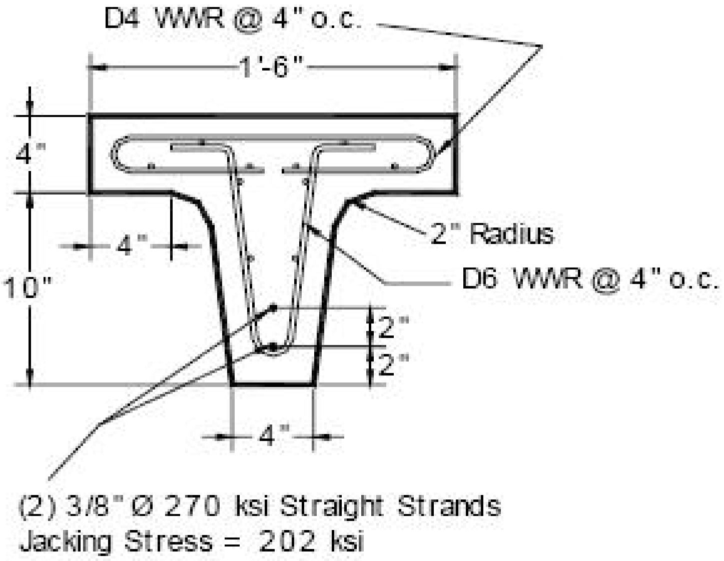

The beam is supported at the ends with a pin and roller giving a clear span of 16 feet (4877 mm). The beam is braced laterally at the supports to prevent the beam from tipping over while the load is being applied. This is strictly for safety issues since the cart carrying the load across the beam will have a high center of gravity possibly causing the beam to tip. Figure 9.2 shows the set up of the beam with lateral bracing at the end supports.

Figure 9.2 Setup of Bridge Girder Specimen

The beam was instrumented with two strain gages on the bottom of the web at mid-span. One gage was used for the conventional data acquisition system the other was used for the wireless system. The gages used have a resistance of 350 ohms and a gage length of 2 inches (50.8 mm). Two accelerometers were mounted on top of the flange at mid-span. One was the conventional accelerometer and the other was the wireless unit.

Design of Mobile Vehicle

The next step was to develop a mobile vehicle to simulate a vehicle driving across a bridge girder. A load of 2500 lbs (1134 kg) was desired for the vehicle to create substantial acceleration results so the system wasn't just picking up noise. One of the carts that is used to transport beam specimens around the lab was selected to be used as the mobile vehicle. Each of the four wheels on the cart has a capacity of 6000 lbs (2722 kg) and the wheels can be adjusted to fit any desired wheel base. The wheels also have the ability of being locked in the forward position to prevent them from pivoting while moving across the beam. The wheels were adjusted so that the distance between the wheels was 12 inches (305 mm). A wheel base any shorter than this was determined to be unsafe due to the fact that the cart could become unstable with all of the weight added to it. A wider wheel base would place the load too close to the edge of the flange of the beam possible causing it to crack. The cart has a weight of 319 lbs (145 kg). To add weight to the cart, one of the concrete blocks used for bearing support during beam tests was placed on top of the cart. This block was measured to have a weight of 1224 lbs (555 kg). Additional weight was added by using pieces of angle steel. This steel provided an additional 573 lbs (260 kg) giving a total mobile vehicle weight of 2116 lbs (960 kg). This load was determined to be sufficient enough to create substantial acceleration results.

A steel track was installed on top of the beam using 1/8 in. thick angle steel. This track prevents the cart from moving off course and possible falling off the beam. To simulate a vehicle driving over a bump on a bridge, small set screws were attached to the steel track at a distance of 4 ft, 8.5 ft and 12.5 ft. These screws created an impact and produced a larger acceleration. Figure 9.3 shows the plan view of the beam and location of the set screws.

Figure 9.3 Layout of Mobile Vehicle System with Location of Set Screws

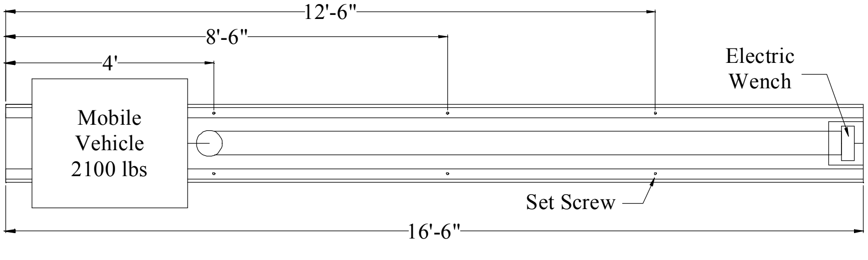

To get the mobile vehicle to move across the beam, an electric wench was mounted at the end of the beam and attached to the cart. The wench is powered by a 12 volt battery and has a capacity of 2000 lb (8896 N). To increase the capacity of the wench a pulley was attached to the cart. This doubled the capacity to 4000 lb (17.8 kN) but also reduced the speed in half. Figure 9.4 shows the beam with the electric wench attached to the cart.

Figure 9.4 Mobile Vehicle being Pulled by Wench

Data Acquisition Systems

Conventional System

To demonstrate the effectiveness of the state-of-the-art remote health monitoring system, the system was tested along side with a conventional system. Two separate conventional systems are used separately for the acceleration testing and the strain testing. For the acceleration tests, the system that is used is an accelerometer by Dataq. This accelerometer measures acceleration in only one direction. The accelerometer has a maximum frequency of 240 Hz. The accelerometer is connected to a ±10 volt power supply box. This box sends the voltage signal to a DI-194 serial port data recording module. The software used for this system is the WinDaq Waveform Browser playback and analysis software. This software allows the user to record waveforms continuously to disk and monitor the real time display of the waveforms. Figure 9.5 shows the parts of the conventional accelerometer system including the accelerometer, power supply and data recording module. For the strain experiments, the conventional system that was used was a P3500 strain indicator connected to a Keithly data acquisition system. The P3500 and the Keithly systems are shown in Figure 9.6 and Figure 9.7 respectively. The system was set up to record a strain reading once every second. The software that was used for the datalogging was developed by one of the professors in our Civil Engineering Department.

Figure 9.5 Conventional Accelerometer System

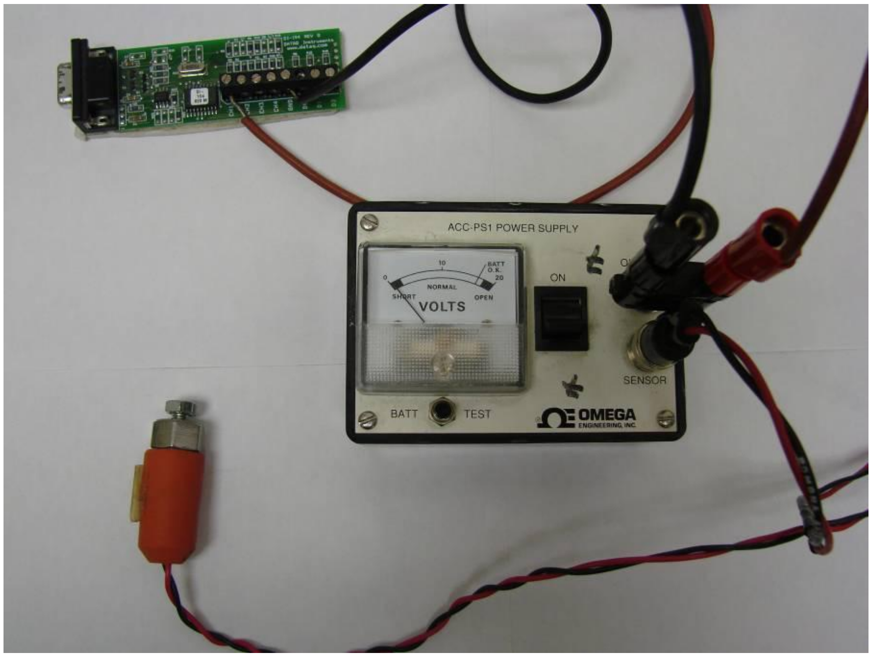

Figure 9.6 P3500 Strain Indicator

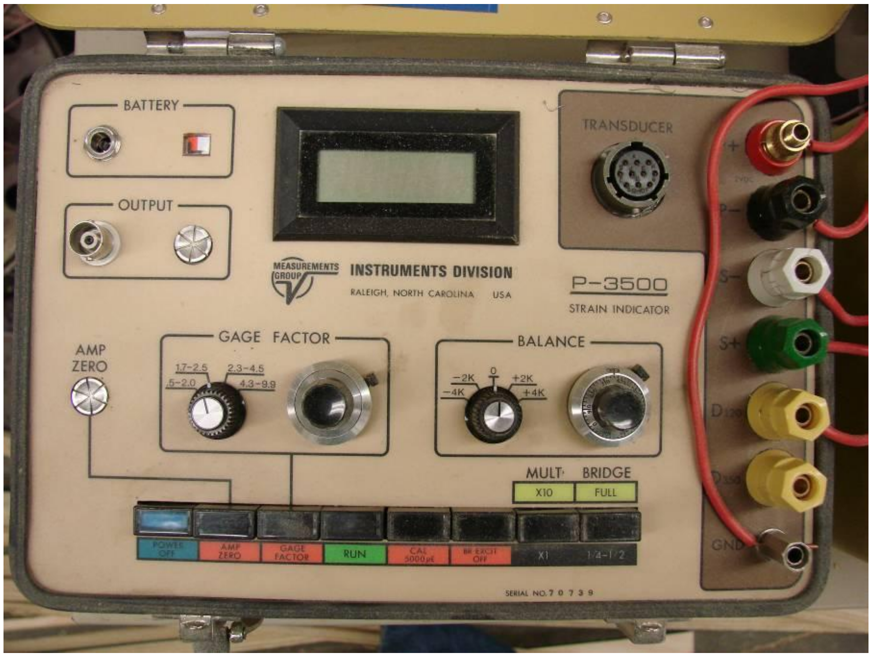

Figure 9.7 Keithly Data Acquisition System

Wireless System

Many data acquisition systems were considered for the state-of-the-art health monitoring phase. One of the wireless systems that was in consideration was developed by Crossbow Technology Inc. This system consists of tiny quarter sized wireless sensors that are programmed and controlled through a wireless network. These sensors which are referred to as motes, communicate with a base station using a radio module. This module can then be connected to an interface board which allows for communication from anywhere through the internet. The sensors can all be programmed and controlled from a remote location. A training seminar for this product was attended by Dr. Esmaeily from our research team. After learning more on how this system functions it was decided that the programming required for the software is to extreme for the purpose of this research.

The other system that was investigated is a wireless system from MicroStrain. This is the system that the research group decided to use in the research. The system is more feasible and doesn't require as much software programming. The system consists of wireless nodes that communicate with a base station. The node that is used to measure acceleration is the G-Link Wireless Accelerometer Node. This node is capable of measuring acceleration in the x, y and z axis. It can measure accelerations up to 10 G's. The node can measure acceleration in real-time streaming at a rate up to 736 Hz, and datalogging rates up to 2048 Hz. Figure 9.8 shows the G-Link node.

Figure 9.8 G-Link Wireless Accelerometer Node and Base Station

The node that is used for strain measurements is the V-Link Wireless Voltage Node. This node is capable of measuring three channels consisting of 350 ohm strain gages wired in quarter bridge configurations. This node is capable of measuring strain at a rate of up to 736 Hz in real-time streaming or datalogging at a rate of 2048 Hz. Figure 9.9 shows the V-Link node.

Figure 9.9 V-Link Wireless Voltage Node and Base Station

Results and Analysis

Strain

Several small-scale strain experiments were conducted using a 1/4 in. by 1 in. by 9.5 in. long aluminum beam. These experiments were conducted to learn the programming software. The software that is used for programming the MicroStrain nodes is called Agile Link. The software allows for streaming of real-time results and the option of data logging. The default setup of the software displays and records the data in the units of bits. The software gives the user the option of calibrating each node connected to the base station to display and record data in the appropriate units. For example, the V-Link node is equipped with a strain calibration wizard that allows for the input of the bridge configuration of the strain gage, number of gages, gage resistance, gage factor, and an onboard shunt resistance value. After calibration of the node, the results are then displayed in units of micro strain (με). Similarly the G-Link is calibrated to display and record the data in G-force units (G's).

The first feature that was tested using the MicroStrain system is its ability to effectively measure strain. All tests were performed outdoors using the pre-stressed concrete beam described earlier. For this test the set screws were removed from the steel track to create a smooth strain curve, we did not want any impact loading that would create higher strain readings. One of the strain gages at mid-span on the bottom of the web is wired into the V-Link node. The other is wired into the P3500 strain conditioner used for the conventional system. The back wheels of the mobile vehicle are placed on the beam at a distance of 4 inches from the edge of the beam. The vehicle starts at this location due to the stops that are positioned at the end of the steel rails to prevent the vehicle from accidentally rolling off the edge of the beam. The mobile vehicle is then lifted off the beam to create zero moment and zero out the strain acquisition systems. The vehicle is then placed back on the beam and rolled across the steel rails at a speed of approximately 0.21 feet per second, ft/s (0.064 m/s). The vehicle is stopped with the wheels at a distance of approximately 2 ft from the edge of the beam to prevent damaging the electric wench. After completion of the first experiment the strain was plotted against time for both systems. There appeared to be some disagreement between the two systems. Figure 9.10 shows the comparison of the results between the two systems.

Figure 9.10 Comparison of Strain Values for Test 1

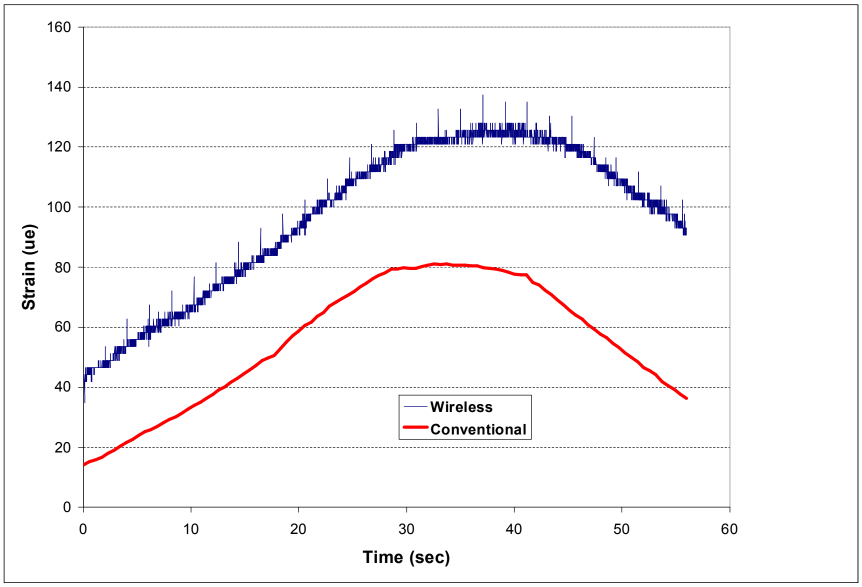

It appears that the wireless system is recording higher strains than the conventional system. The conventional system indicated a maximum strain of 81.0 με. The wireless system is indicating a maximum strain of approximately 127 με. The vehicle was reset and a second test was performed using the same procedure as the first. Following the completion of the second test the results were again plotted. The same results were observed as the first test. The wireless system recorded higher strains than the conventional system, but this time the difference in the maximum strains was higher than the first test. The conventional system shows a maximum strain of 83.0 με, where the wireless system shows a maximum strain of approximately 142 με. The conventional system seems to be consistent in the results but the wireless system does not. Figure 9.11 shows the comparison of the results from the two systems.

Figure 9.11 Comparison of Strain Values for Test 2

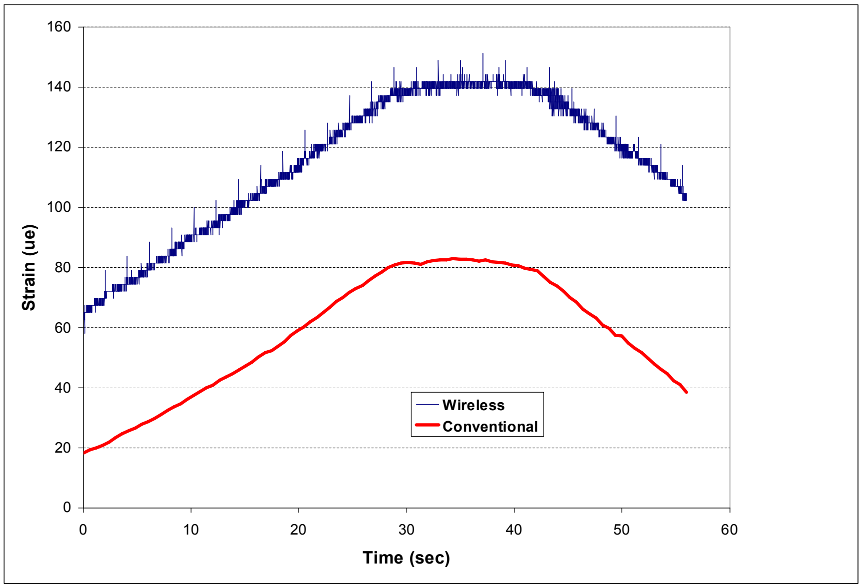

A third test was performed to determine if the same outcome would occur. After plotting the results from the third test, it was observed that the strains from the wireless system were again higher than the conventional system but seemed to be similar to the second test. The conventional system recorded a consistent maximum strain from the previous tests at 84.5 με. The wireless system recorded a strain of approximately 135 με. Figure 9.12 shows the comparison of the results from the two systems.

Figure 9.12 Comparison of Strain Values for Test 3

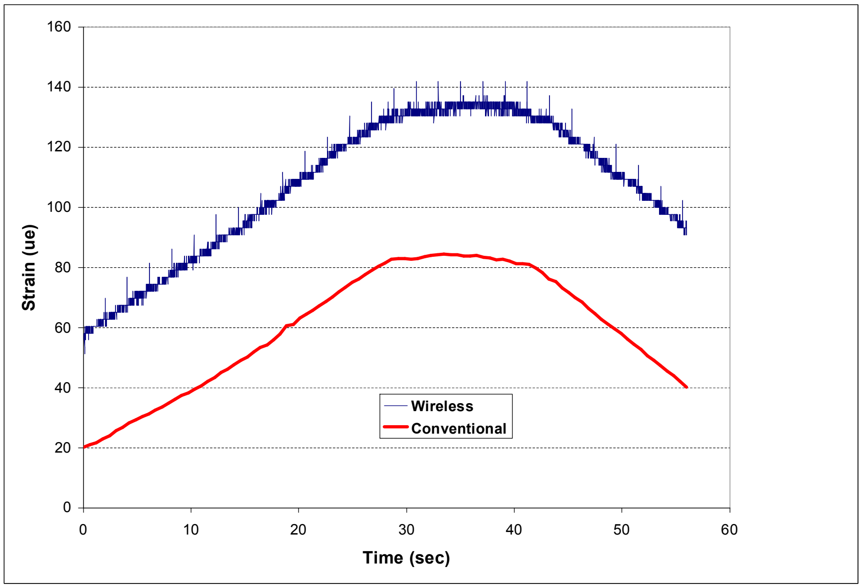

Following the days experiments, the manufacturer of the wireless system was contacted to try to determine why the results were off. After consulting with the manufacturer it was determined that the strain excitation inside the V-Link has a warm-up period where the strain will drift until the node is warmed up and the strain levels off. The internal excitation does not begin to warm up until the node is told to start acquiring data. In the previous experiments, the node was idle until the vehicle was ready to move, then the node was told to start acquiring data. Therefore, the node was warming up while the vehicle was moving. To overcome this issue, a trigger had to be created in the node.

The Agile Link software has the capability of creating triggers so when the node experienced a designated signal it will start acquiring data. This means that while the node is idle waiting for the test to begin, the internal excitation will be warming up and once the warm-up period levels off the experiment will begin. The triggers can be set to positive signal increase or a negative signal increase. The trigger was created so that the node feels when the vehicle is applied to the beam it knows that at that strain it will begin to acquire data. The triggers are based on signal units of bits, so the strain had to be converted to bits using Equation (17).

$$InputBits = \frac{(Output - Offset)}{Gain} \tag{17}$$

This bit signal was input into the trigger and the strain experiments were again conducted. Following the completion of the experiments, the strains were again plotted against time for the two systems. It is now noticed that the wireless system and the conventional system greatly agree as shown in Figure 9.13. The conventional system is showing a maximum strain at mid-span of 83.0 με. The wireless system is indicating a maximum strain at mid-span of approximately 87.8 με. This is a great relief that promising results were obtained from the MicroStrain system indicating that it can be effective in measuring strains.

Figure 9.13 Strain Comparison of Conventional and Wireless Systems

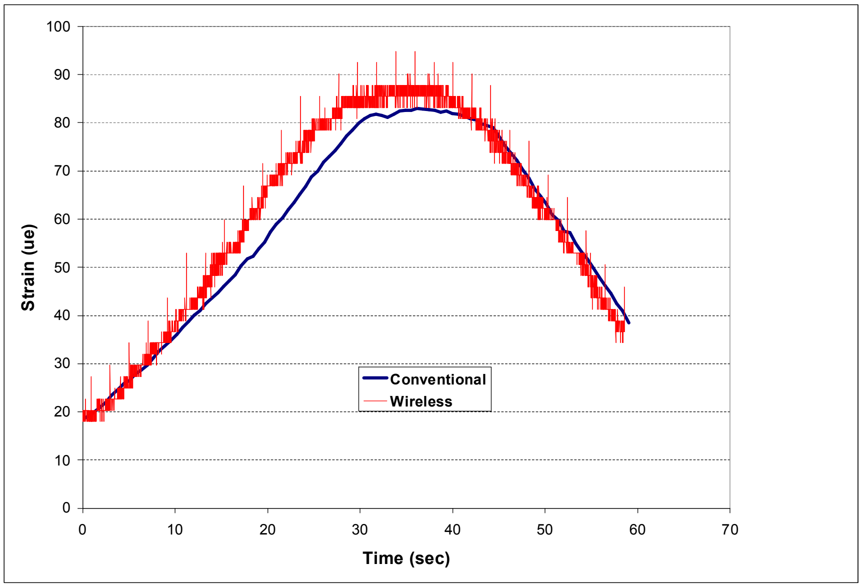

Acceleration

The next experiment that was conducted on the MicroStrain was to determine the ability of the system to effectively pick up vibration and measure acceleration. The two accelerometers were mounted side-by-side on the top of the beam flange at mid-span. For the acceleration tests the same mobile vehicle is used and is placed in the same position as it was with the strain tests. For this test the set screws were put in place on the steel track that the vehicle travels on. These set screws are to simulate a bump or imperfection that a vehicle would travel across on a bridge. The mobile vehicle was attempted to be pulled across the beam using the electric wench but when the wheel of the vehicle came in contact with the set screws the vehicle stopped to allow the wench to build up tension in the cable. This caused the vehicle to accelerate over the screws faster than the wench allowed. It also takes approximately 60 sec. for the wench to pull the vehicle across the beam. A faster speed would induce greater vibration in the beam. Therefore, it was decided that the vehicle would be pushed by hand. The maximum frequency that the G-Link can support for datalogging is 2048 Hz. The node is set up to collect 30,000 data points. At a rate of 2048 Hz, this corresponds to a time limit of 14.65 sec. Multiple trials were conducted to move the vehicle across the beam in under the time limit. After successful tests were conducted, the acceleration data was plotted. The MicroStrain system indicates a maximum acceleration of approximately ± 0.6 G's. Figure 9.14 shows the acceleration results from the MicroStrain G-Link. The spikes in the acceleration indicate where the vehicle impacted the set screws. It is observed in this figure that the acceleration is greater near the end of the beam than at mid-span. This is because the stiffness is larger at mid-span causing the amplitude to be higher.

Figure 9.14 Acceleration Results from G-Link

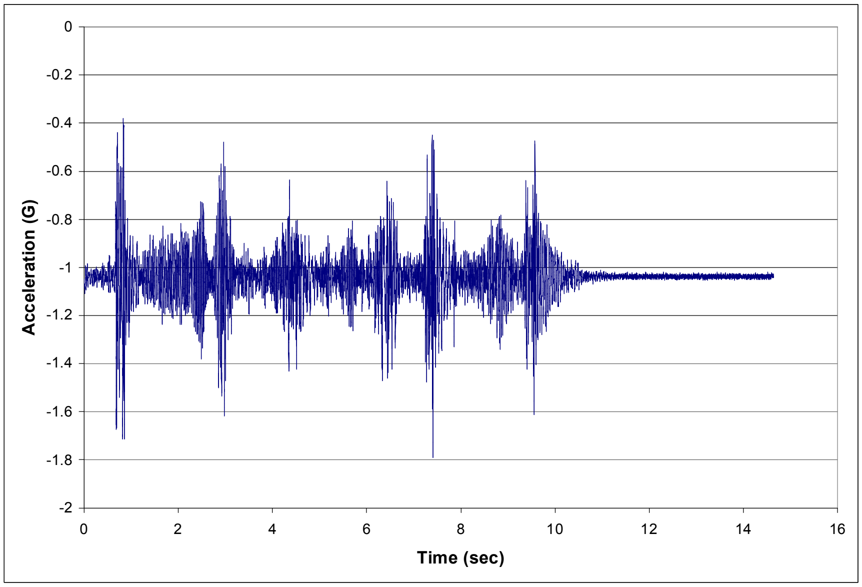

The results from the conventional system were not as conclusive. The frequency of the system is not great enough to sense the vibrations. Since the conventional system is not effective in measuring the acceleration in the beam a comparison is not made between the two systems. Instead a fast Fourier transform was performed to analyze the data. The acceleration data that is analyzed is time domain data. By performing a fast Fourier transform, the data turns into frequency domain. Figure 9.15 shows the data after being transformed. The frequencies and the magnitudes of the frequencies that were experienced by the beam are shown. The magnitude on the y-axis indicates the occurrence of each frequency. By zooming in, it can be seen that the larger magnitudes occurred between frequencies of 10 and 40 Hz. This can be seen in Figure 9.16. This data can be used for damage detection in a structure, or to determine internal changes within the structure. This aspect was beyond the scope of this research.

Figure 9.15 Frequency and Magnitude of Acceleration in Girder

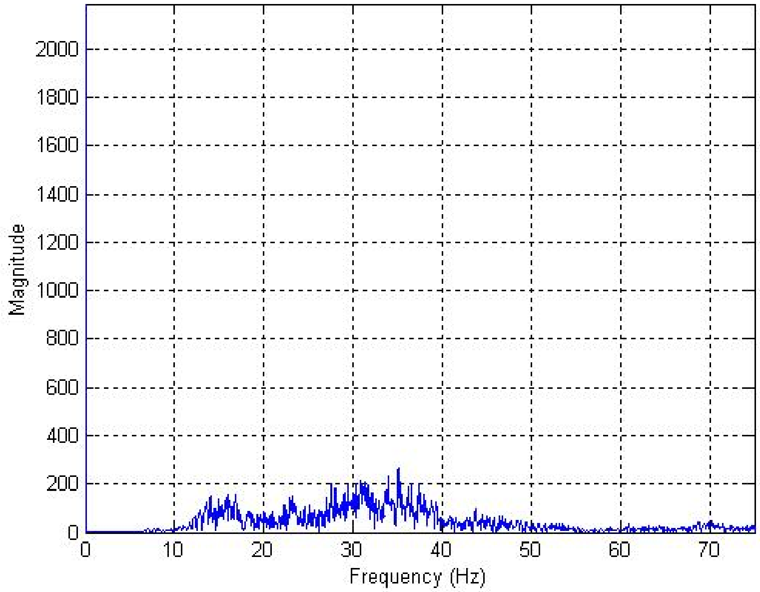

Figure 9.16 Close up of Frequencies with Higher Magnitudes

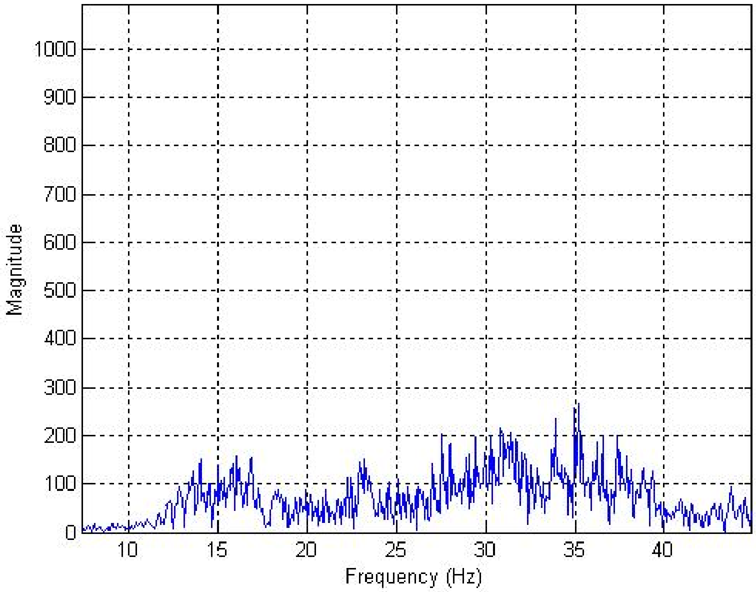

Advantages

After experimenting with the MicroStrain system, several key advantages were noticed. The system is quite simple to use. The AgileLink software that is used to program the nodes requires no knowledge of advanced programming software such as C++ or HTML. The nodes can be set up to acquire data at various sample rates. The data that is recorded is saved in a Microsoft Excel format, which is common data processing software. The system allows for streaming of multiple nodes connected to the base station at the same time. The size of the nodes is also a critical advantage. In the development of state-of-the-art health monitoring systems, small size is one of the key requirements for advancement. The nodes also have low battery consumption to allow for extended use. Rechargeable batteries are provided with the nodes. The G-Link is capable of recording acceleration in three directions which is not a common feature in current accelerometers. The V-Link connection terminals are very easy to use. They don't require any wires to be screwed to the connection terminals. It has an onboard resistor for wireless shunt calibration of strain gages, and also resistors to complete bridge configuration. The V-Link also has the capability of recording external temperatures. The customer support for the system is also very good. When the issue came up about the drift that was experienced while performing the strain experiments, the technical representative knew exactly how to correct the problem.

Disadvantages

Along with the advantages of the system, there were some disadvantages that were noticed. With both nodes, the G-Link and the V-Link, the main disadvantage was the range of use. Both nodes advertise to have the same communication range of up to 230 feet (70 meters). However, in the research this was not the case. At a distance of approximately 50 ft (15.25 m) the streaming data became very choppy. This distance also has to be clear of any obstructions. For use on bridge components this is hard to come by. Most often, instrumentation is placed on the bottom surface of bridge girders. In order to download the data from the node, the individual could not be on top of the bridge. Also, many bridge decks and girders are more than 50 ft high. This means that the individual could not stand on the ground underneath the structure and download the results. Another big disadvantage with the V-Link was the issue of the internal voltage excitation device. When obtaining experimental data it is not often desirable to wait for the system to sit idle and warm up. Especially when applied to a bridge component that is in use. The bridge would have to be closed to traffic while the instrumentation was installed and allowed to warm up. Some knowledge is also required about the behavior of the element in consideration before the data acquisition trigger can be set up. If the trigger is intended to pick up a certain events, then the strain that is to occur at that event has to be known before hand. That is often not possible for certain un-expected events. Since this MicroStrain system is quite new and has never been applied to bridge use, it is not adequate to allow the disadvantages to out weigh the advantages. I believe that these disadvantages will be taken care of with future versions of this product.

CHAPTER 10 - Conclusions and Recommendations

The mobile vehicle system that was designed was very effective. The cart along with the concrete block and the additional steel seemed to provide efficient weight to conduct the experiments. The vehicle rolled smoothly along the steel tracks with the help of the electric wench for the strain experiments. By placing small set screws along the length of the steel track, sufficient vibration was created to produce very distinguishable acceleration results.

The wireless system from Microstrain seemed to be very effective for use in state-of-the-art health monitoring. The system was very easy to program and install. The G-Link that was used to measure acceleration was capable of measuring acceleration in three directions at a very high frequency of 2048 Hz. This high frequency allowed the G-Link to capture very precise acceleration results. This frequency was much higher than the conventional system which was only capable of 240 Hz. The results from the acceleration experiment indicated that the beam was experiencing a maximum acceleration of approximately ± 0.6 G's. This maximum acceleration occurred when the mobile vehicle was near the end of the beam where the beam stiffness is larger. Since the frequency of the conventional system was so low, a comparison between the two systems could not be made. A fast Fourier transform was performed on the acceleration data to be used for damage detection which is beyond the scope of this research.

The V-Link that was used for the strain measurements was also very effective. Three strain gages are able to be wired to the V-Link for consecutive measuring. The conventional system that was used to determine the effectiveness of the V-Link was a P3500 strain indicator that was connected to a Keithly data acquisition system. When conducting the strain experiment, the two systems were not in much agreement with each other. The conventional system indicated a maximum strain of 84.5 $\mu\varepsilon$, while the wireless system was indicating a strain of 135 $\mu\varepsilon$. It was later determined that this was caused by the warm-up period associated with the internal strain excitation, which caused the strain readings to drift. This was accounted for by creating an event trigger which would allow the voltage excitation to warm up and then start acquiring data once a given event was experienced. The results after the trigger was created were in much more agreement with each other. The conventional system was indicating a maximum strain of 83 με while the V-Link was indicating a strain of 87.8 με.

This research also posed many recommendations for future work. The wireless monitoring system could be applied to a full-scale bridge out in the field. Since these wireless devices are quite new, little is known about their effectiveness outside the laboratory environment. I believe the trigger could be effective in detecting when an oversized vehicle crosses the bridge and the system could be used to alert the proper personnel. The issue with the short range could be a problem in the field since there are often many obstructions in the surrounding environment.

References And/Or Bibliography

ACI Committee 440 (2002), "Design and Construction of Externally Bonded FRP Systems for Strengthening Concrete Structures (AC I440.2R-02)." *American Concrete Institute.*

Aktan, A.E., Ciloglu, S.K., Grimmelsman, K.A. (2004). Infrastructure Health Monitoring: State-of-the-Art, Challenges and Opportunities. *2004 Conference Proceedings - Materials and Processing Technology - 60 Years of SAMPE Progress, 49,* 3234-3248.

Ansari, Farhad. (2005, June). Fiber Optic Health Monitoring of Civil Structures Using Long Gage and Acoustic Sensors. *Smart Materials and Structues, 14*(3), S1-S7.

Arduini, M.; Di Tommaso, A.; Nanni, A., "Brittle Failure in FRP Plate and Sheet Bonded Beams," *ACI Structural Journal*, Vol. 94, No. 4, 1997, pp. 363-370.

Arduini, M. and Nanni, A., "Behavior of Pre-cracked RC Beams Strengthened with Carbon CFRP Sheets." *Journal of Composites for Construction,* ASCE, Vol. 1, No. 2, 1997, pp. 63-70.

Bakis, C. E., Bank, L. C., Brown, V. L., Cosenza, E., Davalos, J. F., Lesko, J. J., Machida, A., Rizkalla, S. H. and Triantafillou, T. C. "Fiber-Reinforced Polymer Composites for Construction—State-of-the-Art Review," *Journal of Composites for Construction*, ASCE, Vol. 6, No. 2, 2002, pp. 73-87.

Bernhardt, Kristen L., Todd, Michael D. (2002). State-of-the-Art Sensing Technologies for Transportation Infrastructure Condition Assessment. *Proceedings of the International Conference on Applications of Advanced Technologies in Transportation Engineering,* pp. 457-464.

Hake, P. J. (2004). "Comparrison of compressive strengths using 4x8 vs. 6x12 cylinders for prestress concrete," MoDOT Report No. RDT 04-005, 8p.

Larson, K. H., Peterman, R. J. and Rasheed, H. A., "Strength-Fatigue Behavior of FRP Strengthened Prestressed Concrete T Beams," *Journal of Composites for Construction***,** ASCE, Vol. 9, No. 4, 2005, pp. 313-326.

Lynch, Jerome Peter., Law, Kincho H., Kiremidjian, Anne S., Carryer, Ed, et al. (2002, August). Laboratory and Field Validation of a Wireless Sensing Unit Design for Structural Monitoring. *Proceedings of the US-Korea Workshop on Smart Structural Systems,* 12p.

Lynch, Jerome P., Sundararajan, Arvind., Law, Kincho H., Kiremidjian, Anne S., Carryer, Ed., Sohn, Hoon., Farrar, Charles R. (2003). Field Validation of a Wireless Structural Monitoring System on the Alamosa Canyon Bridge. *Proceedings of the SPIE-The International Society for Optical Engineering,* 5057, 267-268.

Lynch, J.P. (2004, June). Overview of Wireless Sensors for Real-Time Health Monitoring of Civil Structures. *Proceedings of the 4th International Workshop on Structural Control and Monitoring,* 6p.

Meier, U., "Brülckensanierung mit Hochleistungs-Faserverbundwerkstoffen," *Material und Technik*, Vol. 15, 1987, pp. 125- 128.

Mosallam, Dr. Ayman., Haroun, Dr. Medhat., Feng, Dr. Maria. (2006, March). Advances in Remote Sensing and Nondestructive Evaluation of Bridges and Structures. *International Conference on Bridge Management Systems-Monitoring, Assessment and Rehabilitation.*

Quantrill, R.; Hollaway, L.; Thorne A., "Experimental and analytical investigation of FRP strengthened beam response: Part I," *Magazine of Concrete Research*, Vol. 48, No. 177, 1996, pp. 331-342.

Rahimi, H.; Hutchinson, A., "Concrete Beams Strengthened with Externally Bonded FRP Plates," *Journal of Composites for Construction*, Vol. 5, No. 1, 2001, pp. 44-56.

Ritchie, P.; Thomas, D.; Lu, L.; Connelly, G., "External Reinforcement of Concrete Beams Using Fiber Reinforced Plastics," *ACI Structural Journal*, V. 88, No. 4, 1991, pp. 490-499.

Saadatmanesh, H., and Ehsani, M. R., "RC Beams Strengthened with GFRP Plates, I: Experimental Study." *Journal of Structural Engineering, ASCE,* Vol. 117, No. 11, 1991, pp. 3417-3433.

Samir, Shoukry N., Mourad, Riad Y., Gergis, William W. (2006). Remote Health Monitoring and Modeling of Star City Bridge, WV. *Transportation Research Board 85th Annual Meeting*, pp. 1-19.

Sharif, A., Al-Sulaimani, G., Basunbul, I., Baluch, M., Ghaleb, B., “Strengthening of Initially Loaded Reinforced Concrete Beams Using FRP Plates,” ACI Structural Journal, V. 91, No. 2, 1994, pp. 160-168.

Spadea, G., Bencardino, F., Swamy, R., (). “Structural Behavior of Composite RC Beams with Externally Bonded CFRP,” *Journal of Composites for Construction*, Vol. 2, No. 3, 1998, pp. 132-137.

Sridhar, S., Ravisankar, K., Parivallal, S., Kesavan, K., Sreeshylam, P., Murthy, S.G.N. (2005, July). Remote Health Monitoring of Civil Engineering Structures-An Overview. *Proceedings of ISSS,* pp. 70-77.

Teng, J. G., Smith, S. T., Yao, J. and Chen, J. F., “Intermediate crack-induced debonding in RC beams and slabs,” *Construction and Building Materials*, Vol. 17, No. 6-7, 2003, pp. 447-462.

Appendix A - Rectangular Beam Specimen Design

Properties

Beam Geometry:

Length = 16 ft.

Clear Span = 15.5 ft

b = 6 ft

h = 12 ft

Steel Properties

E_s = 29,000 ksi

f_y = 70 ksi

d = 15.5 in

top reinforcement = 2-#3 bars

bottom reinforcement = 2-#5 bars.

#3 stirrups with 1-in cover

Concrete Properties

f'_c = 5000 psi

Flexural Design

Rectangular Beam

$$M_n = A_s f_y \left(d - \frac{a}{2} \right)$$

$$a = \frac{A_s f_y}{0.85 f'_c b}$$

$$M_n = \left(0.62in^2\right)\left(60ksi\right)\left(11in - \frac{1.46in}{2}\right) = 31.8\,k - ft$$

T-Beam

$$a = \frac{A_s f_y}{0.85 f'_c b} = \frac{\left(0.62in^2\right)\left(60ksi\right)}{0.85\left(5000psi\right)\left(16in\right)} = 0.547in \le h_f \Rightarrow \text{Design as Rectangular}$$

$$M_n = \left(0.62in^2\right)\left(60ksi\right)\left(11in - \frac{0.547in}{2}\right) = 33.3\,k - ft$$

Shear Reinforcement Design

Rectangular Beam

$$V_u = \frac{P}{2} = \frac{27.1k}{2} = 13,550\,lb$$

$$V_c = 2\sqrt{f'_c}b_w d = 2\sqrt{5000}\left(6in\right)\left(10.5in\right) = 8910\,lb$$

$$\phi V_c = 0.75V_c = 0.75(8910lb) = 6683\,lb$$

$V_u > \phi V_c \therefore shear\,reinforcement\,required$

No. 3 stirrups: $A = 0.22\,in^2$

$$V_s = \frac{V_u}{\phi} - V_c = \frac{13,550lb}{0.75} - 8910lb = 9157\,lb$$

Check $V_s \le 8\sqrt{f'_c}b_w d = 8\sqrt{5000}\left(6in\right)\left(10.5in\right) = 35,638\,lb$

$$S = \frac{A_v f_y}{50b_w} = \frac{\left(0.22\right)\left(70,000ksi\right)}{50\left(6in\right)} = 51.3\,in$$

$$4\sqrt{f'_c}b_w d = 4\sqrt{5000}\left(6in\right)\left(10.5in\right) = 17,819\,lb > V_s$$

$$\Rightarrow S_{\max} \le \frac{d}{2} \le 24in$$

$$S_{\max} = \frac{d}{2} = 5.25\,in,\ use\,S = 5\,in$$

T-Beam

$$V_u = \frac{P}{2} = \frac{33.5\,k}{2} = 16,750\,lb$$

$$V_c = 2\sqrt{f'_c}b_w d = 2\sqrt{5000}\,(6in)(10.5in) = 8910\,lb$$

$$\phi V_c = 0.75V_c = 0.75(8910lb) = 6683\,lb$$

$$V_u > \phi V_c \;\therefore\; shear\,reinforcement\,required$$

No. 3 stirrups: $A = 0.22\,in^2$

$$V_s = \frac{V_u}{\phi} - V_c = \frac{16,750lb}{0.75} - 8910lb = 13,423\,lb$$

Check $V_s \le 8\sqrt{f'_c}b_w d = 8\sqrt{5000}\,(6in)(10.5in) = 35,638\,lb$

$$S = \frac{A_v f_y}{50b_w} = \frac{(0.22)(70,000ksi)}{50(6in)} = 51.3\,in$$

$$4\sqrt{f'_c}b_w d = 4\sqrt{5000}\,(6in)(10.5in) = 17,819\,lb > V_s$$

$$\Rightarrow S_{\max} \le \frac{d}{2} \le 24in$$

$$S_{\max} = \frac{d}{2} = 5.25\,in,\; use\,S = 5\,in$$

Appendix B - Tension Force in FRP

FRP Properties

E_f = 227527 MPa

f_f = 2935 MPa

t_f = 0.1651 mm

b_f = 152.4 mm

layers = 5

Tension Force in FRP

Rectangular Beam

Method 1: ACI440.2R-02

$$A_f = t_f b_f = (0.1651mm)(5\,layers)(152.4mm) = 125.9\,mm^2$$

$$\varepsilon_{fu} = \frac{f_f}{E_f} = \frac{2935\,MPa}{227527\,MPa} = 0.0129$$

$$\kappa_m = \begin{cases} \dfrac{1}{60\varepsilon_{fu}}\left(1 - \dfrac{nE_f t_f}{360,000}\right) \le 0.90 \; for \; nE_f t_f \le 180,000 \\ \dfrac{1}{60\varepsilon_{fu}}\left(\dfrac{90,000}{nE_f t_f}\right) \le 0.90 \; for \; nE_f t_f > 180,000 \end{cases}$$

$$E_f t_f = (227527Mpa)(0.8255\,mm) = 187,937\,N/mm > 180,000$$

$$\kappa = \frac{1}{60\varepsilon_{fu}}\left(\frac{90,000}{nE_f t_f}\right) = \frac{1}{60(0.0129)}\left(\frac{90,000}{187,937}\right) = 0.6187 \le 0.90$$

$$\varepsilon_{fe} = \kappa_m \varepsilon_{fu} = 0.6187(0.0129) = 0.007981$$

$$T = E_f \varepsilon_{fe} A = (227,527)(0.007981)(125.9) = 228,600\,N = 51.4\,kips$$

Method 2: Teng et al.

$$T = A\sigma_f$$

$$A_f = t_f b_f = (0.1651mm)(5\,layers)(152.4mm) = 125.9\,mm^2$$

$$\sigma_f = \alpha k_b k_L \sqrt{\frac{E_f\sqrt{f'_c}}{t_f}}$$

$$k_b = \sqrt{\frac{2-\frac{b_f}{b}}{1+\frac{b_f}{b}}} = \sqrt{\frac{2-\frac{152.4}{152.4}}{1+\frac{152.4}{152.4}}} = 0.707$$

$$\alpha = 1.1$$

$$L_b = 1752.6\,mm$$

$$L_{b,\max} = \sqrt{\frac{E_f t_f}{\sqrt{f'_c}}} = \sqrt{\frac{(227,527)(0.826)}{\sqrt{34.47}}} = 179\,mm$$

$$L_b \geq L_{b.\max} \Rightarrow k_L = 1.0$$

$$\sigma_f = 1.1(0.707)(1.0)\sqrt{\frac{(227,527)\sqrt{34.47}}{0.826}} = 989\,MPa$$

$$T = \sigma_f A = (989\,MPa)(125.9\,mm) = 124,516\,N = 28.0\,kips$$

T-Beam

Method 1: ACI440.2R-02

$$A_f = t_f b_f = (0.1651mm)(5\,layers)(152.4mm) = 125.9\,mm^2$$

$$\varepsilon_{fu} = \frac{f_f}{E_f} = \frac{2935\,MPa}{227527\,MPa} = 0.0129$$

$$\kappa_m = \begin{cases} \frac{1}{60\varepsilon_{fu}}\left(1-\frac{nE_f t_f}{360,000}\right) \leq 0.90 \; for\; nE_f t_f \leq 180,000 \\ \frac{1}{60\varepsilon_{fu}}\left(\frac{90,000}{nE_f t_f}\right) \leq 0.90 \; for\; nE_f t_f > 180,000 \end{cases}$$

$$E_f t_f = (227527Mpa)(0.8255\,mm) = 187,937\,N/mm > 180,000$$

$$\kappa = \frac{1}{60\varepsilon_{fu}}\left(\frac{90,000}{nE_f t_f}\right) = \frac{1}{60\left(0.0129\right)}\left(\frac{90,000}{187,937}\right) = 0.6187 \le 0.90$$

$$\varepsilon_{fe} = \kappa_m \varepsilon_{fu} = 0.6187\left(0.0129\right) = 0.007981$$

$$T = E_f \varepsilon_{fe} A = \left(227,527\right)\left(0.007981\right)\left(125.9\right) = 228,600\,N = 51.4\,kips$$

Method 2: Teng et al.

$$T = A\sigma_f$$

$$A_f = t_f b_f = \left(0.1651mm\right)\left(5\,layers\right)\left(152.4mm\right) = 125.9\,mm^2$$

$$\sigma_f = \alpha k_b k_L \sqrt{\frac{E_f\sqrt{f'_c}}{t_f}}$$

$$k_b = \sqrt{\frac{2-\frac{b_f}{b}}{1+\frac{b_f}{b}}} = \sqrt{\frac{2-\frac{152.4}{406.4}}{1+\frac{152.4}{406.4}}} = 1.087$$

$$\alpha = 1.1$$

$$L_b = 1752.6\,mm$$

$$L_{b,\max} = \sqrt{\frac{E_f t_f}{\sqrt{f'_c}}} = \sqrt{\frac{\left(227,527\right)\left(0.826\right)}{\sqrt{34.47}}} = 179\,mm$$

$$L_b \ge L_{b.\max} \Rightarrow k_L = 1.0$$

$$\sigma_f = 1.1\left(1.087\right)\left(1.0\right)\sqrt{\frac{\left(227,527\right)\sqrt{34.47}}{0.826}} = 1521\,MPa$$

$$T = \sigma_f A = \left(1521\,MPa\right)\left(125.9\,mm\right) = 191,441\,N = 43.0\,kips$$

Appendix C - Design of FRP U-Wraps

Rectangular Beam

$$T = E_f A_f \varepsilon_{fu} = T_{\max} = 196,697\,N = 44.22\,k$$

$$V_{hu} = \frac{T_{\max}}{L_a} = \frac{44.22\,k}{5.5\,ft} = 8.04\,k/ft$$

$$T_{sf} = \frac{V_{hu}}{\mu} = \frac{8.04}{1.4} = 5.74\,k/ft$$

$$T_{sf} = \theta A_{vf} f_{fe}$$

$$f_{fe} = 100\,ksi$$

$$A_{vf} = \frac{T_{sf}}{\theta f_{fe}} = \frac{5.74}{0.85(100)} = 0.0675\,in^2/ft$$

Using a 12 in. spacing,

$$w_f = \frac{A_{vf}}{2nt_f} = \frac{0.0675(1\,ft)}{2(1)(0.0065)} = 5.2\,in$$

Use 5.5 in. stirrups @ 12 in. o.c.

T-Beam

$$T = E_f A_f \varepsilon_{fu} = T_{\max} = 382,858\,N = 86.07\,k$$

$$V_{hu} = \frac{T_{\max}}{L_a} = \frac{86.07\,k}{5.5\,ft} = 15.42\,k/ft$$

$$T_{sf} = \frac{V_{hu}}{\mu} = \frac{15.42}{1.4} = 11.02\,k/ft$$

$$T_{sf} = \theta A_{vf} f_{fe}$$

$$f_{fe} = 100\,ksi$$

$$A_{vf} = \frac{T_{sf}}{\theta f_{fe}} = \frac{11.02}{0.85(100)} = 0.1296\,in^2/ft$$

Using a 12 in. spacing,

$$w_f = \frac{A_{vf}}{2nt_f} = \frac{0.1296\left(1ft\right)}{2\left(1\right)\left(0.0065\right)} = 9.77\,in$$

Using 2 layers,

$$w_f = \frac{A_{vf}}{2nt_f} = \frac{0.1296\left(1ft\right)}{2\left(2\right)\left(0.0065\right)} = 4.98\,in$$

Use 5 in. stirrups @ 12 in. o.c.